Nevada Department of Transportation
Research Report No. 023-20-803
Repair and Testing of Out-of-Plane Seismic Response of Pocket Connections
January 2022

Disclaimer

TECHNICAL REPORT DOCUMENTATION PAGE

1. Report No. 023-20-803	2. Government Accession No.	3. Recipient's Catalog No.
4. Title and Subtitle Repair and Testing of Out-of-Plane Seismic Response of Pocket Connection		5. Report Date January 2020
		6. Performing Organization Code
7. Author(s) Allan J. Romero, Mohamed A. Moustafa, M. Saiid Saiidi, Hamed Ebrahimian		8. Performing Organization Report No.
9. Performing Organization Name and Address University of Nevada, Reno 1664 N. Virginia St. MS 0258 Reno, NV 89557		10. Work Unit No.
		11. Contract or Grant No. 023-20-803
12. Sponsoring Agency Name and Address Nevada Department of Transportation 1263 South Stewart Street Carson City, NV 89712		13. Type of Report and Period Covered Final Report March 2020 to January 2022
		14. Sponsoring Agency Code
15. Supplementary Notes n/a		

16. Abstract

Accelerated bridge construction (ABC) has been utilized in precast bridge structures because of its advantage to expedite on-site construction. In ABC, one of the main concerns is the joint connection as it needs to be well designed to maintain structural integrity. Several studies were able to demonstrate the effectiveness of ABC pocket connections for partial and fully precast columns. The pocket connections are designed to have the cap beam longitudinal reinforcements bundled outside the joint allowing the placement of the column uninhibited. On the contrary, this has been an issue for cast-in-place (CIP) construction where congestion of the reinforcements in the joint regions is typical. A recent study at the University of Nevada, Reno (UNR) was conducted by utilizing ABC pocket connection in CIP bridges. The specimen was tested at UNR Earthquake Engineering Laboratory on a shake table in an upside-down configuration using an increasing scaled ground motion. The specimen performed well under out-of-plane ground motion excitations and the ductility of the column was confirmed through typical plastic hinge behavior. In this study, the main objective is to further use the specimen from the recent UNR test to repair the damaged column and to test the repaired specimen using the same loading protocol as the original model.

The objective was achieved by developing a repair method using flush cutting and coring of the damaged column. A new column was constructed using the exact reinforcements as the original model. However, the column was cast monolithically in the pocket joint as opposed to the original model where the column reinforcement sat in two different concrete casts with a cold joint at the column-cap beam interface. The repaired column was subjected to the same loading protocol as the original model using the scaled 1994 Northridge earthquake ground motion recorded at the Sylmar Converter Station. The repaired specimen performed well as the plastic hinge zone developed in the column outside the joint, close to the interface of the cap beam, as desired and required by design. The results were compared to the original specimen and the maximum drift ratio for 20% through 450% of the earthquake motion was relatively equal. However, for 550% and 650% of the earthquake motions, the drift ratio in the repaired specimen was significantly larger compared to the original specimen. The high drift ratios were attributed to the slippage of the column in the joint and were validated by an increase in the ratios between the rotations of the original and repaired column recorded at the base. The cap beam remained essentially elastic, i.e. capacity-protected as required, throughout the test which is similar to the performance of the original model. Lastly, recommendations for the repair of CIP cap beam-column emulating ABC pocket connection are provided with special attention to roughen the pocket joint connection to develop a sufficient bond between the two members.

17. Key Words Accelerated Bridge Construction (ABC); cast-in-place (CIP) construction; repair; shake table testing	18. Distribution Statement No restrictions. This document is available through the: National Technical Information Services Springfield, VA 22161

19. Security Classif (of this report) Unclassified	20. Security Classif (of this page) Unclassified	21. No. of Pages 126	22. Price n/a

Form DOT F 1700.7 (8-72) Reproduction of completed page authorized NDOT Rev 04/2022

University of Nevada, Reno

Repair and Shake Table Testing of Out-of-Plane Seismic Response of Simplified Cast-in-Place Joints using ABC Pocket Connection

Allan Joseph Romero

Dr. Mohamed A. Moustafa

Dr. M. Saiid Saiidi

Dr. Hamed Ebrahimian

January 2022

ABSTRACT

Accelerated bridge construction (ABC) has been utilized in precast bridge structures because of its advantage to expedite on-site construction. In ABC, one of the main concerns is the joint connection as it needs to be well designed to maintain structural integrity. Several studies were able to demonstrate the effectiveness of ABC pocket connections for partial and fully precast columns. The pocket connections are designed to have the cap beam longitudinal reinforcements bundled outside the joint allowing the placement of the column uninhibited. On the contrary, this has been an issue for cast-in-place (CIP) construction where congestion of the reinforcements in the joint regions is typical. A recent study at the University of Nevada, Reno (UNR) was conducted by utilizing ABC pocket connection in CIP bridges. The specimen was tested at UNR Earthquake Engineering Laboratory on a shake table in an upside-down configuration using an increasing scaled ground motion. The specimen performed well under out-of-plane ground motion excitations and the ductility of the column was confirmed through typical plastic hinge behavior. In this study, the main objective is to further use the specimen from the recent UNR test to repair the damaged column and to test the repaired specimen using the same loading protocol as the original model.

The objective was achieved by developing a repair method using flush cutting and coring of the damaged column. A new column was constructed using the exact reinforcements as the original model. However, the column was cast monolithically in the pocket joint as opposed to the original model where the column reinforcement sat in two different concrete casts with a cold joint at the column-cap beam interface. The repaired column was subjected to the same loading protocol as the original model using the scaled 1994 Northridge earthquake ground motion recorded at the Sylmar Converter Station. The repaired specimen performed well as the plastic hinge zone developed in the column outside the joint, close to the interface of the cap beam, as desired and required by design. The results were compared to the original specimen and the maximum drift ratio for 20% through 450% of the earthquake motion was relatively equal. However, for 550% and 650% of the earthquake motions, the drift ratio in the repaired specimen was significantly larger compared to the original specimen. The high drift ratios were attributed to the slippage of the column in the joint and were validated by an increase in the ratios between the rotations of the original and repaired column recorded at the base. The cap beam remained essentially elastic, i.e. capacity-protected as required, throughout the test which is similar to the performance of the original model. Lastly, recommendations for the repair of CIP cap beam-column emulating ABC pocket connection are provided with special attention to roughen the pocket joint connection to develop a sufficient bond between the two members.

ACKNOWLEDGMENTS

This study was funded by the Nevada Department of Transportation through an agreement no. # P023-20-803. The research team would like to thank the Earthquake Engineering Laboratory staff members Dr. Patrick Laplace, Mr. Chad Lyttle, and Mr. Todd Lyttle. The help provided by the undergraduate student researcher, Mr. Edwin Casildo Rios, is acknowledged. We also thank Mr. Masood Vahedi and Mr. Jose Heredia for helping with the instrumentation as well as Ms. Milana Cimesa, Mr. Ronaldo Grijalva, and Mr. Pawan Acharya for helping at various stages of the preparation of the test specimen and shake table test setup.

TABLE OF CONTENTS

LIST OF TABLES

LIST OF FIGURES

CHAPTER 1. INTRODUCTION

1.1. Background

Accelerated Bridge Construction (ABC) has been gaining attention in bridge design and construction with the intention to reduce the amount of time and resources for on-site construction. Compared to conventional cast-in-place (CIP) construction, the ABC method provides a more efficient way of bridge construction by utilizing precast members which minimize or eliminate the on-site construction process such as formwork, shoring, casting, and curing of the concrete. Removing these traditional processes speeds up the construction and avoids prolong disturbance in public roads. In ABC construction, a significant concern is the behavior of joints especially when bridge structures are located in areas of high seismicity with large and frequent earthquakes. Tazarv and Saiidi [1] conducted a test that utilizes ABC pocket connections in precast bent caps. The study demonstrated the seismic validity of using ABC pocket connection in joint connections, which is advantageous in significantly reducing on-site construction work. Other studies from Mohebbi et al. [2] and Mehrsoroush et al. [3] also confirmed the effectiveness and validity of the application of ABC pocket connections in reducing construction time.

Contrary to ABC pocket connections, conventional CIP concrete bridge structures are more difficult to construct because of having to thread the cap beam longitudinal reinforcements into the column reinforcement. Moreover, additional reinforcement is needed to avoid failure in the joint caused by principal stresses. This can lead to congestion in the joint area making concrete placement difficult and the construction time-consuming. Inspired by the concept of ABC pocket connection, Schwartz et al. [4] examined the applicability of ABC pocket connection details for CIP cap beam-column connection. The study showed the effectiveness and acceptable seismic behavior of the CIP pocket connections mimicking ABC joints as evident from the observed essentially elastic behavior of the cap beam and the development of the plastic hinge fully in the column close to the beam-column interface as desired and required by design.

1.2. Literature Review

A literature review from recent studies was conducted to provide an overview of previous work that determined the effectiveness of pocket connections in seismic bridge joint connections. ABC pocket connections were utilized in such a way that connections between reinforced columns and adjacent members like cap beams can be simplified. Pocket connections can perform as pin or moment connections and can be utilized with partially-cast columns, columns made of fiber-reinforced polymer composite tube materials, or full precast columns. Several studies about pocket connections had demonstrated the desired ductile behavior in the column and showed that damage in the joint and the surrounding members can be minimal.

Matsumoto et al. [5] and Mehraein and Saiidi [6] investigated the use of partially-cast columns in precast piers and cap beams, respectively. Matsumoto et al. [5] studied two 0.42 scale column pier cap connections with one specimen designed for low ductility and the other one for high ductility. In these specimens, longitudinal reinforcement had to be threaded since the cap beam longitudinal reinforcements are not bundled. Both specimens developed a plastic hinge in the column; however, joint shear cracking was observed for the low ductility. Similarly, Mehraein and Saiidi [6] investigated the use of pocket connections in partially-cast column and precast cap beam testing two 0.27-scale two-column bents. One specimen was precast while the other specimen was CIP. The cap beam longitudinal reinforcement, in this case, was bundled outside the pocket joint allowing placement of column reinforcement easily and a spiral reinforcement was added in the pocket joint for additional confinement. The result shows that both specimens had developed plastic hinges in the column while the cap beam remained essentially elastic and capacity protected.

In columns with composite materials, Zhu et al. [7] and Motaref et al. [8] tested scaled columns using concrete-filled fiber reinforced polymer tubes (CFFT) and glass fiber reinforced polymer (GRFP), respectively. Zhu et. al [7] tested a variety of CFFT configurations both in CIP and precast columns and all specimens were connected to a footing through a pocket connection. The result showed better performance compared to a CIP column specimen. Motaref et. al [8] tested two-column bents with one column used regular concrete with engineering cementitious material (RC-ECC) in the plastic hinge zone while the other column used GRFP. The pockets were designed to be an octagonal shape and members were connected using grout. Both specimens were tested to failure and the results show satisfactory performance in the column and no damages were incurred in the footing and connection.

Haraldsson et al. [9], Tazarv and Saiidi [1], and Mohebbi et al. [2] examined the use of pocket connections with fully precast columns. Haraldsson [9] et al. investigated the performance of three 0.42 fully precast columns with CIP footing pocket connection. Two of the precast column specimens were constructed identically except one of the columns had a lower reinforcement ratio and the third specimen was designed to have a weaker footing. The pockets were designed to have an octagonal shape and the column to be embedded in the pocket were roughened to create more traction with CIP footing. Crushing of concrete in the plastic hinge zone occurred for the first two specimen while failure in the connection due to buckling of column longitudinal reinforcement and punching shear was observed for the third specimen.

Tazarv and Saiidi [1] formulated preliminary design guidelines based on different projects for cap beams and pocket connections. The proposed guideline was to design the pocket with helical lock-seam corrugated steel pipe and an equation was formulated to determine the minimum pocket requirement. Following standard AASHTO [10] design guidelines and results from previous ABC research, the cap beam longitudinal reinforcement was bundled outside the pocket joint to allow column placement without the need for threading of reinforcement. Additional transverse reinforcements in the pocket with the same volumetric ratio from the column transverse were recommended to be added on the lower half of the cap beam.

Mohebbi et al. [2] also developed design guidelines for square column-cap beam connection. A 0.33-scale square column model and a two-column bent were tested for that study. Both models utilized pocket connection wherein the single square column model used the pocket connection in the column-footing, while the two-column bent used such connections in all cap beam-column and column-footing connections. For both specimens, the damage was identified in the column developing a plastic hinge zone while the connection maintained its integrity. Recommendations were also established to: (1) bundle the cap beam longitudinal reinforcement around the joint to address shrinkage cracks and temperature, and (2) provide diagonal reinforcement in the square pocket to address cracking around the corners of the pocket.

Camarena et al. [11] investigated pocket connections with shape memory alloy (SMA) for CIP columns and cap beams. In this research, two-column bents with 1/3-scale were constructed with one column-cap connection designed in CIP pocket connections while the other column utilized an ABC pocket connection. Two-way hinges reinforced with Copper-Aluminum-Manganese (CAM) SMA bars at the base of both columns were designed. The bent specimen was tested on a shake table simulating a scaled ground motion of the Imperial Valley-02 earthquake event recorded at the El Centro Array #9 Station. The test showed that the pocket connection performed well as the joint did not exhibit any damage and plastic hinge develop within the columns. Utilizing two-way hinges reinforced with CAM revealed promising results as the structural integrity of the column bases remains intact with significant energy dissipation.

Schwartz et al. [4] investigated a CIP beam-column specimen emulating ABC pocket connection. A 1/3-scale model of a prototype bridge specimen was constructed with the cap beam placed in the bottom. The cap beam longitudinal reinforcement was bundled outside the pocket joint allowing the placement of the column uninhibited. Spiral confinement was added around the upper half and lower center of the pocket joint. The specimen was subjected to the 1994 Northridge Sylmar earthquake at an increasing scale. The column developed plastic hinge zone at the base while the cap beam remained capacity protected. The test specimen used in this latter study by Schwartz et al. [4] was further used in this study presented herein as explained in the next sections.

1.3. Project Phase I Overview

With the promising result of using ABC pocket connections in precast bridge structures, Schwartz et al. [4] utilized a similar idea in CIP reinforced concrete bridge structures. The work completed by Schwartz et al. [4] along with the work presented in this report complement each other and collectively form a two-phase project. The first phase is what was conducted and reported by Schwartz et al. [4] while the second phase is the work discussed in detail in this report.

In the first phase of the study, a large-scale specimen comprised of a cap beam and column was designed through an ABC pocket-inspired CIP connection. The main difference with traditional CIP is that the column and cap beam in the specimen were not precast. The specimen was configured based on a 1/3-scale model component of a prototype bridge where the cap beam was designed to have an I-shaped cross-section. Reinforcement details allowed the CIP pocket connection by bundling the cap beam reinforcement at both sides of the joint allowing the placement of the column reinforcement easily. Additional transverse hoops were added in the upper and lower half of the joint to ensure that confinement is achieved.

The cap beam and column specimen were constructed in two stages. In the first stage, the cap beam and the end blocks were formed and the reinforcements were placed. The column reinforcement cage was placed in the joint providing 15 in (381 mm) development for column longitudinal reinforcement. The concrete was cast in the cap beam including the portion of the column reinforcements in the pocket. The second stage was then executed by casting the concrete in the column specimen formwork including the loading head.

The specimen was tested using one ground motion that was selected from the NGA-West2 ground motion database developed by the Pacific Earthquake Engineering Research (PEER) Center. The selected ground motion was the 1994 Northridge earthquake acceleration history recorded at the Sylmar Converter Station in the 52^{o} direction. The record was scaled by an initial factor of 0.4065 so that the peak ground acceleration (PGA) of the earthquake record matched the PGA from the design response spectrum at the period of the specimen. The cap beam-column specimen was tested in an upside-down layout for a feasible shake table test setup under out-of-plane ground motion. A total of 11 runs at increasing scales of the design earthquake, which started from 20% up to 650%, were performed at the shake table.

The performance of the specimen was evaluated based on the measured displacement, force, acceleration, and reinforcement strain. The force-displacement showed good energy dissipation achieving high displacements in both pull and push directions despite the asymmetric behavior of the hysteresis. The acceleration measured from the cap beam web (underside) and the input ground motion were equivalently similar indicating no slippage of the specimen along the shake table. The strains also provided a good indicator of where steel reinforcement bars yielded in certain sections of the cap beam and the column parts of the specimen.

The first phase of the study, i.e. the part completed by Schwartz et al. [4], was able to draw conclusions based on the observed experimental results along with complementary analytical studies. The utilization of the ABC pocket connection improves the construction of CIP joints allowing the column cage reinforcement to be placed freely within the joint. The connection between the cap beam and column in the joint showed ductility and this is evident with the development of plastic hinge in the cap beam interface.

1.4. Objective and Scope

Using the specimen tested by Schwartz et al. [4] having no reinforcement interlocking the cap beam and the column, a repair method was developed and implemented to determine the effectiveness of the proposed joint in future seismic bridge repair using column replacement as opposed to full superstructure/substructure repair. The repair and re-testing of the specimen comprises the second phase of the project, which is the focus of this report. Accordingly, the part of the study presented herein has two main objectives: (1) to develop a repair method for the column specimen without damaging the cap beam reinforcement along with the construction of a new column for the repaired specimen, and (2) to test the repaired specimen under the same series of ground motions from Schwartz et al. [4] to check whether similar behavior would be observed.

To achieve the first objective, a repair method was developed focusing on the removal of the damaged column specimen in two steps. The first was to cut the column at the cap beam interface and the second was to core the embedded part of the old column in the joint. A new cast-in-place (CIP) column specimen was built with the reinforcements detail the same as that in the original specimen. Unlike to original specimen, the cap beam/column connection was not monolithic.

To achieve the second objective, the repaired specimen was tested under similar shake table testing conditions as the original specimen to verify whether the repaired specimen performed similarly to the original specimen. The loading protocol used in the original specimen was applied for this study. Several instruments were attached to the specimen to check whether plastic hinge formed in the cap beam interface and the joint remained essentially elastic, i.e. capacity-protected. In addition, the force-displacement was observed to investigate the energy dissipation and hysteretic behavior as discussed later in this report.

1.5. Report Outline

The report is organized into five chapters. Chapter 1 presents the introduction, an overview of the original test, and the objective and scope of the research of the repair test. Chapter 2 provides the repair and construction of the new column specimen, measured material properties, and the experimental test setup of the repaired specimen. Chapter 3 discusses the measured results from the shake table test including the observed damage and measured global and local behavior. Chapter 4 compares the behavior and results from the original test from Schwartz et. al [4] and the repaired specimen test. Finally, Chapter 5 provides summary and key conclusions of the study.

CHAPTER 2. EXPERIMENTAL PROJECT DEVELOPMENT

2.1. Introduction

The original column-cap beam specimen was repaired to validate the feasibility of the repair method and to compare the seismic performance of the new column–cap beam specimen with the original test. The repair process took place at the fabrication yard adjacent to the Earthquake Engineering Laboratory at the University of Nevada, Reno. The construction course was divided into two stages: (1) the removal of the existing tested and damaged column and coring of the column-cap beam joint, and (2) construction of a new CIP column into the cap beam. The first stage took place on March 25, 2021, and the second stage occurred between April 22 – May 3, 2021.

2.2. Construction

2.2.1 Removal of Original Column

To successfully repair the column-cap beam specimen, the existing column was removed. Strategically, cutting the column above the column cap beam interface was designed for easement of coring of the embedded column in the joint pocket. Coring of the joint pocket was planned accurately by measuring the diameter and embedded depth, which was used to select the required coring equipment. The plans and construction drawings for the cutting and coring of the column and joint specimen are shown in Figs. 2.1 to 2.4.

2.2.1.1 Cutting of Column Specimen

The existing column was removed by flush cutting the column at the column-cap beam interface. However, to preserve the cap beam portion of the specimen, the cut was performed approximately five inches above the column-cap beam interface. The remaining column fragments above the interface were manually removed. The cap beam specimen with the removed column above the interface is shown in Fig. 2.5.

2.2.1.2 Coring of Column-Cap Beam Joint

The joint pocket was removed carefully to accommodate the placement of the new column specimen. The joint was cored using a coring machine with a specified diameter of 16 in (406 mm) and a depth of 15 in (381 mm). Although the joint specimen was designed to have some allowance between the column and the bottom cap beam (the top portion in a real bridge), the 15 in. depth was conservatively chosen to avoid damaging the cap beam longitudinal reinforcement. The coring process is shown in Figs. 2.6 to 2.8. As noticed in the open pocket shown in Fig. 2.9, the coring was successful as the cap beam longitudinal reinforcement was not damaged and the depth was chosen correctly. The allowance between the joint and the cap beam was small due to original construction. Thus, the cap beam longitudinal reinforcement was exposed; however, the main objective is still satisfied as to the reinforcement at the bottom cap beam being preserved.

2.2.2 Construction of New Column

2.2.2.1 Reinforcement Details

A new column for the repaired specimen was designed exactly like the original specimen. Sixteen #4 column longitudinal reinforcement bars were placed evenly throughout the cross-section with #3 transverse spiral hoops pitched at 2.25 in. A loading head was also designed to allow the specimen to be attached to the mass rig needed for the shake table test (more details in following sections) using a rigid link connection. The ends of the column longitudinal reinforcement in the loading head were bent slightly at an angle to allow placement of four 2.25

in diameter PVC pipes. The pipes were used to allow the threaded rods to be inserted; thus, connecting the rigid link and the specimen. Figures 2.10 and 2.11 show the new column and loading head reinforcement details, respectively.

2.2.2.2 Construction Phase

After the column and loading head reinforcement details were established, the reinforcements were assembled as seen in Fig. 2.12. The formwork for the new column was constructed with a Sonotube placed on the cap beam and the joint. The new column reinforcement was placed using a forklift inside the Sonotube and through the cored joint. The placing of reinforcement is shown in Fig. 2.13. Concrete was then poured from the top of the loading head specimen. Casting, vibrating, and stripping of the formwork are shown in Figs. 2.14 to 2.16. Comparing the construction process from the original specimen, the casting process is different as the column reinforcement in the joint pocket of the original specimen was sitting in the concrete cast first together with the cap beam. The rest of the original column was filled with concrete afterward in a following stage which made a cold joint at the column-cap beam interface. The cap beam and column in the joint pocket were then connected through the concrete material. However, in this phase of the study, the repaired column was cast all at once at the same time. Thus, the cap beam and the column portion in the pocket did not have the same material, i.e. monolithic concrete.

2.3. Measured Material Properties

Samples from the material used were gathered on the day of the construction. The samples were taken to ensure that the specified properties of the material as per design were met and to compare also the concrete and reinforcement properties from the original specimen. The sampled materials included concrete cylinders and reinforcement steel coupons. Standard 6 in (152 mm) by

12 in (305 mm) cylinders were used to measure the compressive strength of the concrete. Nine cylinders were sampled from the concrete batch. The average compressive strength of the concrete was obtained at 7-day, 28-day, and the test day. Since the shake table test was conducted over two days, the average compressive strength was tested on the second day. Table 2.1 lists the average compressive strength of the concrete for each test day. Comparing the concrete properties for both the original and the repaired specimen, the compressive strength for the repaired column was higher on all test dates with 7.16 ksi (49.35 MPa) on the day of the shake table test.

The properties of the reinforcement steel were also tested based on the ASTM A370 Standard. Three coupons of #3 and #4 reinforcement bars were used for tensile tests. Figures 2.17 and 2.18 show the stress-strain diagram of the #3 and #4 reinforcement bars, respectively. The occasional jagged result in the stress-strain diagrams was caused because of some instantaneous test setup glitches or slippage of the reinforcement bars. The yield stress, ultimate stress, yield strain, and the ultimate strain were determined based on the stress-strain relationship. Table 2.2 summarizes the key stress and strain values determined from the material tensile tests.

2.4. Experimental Set up

Consistent with the original shake table test, the repaired specimen was set on the shake table as illustrated in the test setup diagrams in Figs. 2.19 and 2.20. The specimen was excited in the out-of-plane direction which aligned with the North-South direction of the laboratory. The specimen end blocks were elevated by 1.5 in (38 mm) above the shake table top surface to allow for grouting and leveling of the end blocks at both sides of the cap beam. Four threaded rods were passed through the PVC pipes at each end block, each tensioned at 30 kips (133 KN), to tie down the specimen to the shake table. The pretensioned rods ensure also that the specimen would not slip laterally throughout the test. A mass rig was used to model and simulate the inertial force of the specimen. Two 20 kips (89 KN) of mass concrete blocks were placed next to the shake table inside the mass rig and were connected to the specimen through a rigid link connector. The weight of the mass rig and rigid link contributed additional 20 kips which overall produced a total of 60 kips equivalent inertial mass. The rigid link comprised a load cell that measured the lateral force applied in the specimen. A whitewash was used to paint the column and cap beam to better observe the cracks and for the convenience of marking such cracks after each test run. Figure 2.21 shows the overall setup of the specimen on top of the shake table.

2.5. Instrumentation

The structural response of the specimen (both global and local) was captured using several instrumentations. The test data were collected from 127 channels that included strain gauges, string potentiometers, transducers, and accelerometers. In addition to sensors, video cameras were used to monitor the local and overall response of the specimen. All instrumentations were kept similar to the original test by Schwartz et al. [4]. However, eight strain gauges in the spiral hoops had to be removed when the original column was cut in the repairing process.

New strain gauges were attached on reinforcement bars at six sections within the column. The strain gauges were attached to the column longitudinal bars in the North-South direction as well as transverse spiral hoops. Overall, 52 new strain gauges were used in the repaired column. Transducers were also utilized to capture the displacements at certain sections of the specimen. The displacements were then used to calculate the curvature of the column and cap beam twist as discussed later in Chapter Three. Six string potentiometers were attached to the loading head and cap beam to determine the overall global displacements of the specimen under the applied ground motions. Three tri-axial accelerometers were placed on the top of the column, cap beam web, and cap beam underside to obtain and verify the acceleration experienced by the specimen. Each run was monitored by four GoPro Cameras focusing on the performance of the column-cap beam connection and two GoPro Cameras for both sides of the cap beam web. Two video cameras were positioned in the East-West direction to record the out-of-plane movement of the specimen as well as the behavior of the column for each run. A summary of the instrumentation plan and illustrative figures are presented in Table 2.3 and Figs. 2.22 through 2.26.

2.6. Loading Protocol

The loading protocol from the original test (Schwartz et al. [4]) was used for the shake table tests of the repaired specimen. The 1994 Northridge earthquake acceleration history recorded at the Sylmar Converter Station in the 52^o direction was simulated in the shake table tests. The record was scaled by an initial factor of 0.4065 so that the peak ground acceleration (PGA) of the earthquake record matched the PGA from the design response spectrum at the fundamental period of the specimen. Figure 2.27 shows the scaled acceleration history of the Northridge earthquake at the Sylmar Converter Station. The period of the specimen was calculated using the cracked section properties and was determined to be 0.574 sec. In the original test, the specimen period was mistakenly used to determine the scale factor instead of the prototype period; thus, the correct scale factor is 0.37. However, to accurately compare the results between the original and repair test, the initial factor of 0.4065 is still used.

Before each earthquake motion, a white noise motion was applied with an amplitude of 0.05g to be used for basic modal analysis to determine the vibration period and damping ratio of the specimen and track how these properties change as damage progressed. The overall test series included 12 seismic tests. Initially, the total number of runs expected to be conducted was 11 runs similar to the original test. However, the research team decided to perform another run to further push the specimen and observe the behavior of the specimen at full failure. Nevertheless, it is noted that in the occurrence of the 12th run, the displacement demands increased significantly and the laboratory staff decided to stop the test in the middle to avoid any damage to the test setup or the shake table. Figures 2.28 and 2.29 show the spliced acceleration history for all the runs. The intensity was increased in the original test and again in the repaired test until the specimen failed in order to develop the full hysteresis envelope. The loading protocol is summarized in Table 2.4 .

CHAPTER 3. EXPERIMENTAL RESULTS AND DISCUSSIONS

3.1. Introduction

A series of shake table tests were performed to evaluate the repaired ABC emulated column-cap beam connection under out-of-plane seismic loading. The shake table test was conducted on two consecutive days with the first seven runs on August 19, 2021, and the last five runs on August 20, 2021. This chapter presents the observed and measured performance of the repaired specimen.

3.2. Observed Damaged

Damage after each run within the typical plastic hinge zone and the cap beam web was observed by marking and documenting the cracks and spalling of the concrete. The damage was examined through drawing fine lines on the side of the cracks and marking them with different colors for each run. Photos from north, south, east, and west sides were taken to ensure that progression of damage was fully captured. Aside from the damage, the drift ratios for each run were also computed. The drift ratios were calculated by dividing the column displacement by the effective height of the column. The effective height of the column was 90 in (2286 mm) as measured from the column-cap beam interface to the loading head midheight, where the centroid of applied inertial load was located.

Initially, the cracks from the original test run were marked with a black line to ensure that the cracks from the repaired test are differentiated. Since run one was not expected to develop significant damage, the first two runs were performed consecutively without pausing the tests or marking the cracks. Figure 3.1 shows the onset flexural cracking within the plastic hinge zone after run two. The drift ratio of run #1 and run #2 were 0.11% and 0.41%, respectively. These drift ratios were low and did not cause visual damage in the column. More flexural cracks were observed after run #3 in the south side of the plastic hinge zone in the column as shown in Fig. 3.2, and new flexural cracks appeared on the upper part of the column as depicted in Fig. 3.3. Shear cracks were also noticed around the cap beam interface (Fig. 3.4). The maximum drift ratio in run #3 was 1.98%.

Runs #4 and #5, with drift ratios of 3.03% and 3.64%, respectively, caused more flexural cracks in the plastic hinge zone with some cracks expanding to the east and west side. The additional flexural cracks are evident in Fig. 3.5. In addition, shear cracks in run #4 were observed in the cap beam web shown in Fig. 3.6. In run #6, the flexural cracks in the south side started to expand as the drift ratio went up to 4.0%. Minor spalling had been observed in the north side of the column as well as the cap beam close to the plastic hinge zone. Figure 3.7 shows the spalling on the north side of the column. Shear cracks were detected on the east-side portion of the plastic hinge zone (Fig. 3.8) in that run. For run #7 with a drift ratio of 4.48 %, the spalling in the north side grew to expose portions of the spiral reinforcement (Fig. 3.9). In addition, onset of minor spalling in the south plastic hinge zone was observed. For runs #8 and #9, additional flexure cracks appeared throughout the column and with spalling growing in the south side. Additional shear cracks appeared in the cap beam interface (Fig. 3.10) as well as the cap beam web (Fig. 3.11). The drift ratio recorded for runs #8 and #9 was 4.67 % and 5.45 %, respectively.

In run #10, the specimen started to have significant damage concentrating in the plastic hinge zone. The column recorded a maximum drift ratio of 6.95% towards the north direction. The motion caused more flexure cracks to expand (Fig. 3.12) with additional spalling on the north side (Fig. 3.13). For run #11 with a drift ratio of 10.27%, the spalling in the north side grew larger with multiple spiral reinforcements exposed (Fig. 3.14). Additional flexure cracks and shear cracks also appeared on the east side (Fig. 3.15). The flexural cracks also expanded in the south portion of the plastic hinge zone. After run #11, one more additional run, i.e. run #12, using the same scaled motion that was applied in run #11. During run #12 while the earthquake motion was being applied, loud popping sounds indicating rupture of the column longitudinal rebars was heard. Thus, the laboratory staff decided to stop the test instantaneously before the full intended motion was completed to avoid any damage to the test setup or shake table. In this last run, significant damage was evident in both the north and south sides of the plastic hinge zone. The spalling of both sides of the plastic hinge zone can be seen in Figs. 3.16 and 3.17. The final column orientation and permanent drifts is shown in Fig. 3.18 where the column is seen to have permanently drifted towards the north side.

3.3. Measured Global Behavior

3.3.1 Shake Table Input Motion and Recorded Acceleration

The shake table feedback accelerations were compared to the target motions that were intended to reproduce a scaled acceleration history of the Northridge-Sylmar record. Table 3.1 compares the target and achieved peak ground acceleration (PGA) for each run. The accelerations for the shake table feedback and input motion differed within 15-37%, which was attributed to the mass and dynamics of the shake table itself along with the shake table-specimen interaction. The spectral acceleration at the top of the column, depicting a single-degree-of-freedom model, was measured and analyzed. In addition, the period of the specimen for each run was estimated using the Frequency Response Factor (FRF) determined from the white noise tests. The periods were used to determine the predicted and achieved linear-equivalent spectral acceleration. The predicted and achieved spectral accelerations (S_a) are shown in Table 3.2. The difference between the target and achieved spectral acceleration ranged from around 0.3% to 69% with average differences running around 44%. Figures 3.19 to 3.30 show the full target and achieved acceleration response spectra. Although there are differences in the spectral acceleration at the equivalent linear elastic period, the shape of the target and achieved spectral acceleration are similar after run #3. The spectral accelerations were also compared with the seismic design response spectrum in Fig. 3.31 for completeness.

The acceleration was also measured in three locations on the specimen during testing using three triaxial accelerometers. The accelerations for the x-direction (East-West), y-direction (North-South), z-direction (Top-Bottom) were filtered to remove high-frequency noise. The recorded accelerations for the x and z direction were very small and negligible compared to the y-direction, which is expected as the test was uniaxial tests. The accelerations of the cap beam underside were compared to the accelerations achieved by the shake table. Based on Fig. 3.32 that shows the stitched acceleration histories from all runs, both shake table and cap beam underside acceleration are identical confirming that the specimen did not slip during any of the tests. Figure 3.33 shows also the cap beam web acceleration where the recorded values were similar to the cap beam underside. The accelerations on top of the column were also observed to be decreasing in comparison with the cap beam acceleration. Figure 3.34 plots the top column acceleration. The smaller acceleration at higher runs can be attributed to the yielding of the column; thus, acceleration from the shake table was not fully transmitted.

3.3.2 White Noise Tests

A white noise motion with 5%g RMS amplitude was applied to the specimen before and after each run. All white noise motions were executed except after run 12 as some of the column reinforcements had already ruptured. The response of the specimen through the acceleration at the top of the column was used to obtain the fundamental vibration period . As mentioned earlier, the

FRF of the top column acceleration was used to determine the period. In determining the frequency and period, the first dominating peak in the frequency domain from each test was determined. Table 3.4 summarizes the period as calculated from FRF method...

3.3.3 Displacement and Drift Ratio

The displacements were recorded at the loading head and the cap beam of the specimen. The displacements from the string potentiometers attached to the loading head were filtered and the average was obtained. The relative displacement of the column was calculated by subtracting the shake table displacement, as obtained from the table actuator transducer, from the average top column displacement. Figure 3.35 shows the column displacement for each run. In addition, Table 3.5 lists the residual displacement of the column for each run. A positive residual displacement indicates that the column shifts toward the south direction while a negative residual indicates a displacement in the north direction. As observed, runs #1 to #3 indicated only small residual displacements towards the south. However, after run #4, the residual displacement shifted towards the north direction. The residual displacements in the north direction significantly increased especially after run #11 where the residual value was 6.77 in (172 mm) or 10.27% drift ratio. However, after run #12, the residual displacement increased more to 16.16 in (411 mm). This high residual value can be attributed to the failure of the column longitudinal reinforcement and the weakening of the column cap beam connection, which both led to a significant drop in the lateral stiffness.

The displacement from the top and bottom cap beam were also captured to measure the movement of the cap beam. Similar to the displacements from the loading head, the cap beam displacements were filtered and shown in Fig. 3.36. To compare with the cap beam string potentiometers, the Novatechnik transducers attached at both sides of the cap beam were also recorded to measure the cap beam displacement. The effect of cap beam torsional flexibility on the overall displacement of the column was determined based on the calculated angle of twist. The measured displacement obtained from the vertical transducers attached at the two sides of the bottom flange were subtracted and the difference was divided by the distance between the two transducers, i.e., the total width of the simulated cap beam flange. The calculated cap beam twist was then multiplied with the effective rotational height, which is the length of the cap beam center rotation and the effective column height. Figure 3.37 shows the cap beam displacement from Novatechnik transducers. The cap beam string potentiometers did not provide an accurate displacement due to the small readings within the sensors sensitivity. However, the readings of the cap beam displacement from the transducers were accurate and provided a better representation of the displacement.

3.3.4 Force-Displacement Relationship

The force-displacement behavior was analyzed to determine the performance of the specimen. The force-displacement hysteresis loops provide a good indicator of the performance in terms of the amount of energy dissipated, column reinforcement yielding, and force-displacement capacities. Similar to the original test, the lateral force was measured using the load cell connected within the rigid link. The relative displacements calculated previously in section 3.3.3 were used. Consistent with the sign convention for the residual displacement, a positive displacement indicates a movement in the south direction while a negative displacement indicates a movement in the north direction. The force-displacement hysteresis loops for each run were obtained and plotted in Figs. 3.38 to 3.49.

The hysteresis loops for runs #1 and #2 in Fig. 3.38 and 3.39 indicate a linear behavior with relatively small energy dissipation. During run #3, the hysteresis loops started to behave in a nonlinear manner as the recorded lateral force started to increase compared to the initial runs. Figure 3.40 shows the hysteresis loops for run three. The hysteresis loops were also observed to be relatively asymmetric with displacement occurring on the south side. In runs #4 and #5 shown in Fig 3.41 and Fig. 3.42, respectively, the hysteresis grew wider indicating a relatively higher energy dissipation. In addition, the column displacement gradually started to shift towards the north direction. The hysteresis curves for runs #6, #7, and #8 continued to widen as shown in Figs. 3.43 to 3.45. In addition, the hysteresis started to show more asymmetric behavior as displacements in the negative (north) direction gradually increased.

The asymmetric behavior became more evident in runs #9 and #10. Figures 3.46 and 3.47 show the hysteretic behavior of the column specimen for runs #9 and #10, respectively. As observed in the plot, the hysteresis becomes wider indicating a high energy dissipation. The high energy dissipation was consistent with the plastic hinge forming in the column close to the cap beam interface as required by design. The displacement consistently grew higher in the north direction with no increase in the displacement in the south direction. In run #11 shown in Fig. 3.48, the asymmetric behavior of the hysteresis loop became wider with higher displacements occurring in the north direction. The hysteresis also shifted from the origin indicating large residual displacements. Lastly, the force-displacement relationship for run 12 was obtained and plotted in Fig. 3.49. Since the ground motion was incomplete due to sudden test stop when severe rupture of the column longitudinal reinforcement was heard, the force-displacement relationship shown in the figure provides the hysteretic behavior only up to the stopping point. In addition, because of the rupture in the column reinforcement, higher displacements were recorded with a significant decrease in the lateral force capacity.

The envelope of the force-displacement relationship for the specimen was also determined based on the cumulative hysteresis curve of runs #1 through #12. Figure 3.50 shows the envelope in both north and south directions. Since the majority of the force-displacement hysteresis is asymmetric and residual displacements occurred in the north direction, the envelope from the negative (north direction) displacements was used to develop the “experimental pushover curve”. In addition, the idealized pushover curve was identified by first projecting an elastic region by passing a line through the first yielding of the column longitudinal reinforcement. The plastic region was then estimated by equalizing the area from the plastic region of the actual pushover curve. Figure 3.51 shows the experimental and idealized pushover curve. The effective yield point was determined to be 17.54 kips (78 kN) at 2.0 in (51 mm) displacement.

3.4 Measured Local Behavior

3.4.1 Strains

The maximum (or minimum based on sign) strains were recorded at different locations in the specimen. The strain gauges were attached to the column and cap beam reinforcement at various locations as shown before in section 2.5 and the recorded maximum and minimum strains are summarized in Tables 3.8 through 3.17 for all runs. In the strain measurements, a positive strain shows compression while a negative strain indicates tension. Strain gauges were placed at six sections of the column on the longitudinal and transverse reinforcement. The strain gauges were placed 9” (229 mm) and 4.5” (114 mm) below the cap beam interface, right at the cap beam interface, and 6” (152 mm), 12” (305 mm), and 18” (457 mm) above the cap beam interface. In the column longitudinal reinforcement, no yielding occurred for runs #1 and #2. During run #3, all instrumented sections showed reinforcement yielding with largest strains occurred in the plastic hinge zone. Yielding extended in all instrumented sections of the column longitudinal reinforcement. However, some strain gauges were damaged during higher runs and no valid strains were not recorded in such cases. Tables 3.8 through 3.10 show the complete peak strain measurements for the column longitudinal reinforcement. Similarly, the strains at the transverse hoops were also recorded at five sections in the column. The transverse hoops did not yield until run #11, at which yielding occurred below and above the cap beam interface. Tables 3.11 through 3.13 show the maximum and minimum strain in the transverse hoops.

Since the reinforcements from the cap beam were preserved during the repair process, the strain gauges that were previously attached to the reinforcements were utilized. Tables 3.14 through 3.17 show the strain recorded for the cap beam longitudinal and transverse reinforcement. In the cap beam longitudinal reinforcement, no yielding was noted throughout the test. In addition, higher strain but still in the elastic region occurred in several horizontal ties near the pocket, and the maximum tensile strain for such was recorded to be 71% of the yield strain. The recorded maximum tensile strain in the instrumented stirrups was measured to be 56% of the yield strain which was measured in the stirrup located outside the pocket joint.

3.4.2 Column Curvature and Rotation

The curvature in the plastic hinge region of the column was calculated from the measurements obtained from the transducers placed along the direction of loading. Similar to the original test, four pairs of Novatechnik displacement transducers were used to estimate the curvature in four column sections within the plastic hinge zone. The curvature at each pair in the plastic hinge zone was calculated using Equation 3-1 and the rotation using Equation 3-2.

$$\phi_i = {\left(\frac{\Delta_{i,1}}{l_{i,1}} - \frac{\Delta_{i,2}}{l_{i,2}}\right)} \Big/ {\left(x_{i,1} + \mathrm{D} + x_{i,2}\right)} \qquad (3\text{-}1)$$

$$\theta_i = {(\Delta_{i,1} - \Delta_{i,2})}\Big/{(x_{i,1} + \mathrm{D} + x_{i,2})} \tag{3-2}$$

where, ϕ_i is the average curvature at section i, θ_i is the average rotation at section i, $\Delta_{i,1}$ and $\Delta_{i,2}$ are measured displacements from transducers at section i, $l_{i,1}$ and $l_{i,2}$ are gauge lengths at section i, $x_{i,1}$ and $x_{i,2}$ are the distance from column face to the transducers at section i, and D is the column diameter.

The curvature profile obtained from runs #1 through #12 is shown in Fig.3.52. High curvatures were observed at the column-beam interface indicating formation of plastic hinge in this region. In addition, the curvature was also observed to decrease as the distance gets farther away from the cap beam interface. The minimum and maximum rotation were also determined and were plotted in Fig. 3.53. A positive rotation indicates rotation towards the north while a negative rotation shows rotation in the south direction. In runs #1 through #3, positive and negative rotations were approximately equal indicating rotations in both directions. However, in runs #4 through #12, the rotation in the north direction was more dominant. As observed, the maximum rotation in most of the runs was higher compared to the minimum rotation because of the asymmetric displacement behavior of the response in the north direction.

CHAPTER 4. COMPARISON BETWEEN ORIGINAL AND REPAIRED SPECIMENS

4.1 Introduction

The results of the original tests performed by Schwartz et al. [4] were compared to the results obtained from the repaired specimen tests. The objective of this section is to analyze whether the repaired specimen performed similarly to the original specimen and to determine the effectiveness of the proposed method in future seismic bridge repair using column replacement as opposed to full superstructure repair. To establish the performance of the repaired specimen, the observed damage and measured data in the repaired and the original specimens were compared. The comparison in this chapter also provides the basis for the brief design recommendations listed in the next chapter for future repair of CIP bridge specimen emulating ABC pocket connection.

4.2 Cap Beam Behavior

The cap beam remained essentially elastic throughout the tests in both specimens and behaved as a capacity-protected member as required by design, with minor shear and torsional cracks in the cap beam interface and the web. The top diagonal cracks in the west and east side of the cap beam interface close to the pocket joint were present before the repaired specimen was tested. After applying the high-amplitude motions to the repaired specimen, these shear cracks grew wider as shown in Fig. 4.1. However, the damage was not significant as the reinforcements in the cap beam remained linear elastic and there was no spalling of concrete. The cap beam reinforcement did not yield. In addition, the maximum strains along the cap beam were measured and compared for both specimens. Figure 4.2 compares the recorded maximum strains in both specimens along the cap beam. As noticed, the maximum strain recorded in the stirrup (18 in away from the cap beam centerline) grew higher relative to other stirrups along the cap beam, which was 63% of the yield strain.

4.3 Column Behavior

The visual damage in the column was compared for both the original and repaired test. In the first five runs, damage in both original and new columns was limited mostly to flexural cracks and was most evident in the north and south of the plastic hinge zone. In run #6, minor concrete spalling occurred for both specimens; however, spalling appeared in the south section in the original column specimen while spalling was observed in the north section of the repaired column specimen. Column flexural cracks and damage continued to expand in the plastic hinge zone after run #6 with some additional shear crack formation for both column specimens. However, one noticeable difference between the damage in the columns was the significant concrete spalling in the north section of the repaired specimen. Figures 4.3a and 4.3b compare the concrete spalling in the north section. As observed, transverse reinforcements in the repaired specimen were uncovered while no reinforcement was exposed in the original test. In the south section, similar damages were observed with wide flexural cracks within the plastic hinge zone. Figures 4.3c and 4.3d show the comparison of the damage for both specimens in the south section. As noticed, the flexural cracks were wider in the repaired specimen compared to the original specimen. No reinforcement exposure in the south section was observed for both specimens.

To further understand the damage incurred in the plastic hinge zone, the drift ratios were compared. Figure 4.4 shows the comparison of the maximum drift ratio for both column specimens. As observed in runs #1 through #9, the drift ratio in the original column specimen was slightly higher compared to the repaired column specimen. The result can be attributed to the material properties of the column specimen where the concrete compressive strength of the repaired column specimen was higher than the original column specimen (see section 2.3) suggesting that the repaired column specimen was stronger. However, in runs #10 and #11 where scaled ground motion was larger, the drift ratio of the repaired specimen was higher. Because of this higher drift ratio recorded in the north direction, major spalling in the plastic hinge zone had been observed since the north section was significantly being compressed crushing the unconfined concrete. On the contrary, the south section of the column plastic hinge zone goes through tension which formed larger flexural cracks.

4.4 Connection Behavior

To determine the effectiveness of the repair method, the connection behavior in the original and repaired specimens were compared. The maximum curvature determined from the base transducers is plotted in Fig. 4.5. As observed, the curvature at the base of the repaired column specimen was higher compared to the original column specimen. Furthermore, as the ground excitation intensity became larger, the difference between the curvatures increases, e.g. a factor of 2.2 and 2.6 of curvature increase is noted for runs #10 and #11. The column base rotations were also compared. Figure 4.6 shows the angle of rotation of the column specimen for both tests. The trend is also similar with the curvature wherein the rotation difference recorded in both column specimens increased at higher ground motion intensity, e.g. a factor of 2.7 and 3.2 of rotation increase is noted for runs #10 and #11.

As discussed in chapter 2, the main difference between the specimens was the connection mechanism between cap beam and column. In the original column specimen, the column reinforcement was sitting in two different concrete casts as the column concrete was poured in two stages. The column reinforcement bars were anchored in the same monolithic concrete cast as the cap beam then the rest of the column was cast later with a cold joint at the column-cap beam interface. However, in the repaired specimen, the full column was cast all in one stage into the cored joint, with smooth concrete surface. These construction differences significantly led to the higher rotation and curvature of the repaired column specimen. To address this issue, it is recommended that the surface of the cored joint be roughened prior to casting the new column.

CHAPTER 5. SUMMARY, CONCLUSIONS, AND RECOMMENDATIONS

5.1 Summary

Accelerated bridge construction (ABC) has been advancing as one of the emerging technologies in construction and design because of its effective way to reduce the on-site time needed for construction and associated traffic delays or shutdowns. Several studies were conducted to evaluate a variety of ABC pocket and socket connections utilizing partial and fully precast members. The successful validation of such connection inspired the consideration of ABC-like connections in CIP connections. In conventional CIP bridge construction, one of the main issues is the congestion of the reinforcement in the joint. This is because of the intercrossing column and cap beam reinforcement in the joint. ABC pocket/socket connection separates the column and cap beam bars thus avoiding joint reinforcement congestion. In an earlier phase of this project, a CIP cap beam-column connection detail that separated column and cap beam bars was developed and validated in out-of-plane testing of a large-scale model tested on a shake table to failure. The objective was to simplify the construction of CIP bridge using the guidelines for detailing an ABC pocket connection. To achieve this goal, the cap beam longitudinal reinforcements were bundled outside the pocket allowing the placement of column longitudinal reinforcement in the pocket uninhibited. The specimen was tested under increasing scale of a recorded ground motion. The earthquake ground motion used for the shake table test series was adopted from the 1994 Northridge earthquake recorded at the Sylmar Converter Station in the H1 component. The plastic hinge in the specimen was formed at the column immediately above the cap beam, and showed plastic hinge formation at the column, while the cap beam remained essentially elastic. The joint damage was minimal. This demonstrated that the new joint detailing method was successful.

In the second phase of the project presented in this report, the main objective was to determine the effectiveness of repairing the specimen by replacing the column while maintaining the original cap beam. The repaired model was subjected to the same shake table testing loading protocol as that of the original specimen. The repair process began by flush cutting the damaged column near the cap beam interface. Since no reinforcements connected the cap beam and the column, the remaining embedded portion of the original column within the pocket joint was removed by coring. A new column specimen was constructed using the same reinforcement detailing as the original column and was placed in the cored joint. Concrete was cast into the formwork and a newly repaired column was constructed. The main difference in this repaired specimen from the original model was that the column was cast monolithically while the original column was cast first in two stages; first the column portion in the joint cast with the cap beam then the rest of the column and the loading head was cast later.

The strain, displacement, force, acceleration data from each scaled ground motion was recorded using 121 different sensors and instruments. Observed damage was noted after each run and the measured global and local behavior was analyzed. The performance of the repaired specimen was compared to the original model based on which recommendations are made for future repair cases.

5.2 Conclusions

The following conclusions were drawn based on the results from the repaired process, shake table tests results, and data interpretations and analysis:

1. Since no reinforcements are interlocking the cap beam and column, the original specimen was efficiently repaired by initially flush cutting the damaged column and by coring the embedded column reinforcement inside the pocket joint. The depth and diameter of the

coring was possible to determine accurately without damaging the reinforcement bars surrounding the pocket joint.

2. The repaired specimen performed well under the out-of-plane seismic excitations and ductility was achieved through the formation of plastic hinge zone in the column immediately adjacent to the cap beam. The cap beam remained essentially elastic (capacity protected) throughout all the tests with only minor cracks formed around the column-cap beam interface.
3. The repaired specimen achieved comparable drift ratios for earthquake levels of 20% to 450%. However, under larger ground motions, i.e. 550% and 650% scale runs, the drift ratios were significantly higher than the original column, which can be attributed to the extra rotation of the repaired column in the joint.
4. To avoid the issue indicated in Conclusion 3, it is recommended that the cored pocket joint surface be roughened to strengthen the bond between the cap beam and column. This would improve the connectivity between the column and the joint even under very strong earthquakes.

5.3 Recommendations

Since there are no existing guidelines on how to repair and replace a bridge column in the case of the new proposed emulative ABC pocket connection for CIP construction, the following recommendations are provided based on the results of this study:

1. The depth and diameter of the coring machine should be carefully selected to preserve the cap beam longitudinal reinforcements as well as the transverse reinforcements surrounding the cap beam.

2. The internal surface of the cored joint should be roughened to achieve sufficient bond between the existing cap beam and the new column.

REFERENCES

[1] Tazarv, M., Saiidi, M. (2015) “Design and Construction of Precast Bent Caps with Pocket Connections for High Seismic Regions.” Center for Civil Engineering Earthquake Research, Department of Civil and Environmental Engineering, University of Nevada, Reno, Report No. CCEER 15-06.

[2] Mohebbi, A., M. Saiidi, and A. Itani, “Seismic Design of Precast Piers with Pocket Connections, CFRP Tendons, and ECC/UHPC Columns,” International Journal of Bridge Engineering, Special Issue: Experimental and Analytical Investigations with Emerging Bridge Design Methods, October 2017, pp. 99-123.

[3] Mehrsoroush, A., Saiidi, M., and Ryan, K. (2017). “Development of EarthquakeResistant Precast Pier Systems for Accelerated Bridge Construction in Nevada.” Center for Civil Engineering Earthquake Research, Department of Civil and Environmental Engineering, University of Nevada, Reno, Report No. CCEER-17- 03.

[4] Schwartz, T., Saiidi, M., and Moustafa, M., (2020) “Simplifying Cast-in-Place Joint Design Using ABC Pocket Connection Details in High Seismic Regions,” Center for Civil Engineering Earthquake Research, Department of Civil and Environmental Engineering, University of Nevada, Reno, Nevada, Report No. CCEER-20-0.

[5] Matsumoto, E. E., Waggoner, M. C., Sumen, G., and Kreger, M. E. (2001). “Development of a Precast Bent Cap System.” Center for Transportation Research, University of Texas at Austin, Report No. FHWA/TX-0-1748-2.

[6] Mehraein, M., and M. Saiidi, “Seismic Performance and Design of Bridge Column-to-Pile-Shaft Pipe-Pin Connections in Precast and Cast-in-Place Bridges,” Earthquake engineering and Structural Dynamics, Published Online, August 2019, Vol. 48, Issue 13, October 2019, pp. 1471-1490.

[7] Zhu, Z., Ahmad, I., and Mirmiran, A. (2006). “Seismic Performance of Concrete Filled FRP Tube Columns for Bridge Substructure.” Journal of Bridge Engineering, 11(3), 359-370.

[8] Motaref, S., Saiidi, M., and Sanders, D. (2011) “Seismic Response of Precast Bridge Columns with Energy Dissipating Joints.” Center for Civil Engineering Earthquake Research,

Department of Civil and Environmental Engineering, University of Nevada, Reno, Report No. CCEER 11-01.

[9] Haraldsson, O. S., Janes, T. M., Eberhard, M. O., and Stanton, J. F. (2013). "Seismic Resistance of Socket Connection between Footing and Precast Column." Journal of Bridge Engineering, 18(9), 910-919. 69

[10] American Association of State Highway and Transportation Officials (AASHTO) (2017). "AASHTO LRFD Bridge Design Specifications (8th Ed.)," Washington, D.C.

[11] Camarena, C., Saiidi, M., and Moustafa, M. (2020), "Development and Seismic Evaluation of Cast-In-Place Emulating ABC Pocket Connections and SMA Reinforced Two-Way Column Hinges."Center for Civil Engineering Earthquake Research, Department of Civil and Environmental Engineering, University of Nevada, Reno, Report No. CCEER 20-06

[12] ASTM International, (2017) "Standard Test Methods and Definitions for Mechanical Testing of Steel Products." A370-17a, West Conshohocken, PA.

CHAPTER 2 TABLES

Table 2.1 Concrete test results

Project Description:	7-day, ksi (MPa)	28-day, ksi (MPa)	Test day, ksi (MPa)	Test day age, days
AEC-OP (Original Column)	3.94 (27.2)	5.20 (35.9)	6.18 (42.6)	46
AEC-OP-R (Repaired Column)	4.57 (31.52)	6.13 (42.27)	7.16 (49.35)	109

Table 2.2 Reinforcement test results

Bar Size	f_y , ksi (MPa)	f_u , ksi (MPa)	ε_y , in/in	ε_u , in/in
#3	63.9 (441)	98.6 (680)	0.00487	0.1222
#4	72.7 (501)	95.0 (655)	0.00329	0.1209

Table 2.3 Overall instrumentations

Instrument	Lab Name	Quantity	Number of Channels
Strain Gauges (YEFLAB)	-	96	96
String Potentiometers	UniMeasure PA40 and PA60	6	6
Accelerometer	320 Triax Mem	3	9
Novotechnik	TR 75 and TR 100	10	10
GoPro Cameras	-	4	4
Video Camers	-	2	2

Table 2.4 Loading protocol

Run #	Test Type	PGA (g)	Factor
WN 1	White Noise		
1	Sylmar - H1	0.06	0.08
WN 1	White Noise		
2	Sylmar - H1	0.13	0.20
WN 1	White Noise		
3	Sylmar - H1	0.25	0.41
WN 1	White Noise		
4	Sylmar - H1	0.38	0.61
WN 1	White Noise		
5	Sylmar - H1	0.51	0.81
WN 1	White Noise		
6	Sylmar - H1	0.63	1.02
WN 1	White Noise		
7	Sylmar - H1	0.76	1.22
WN 1	White Noise		
8	Sylmar - H1	0.89	1.42
WN 1	White Noise		
9	Sylmar - H1	1.15	1.83
WN 1	White Noise		
10	Sylmar - H1	1.41	2.24
WN 1	White Noise		
11	Sylmar - H1	1.66	2.64

CHAPTER 3 TABLES

Table 3.1 Target and achieved peak ground acceleration

Run No.	Peak Ground Acceleration, PGA, g		Difference, %
	Target	Achieved	
Run 1	0.05	0.03	37.00
Run 2	0.13	0.09	27.38
Run 3	0.25	0.22	13.96
Run 4	0.38	0.32	17.00
Run 5	0.51	0.42	18.12
Run 6	0.63	0.53	16.11
Run 7	0.76	0.62	18.72
Run 8	0.89	0.74	16.48
Run 9	1.14	0.91	20.50
Run 10	1.39	1.17	15.71
Run 11	1.65	1.41	14.59
Run 12	1.65	1.35	18.37

Table 3.2 Predicted and achieved spectral acceleration

Run No.	Spectral Acceleration, S_a, g		Difference, %
	Predicted	Achieved	
Run 1	0.13	0.04	68.07
Run 2	0.18	0.14	20.57
Run 3	0.26	0.16	38.76
Run 4	0.39	0.22	44.48
Run 5	0.52	0.29	45.36
Run 6	0.65	0.36	44.66
Run 7	0.79	0.43	44.71
Run 8	0.92	0.51	44.37
Run 9	1.18	0.65	44.55
Run 10	1.44	0.80	44.38
Run 11	1.64	1.63	0.31

Table 3.3 Maximum accelerations at different locations

Absolute Maximum Accelerations, g				
Run No.	Shake Table	Cap Beam (underside)	Cap Beam (web)	Column
Run 1	0.03	0.04	0.04	0.05
Run 2	0.09	0.09	0.09	0.10
Run 3	0.22	0.22	0.22	0.35
Run 4	0.32	0.32	0.32	0.40
Run 5	0.42	0.43	0.42	0.44
Run 6	0.53	0.53	0.52	0.45
Run 7	0.62	0.63	0.62	0.45
Run 8	0.74	0.73	0.72	0.46
Run 9	0.91	0.93	0.92	0.47
Run 10	1.17	1.17	1.15	0.46
Run 11	1.41	1.42	1.41	0.48
Run 12	1.35	1.39	1.37	0.46

Table 3.4 Fundamental periods determined from white noise tests

Run No.	Period (FRF), sec
Run 1	0.530
Run 2	0.750
Run 3	1.130
Run 4	1.140
Run 5	1.140
Run 6	1.140
Run 7	1.140
Run 8	1.140
Run 9	1.140
Run 10	1.140
Run 11	0.890

Table 3.5 Column residual displacement after different runs

Run No.	Residual Displacement, in (mm)
Run 1	0.01 (0.23)
Run 2	0.03 (0.65)
Run 3	0.10 (2.45)
Run 4	-0.10 (-2.57)
Run 5	-0.32 (-8.11)
Run 6	-0.43 (-11.0)
Run 7	-0.50 (-12.7)
Run 8	-0.75 (-19.0)
Run 9	-1.42 (-36.15)
Run 10	-3.11 (-79.0)
Run 11	-6.77 (-172.0)
Run 12	-16.16 (-410.42)

Table 3.6 Maximum measured drifts, displacements, and forces

Run No.	Max. Drift Ratio, %	Max. Column Disp. in. (mm)	Max. Base Shear, kips (kN)
Run 1	0.11	0.10 (2.6)	2.56 (11.4)
Run 2	0.41	0.37 (9.3)	4.74 (21.1)
Run 3	1.98	1.78 (45.2)	15.47 (68.8)
Run 4	3.03	2.73 (69.2)	17.71 (78.8)
Run 5	3.64	3.27 (83.1)	17.77 (79.0)
Run 6	4.00	3.60 (91.4)	17.91 (79.7)
Run 7	4.48	4.03 (102.4)	18.11 (80.6)
Run 8	4.67	4.20 (106.7)	17.71 (78.8)
Run 9	5.45	4.91 (124.7)	17.41 (77.4)
Run 10	6.95	6.25 (158.8)	16.94 (75.4)
Run 11	10.27	9.24 (234.8)	18.11 (80.6)
Run 12	18.88	16.99 (431.5)	18.70 (83.2)

Table 3.7 Cap beam twist contribution to column displacement

Run No.	Column Displacement, in (mm)		Cap Beam Twist Contribution, Percent
	Due to Cap Beam Twist	Overall	
Run 1	0.02 (0.3)	0.10 (2.6)	23.02
Run 2	0.05 (0.7)	0.37 (9.3)	13.79
Run 3	0.23 (2.7)	1.78 (45.2)	12.75
Run 4	0.28 (3.8)	2.73 (69.2)	10.39
Run 5	0.30 (4.2)	3.27 (83.1)	9.04
Run 6	0.31 (4.7)	3.60 (91.4)	8.61
Run 7	0.32 (5.0)	4.03 (102.4)	7.83
Run 8	0.31 (5.2)	4.20 (106.7)	7.41
Run 9	0.31 (5.4)	4.91 (124.7)	6.33
Run 10	0.30 (5.7)	6.25 (158.8)	4.82
Run 11	0.34 (6.7)	9.24 (234.8)	3.67
Run 12	0.38 (6.7)	16.99 (431.5)	2.22

Table 3.8 Column longitudinal reinforcement strain data at 9 in and 4.5 in inside the cap beam (values reported in microstrains)

Location	Column, 9" (229 mm) Inside Cap Beam											
Gauge No.	SG 1		SG 2		SG 3		SG 4		SG 5		SG 6	
Bar Type	Longitudinal		Longitudinal		Longitudinal		Longitudinal		Longitudinal		Longitudinal	
Run No.	Max	Min	Max	Min	Max	Min	Max	Min	Max	Min	Max	Min
Run 1	41.1	-61.6	-	-	124.0	-165.0	75.6	-61.9	68.7	-75.6	75.6	-41.2
Run 2	89.0	-157.0	-	-	213.0	-845.0	131.0	-158.0	131.0	-151.0	117.0	-131.0
Run 3	274.0	-2230.0	-	-	763.0	**-2950.0**	289.0	-2700.0	378.0	**-2950.0**	213.0	**-2850.0**
Run 4	958.0	**-2960.0**	-	-	-	-	536.0	**-3070.0**	337.0	**-4300.0**	282.0	**-3440.0**
Run 5	1100.0	**-3050.0**	-	-	-	-	791.0	**-3130.0**	-227.0	**-5280.0**	460.0	**-3650.0**
Run 6	1290.0	**-2980.0**	-	-	-	-	935.0	**-3200.0**	-556.0	**-6770.0**	591.0	**-3870.0**
Run 7	1400.0	**-2930.0**	-	-	-	-	1020.0	**-3320.0**	-1110.0	**-8620.0**	612.0	**-4160.0**
Run 8	1460.0	**-2980.0**	-	-	-	-	1070.0	**-3390.0**	-1710.0	**-9420.0**	667.0	**-4320.0**
Run 9	-	-	-	-	-	-	1180.0	**-3530.0**	-1750.0	**-10100.0**	735.0	**-4460.0**
Run 10	-	-	-	-	-	-	1290.0	**-3520.0**	-1760.0	**-10100.0**	783.0	**-4330.0**
Run 11	-	-	-	-	-	-	1390.0	**-3420.0**	-1700.0	**-9810.0**	893.0	**-4130.0**
Run 12	-	-	-	-	-	-	1400.0	**-3050.0**	-1720.0	**-8710.0**	996.0	**-3680.0**

Location	Column, 4.5" (114 mm) Inside Cap Beam											
Gauge No.	SG 11		SG 12		SG 13		SG 14		SG 15		SG 16	
Bar Type	Longitudinal		Longitudinal		Longitudinal		Longitudinal		Longitudinal		Longitudinal	
Run No.	Max	Min	Max	Min	Max	Min	Max	Min	Max	Min	Max	Min
Run 1	61.8	-89.3	61.9	-82.5	124.0	-103.0	103.0	-82.4	96.2	-54.9	96.2	-61.8
Run 2	158.0	-426.0	151.0	-268.0	220.0	-1090.0	240.0	-460.0	213.0	-234.0	186.0	-295.0
Run 3	467.0	-2760.0	619.0	-2690.0	776.0	**-3220.0**	618.0	**-3670.0**	618.0	**-9000.0**	357.0	**-3220.0**
Run 4	1660.0	**-3950.0**	1000.0	**-4080.0**	-	-	495.0	**-7080.0**	**-3200.0**	**-14700.0**	330.0	**-4510.0**
Run 5	1830.0	**-7300.0**	1180.0	**-9580.0**	-	-	-653.0	**-13000.0**	**-4420.0**	**-16500.0**	192.0	**-10700.0**
Run 6	1260.0	**-8800.0**	-	-	-	-	-2060.0	**-17500.0**	**-3430.0**	**-17300.0**	**-3130.0**	**-15400.0**
Run 7	928.0	**-9760.0**	-	-	-	-	**-2660.0**	**-21200.0**	**-3280.0**	**-19700.0**	**-4810.0**	**-19100.0**
Run 8	673.0	**-10300.0**	-	-	-	-	**-2750.0**	**-21100.0**	**-2740.0**	**-21200.0**	**-6240.0**	**-21600.0**
Run 9	-	-	-	-	-	-	**-2870.0**	**-22300.0**	-	-	**-6980.0**	**-24900.0**
Run 10	-	-	-	-	-	-	-	-	-	-	**-7670.0**	**-25800.0**
Run 11	-	-	-	-	-	-	-	-	-	-	**-7830.0**	**-25000.0**
Run 12	-	-	-	-	-	-	-	-	-	-	**-8710.0**	**-20600.0**

Table 3.9 Column longitudinal reinforcement strain data right at and 6 in above cap beam (values reported in microstrains)

Location	Column, At Cap Beam Face											
Gauge No.	SG 21		SG 22		SG 23		SG 24		SG 25		SG 26	
Bar Type	Longitudinal		Longitudinal		Longitudinal		Longitudinal		Longitudinal		Longitudinal	
Run No.	Max	Min	Max	Min	Max	Min	Max	Min	Max	Min	Max	Min
Run 1	117.0	-117.0	110.0	-165.0	96.2	-117.0	124.0	-144.0	165.0	-144.0	144.0	-117.0
Run 2	268.0	-1150.0	323.0	-1480.0	185.0	-1110.0	357.0	-1100.0	412.0	-1260.0	295.0	-1040.0
Run 3	694.0	**-3280.0**	762.0	**-14300.0**	398.0	**-3230.0**	920.0	**-6050.0**	1090.0	**-16400.0**	598.0	**-3980.0**
Run 4	-	-	-	-	-	-	-	-	-	-	-	-
Run 5	-	-	-	-	-	-	-	-	-	-	-	-
Run 6	-	-	-	-	-	-	-	-	-	-	-	-
Run 7	-	-	-	-	-	-	-	-	-	-	-	-
Run 8	-	-	-	-	-	-	-	-	-	-	-	-
Run 9	-	-	-	-	-	-	-	-	-	-	-	-
Run 10	-	-	-	-	-	-	-	-	-	-	-	-
Run 11	-	-	-	-	-	-	-	-	-	-	-	-
Run 12	-	-	-	-	-	-	-	-	-	-	-	-

Location	Column, 6" (152 mm) Above Cap Beam											
Gauge No.	SG 31		SG 32		SG 33		SG 34		SG 35		SG 36	
Bar Type	Longitudinal		Longitudinal		Longitudinal		Longitudinal		Longitudinal		Longitudinal	
Run No.	Max	Min	Max	Min	Max	Min	Max	Min	Max	Min	Max	Min
Run 1	165.0	-144.0	137.0	-179.0	-	-	186.0	-192.0	198.0	-212.0	131.0	-158.0
Run 2	323.0	-1230.0	357.0	-1490.0	-	-	467.0	-1170.0	513.0	-1330.0	330.0	-1100.0
Run 3	1180.0	-3370.0	1470.0	**-3460.0**	-	-	1140.0	**-6750.0**	1280.0	**-18300.0**	742.0	**-4560.0**
Run 4	-	-	1890.0	**-20100.0**	-	-	-	-	-	-	117.0	**-16300.0**
Run 5	-	-	-	-	-	-	-	-	-	-	-	-
Run 6	-	-	-	-	-	-	-	-	-	-	-	-
Run 7	-	-	-	-	-	-	-	-	-	-	-	-
Run 8	-	-	-	-	-	-	-	-	-	-	-	-
Run 9	-	-	-	-	-	-	-	-	-	-	-	-
Run 10	-	-	-	-	-	-	-	-	-	-	-	-
Run 11	-	-	-	-	-	-	-	-	-	-	-	-
Run 12	-	-	-	-	-	-	-	-	-	-	-	-

Table 3.10 Column longitudinal reinforcement strain data at 12 and 18 in above cap beam (values reported in microstrains)

Location	Column, 12" (305 mm) Above Cap Beam											
Gauge No.	SG 41		SG 42		SG 43		SG 44		SG 45		SG 46	
Bar Type	Longitudinal		Longitudinal		Longitudinal		Longitudinal		Longitudinal		Longitudinal	
Run No.	Max	Min	Max	Min	Max	Min	Max	Min	Max	Min	Max	Min
Run 1	137.0	-158.0	137.0	-165.0	41.2	-54.9	179.0	-158.0	-	-	-	-
Run 2	275.0	-894.0	309.0	-852.0	75.5	-110.0	406.0	-1090.0	-	-	-	-
Run 3	1070.0	-3200.0	1350.0	-3450.0	144.0	-1940.0	1050.0	-6520.0	-	-	-	-
Run 4	1400.0	-13300.0	-	-	426.0	-2490.0	-	-	-	-	-	-
Run 5	-3180.0	-16400.0	-	-	522.0	-2550.0	-	-	-	-	-	-
Run 6	-3910.0	-16900.0	-	-	611.0	-2520.0	-	-	-	-	-	-
Run 7	-4200.0	-17500.0	-	-	673.0	-2500.0	-	-	-	-	-	-
Run 8	-4610.0	-18900.0	-	-	728.0	-2570.0	-	-	-	-	-	-
Run 9	-5020.0	-24700.0	-	-	-	-	-	-	-	-	-	-
Run 10	-	-	-	-	-	-	-	-	-	-	-	-
Run 11	-	-	-	-	-	-	-	-	-	-	-	-
Run 12	-	-	-	-	-	-	-	-	-	-	-	-

Location	Column, 18" (457 mm) Above Cap Beam			
Gauge No.	SG 51		SG 52	
Bar Type	Longitudinal		Longitudinal	
Run No.	Max	Min	Max	Min
Run 1	48.1	-220.0	82.4	-172.0
Run 2	240.0	-1190.0	282.0	-1060.0
Run 3	962.0	**-3050.0**	872.0	**-3300.0**
Run 4	1180.0	**-10500.0**	1300.0	**-3760.0**
Run 5			1320.0	**-3960.0**
Run 6			1260.0	**-4250.0**
Run 7			1220.0	**-4640.0**
Run 8			1350.0	**-4990.0**
Run 9			1460.0	**-5640.0**
Run 10			1620.0	**-5670.0**
Run 11			1940.0	**-5390.0**
Run 12			2230.0	**-4170.0**

Table 3.11 Column transverse reinforcement strain data at 4.5 in and 9 in inside the cap beam (values reported in microstrains)

Location	Column, 9" (229 mm) Inside Cap Beam							
Gauge No.	SG 7		SG 8		SG 9		SG 10	
Bar Type	Transverse		Transverse		Transverse		Transverse	
Run No.	Max	Min	Max	Min	Max	Min	Max	Min
Run 1	34.3	-27.5	27.5	-27.5	55.0	-	27.5	-27.5
Run 2	48.1	-34.3	27.5	-41.2	61.9	-	20.6	-34.4
Run 3	89.3	-288.0	27.5	-666.0	254.0	-117.0	13.7	-151.0
Run 4	-54.9	-495.0	-75.6	-536.0	61.9	-316.0	6.9	-158.0
Run 5	-131.0	-584.0	-41.2	-1040.0	-	-399.0	6.9	-117.0
Run 6	-124.0	-611.0	110.0	-721.0	-27.5	-440.0	-6.9	-117.0
Run 7	-124.0	-639.0	96.2	-1310.0	-55.0	-461.0	-	-131.0
Run 8	-124.0	-653.0	-	-	-	-	-13.7	-144.0
Run 9	-124.0	-694.0	-	-	-	-	-20.6	-158.0
Run 10	-137.0	-694.0	-	-	-	-	-20.6	-172.0
Run 11	-206.0	-1030.0	-	-	-	-	-13.7	-158.0
Run 12	-398.0	-1150.0	-	-	-	-	-13.7	-165.0

Location	Column, 4.5" (114 mm) Inside Cap Beam							
Gauge No.	SG 17		SG 18		SG 19		SG 20	
Bar Type	Transverse		Transverse		Transverse		Transverse	
Run No.	Max	Min	Max	Min	Max	Min	Max	Min
Run 1	48.1	-13.7	34.4	-27.5	96.2	48.1	48.1	-6.9
Run 2	54.9	-13.7	41.3	-41.3	117.0	48.1	48.1	-20.6
Run 3	54.9	-227.0	20.6	-385.0	117.0	-89.3	41.2	-124.0
Run 4	-61.8	-749.0	-48.2	-454.0	96.2	-151.0	-34.3	-130.0
Run 5	-199.0	-831.0	-61.9	-495.0	61.8	-151.0	34.3	-144.0
Run 6	-110.0	-803.0	-110.0	-488.0	61.8	-137.0	110.0	-192.0
Run 7	-96.1	-762.0	-144.0	-488.0	68.7	-137.0	158.0	-179.0
Run 8	-96.1	-797.0	-158.0	-495.0	151.0	-34.4	96.1	-179.0
Run 9	-103.0	-920.0	-158.0	-502.0	179.0	13.7	-	-
Run 10	-158.0	-996.0	-	-	165.0	41.2	-	-
Run 11	-199.0	-1150.0	-	-	-	-	-	-
Run 12	-233.0	-1350.0	-	-	-	-	-	-

Table 3.12 Column transverse reinforcement strain data right at and 6” above the cap beam (values reported in microstrains)

Location	Column, At Cap Beam Face							
Gauge No.	SG 27		SG 28		SG 29		SG 30	
Bar Type	Transverse		Transverse		Transverse		Transverse	
Run No.	Max	Min	Max	Min	Max	Min	Max	Min
Run 1	20.6	-34.3	-34.4	-82.5	34.4	-13.7	27.5	-41.2
Run 2	13.7	-89.3	-48.1	-110.0	34.4	-82.5	6.9	-192.0
Run 3	-48.1	-172.0	-82.5	-186.0	13.7	-151.0	0.0	-247.0
Run 4	-27.5	-234.0	-103.0	-247.0	-27.5	-213.0	-54.9	-645.0
Run 5	-20.6	-213.0	-137.0	-289.0	-55.0	-296.0	-151.0	-790.0
Run 6	-48.1	-206.0	-172.0	-350.0	-151.0	-351.0	-151.0	-831.0
Run 7	-61.8	-179.0	-186.0	-412.0	-213.0	-426.0	-144.0	-776.0
Run 8	-48.1	-185.0	-557.0	-845.0	-247.0	-474.0	-144.0	-893.0
Run 9	-41.2	-179.0	-564.0	-928.0	-254.0	-598.0	-137.0	-1260.0
Run 10	-27.5	-179.0	-488.0	-983.0	-261.0	-735.0	-151.0	-1860.0
Run 11	75.6	-151.0	-	-	-	-	-	-
Run 12	261.0	-124.0	-	-	-	-	-	-

Location	Column, 6" (152 mm) Above Cap Beam							
Gauge No.	SG 37		SG 38		SG 39		SG 40	
Bar Type	Transverse		Transverse		Transverse		Transverse	
Run No.	Max	Min	Max	Min	Max	Min	Max	Min
Run 1	27.5	-20.6	34.4	-20.6	27.5	-20.6	20.6	-34.4
Run 2	20.6	-131.0	20.6	-131.0	27.5	-110.0	27.5	-158.0
Run 3	-61.8	-213.0	-6.9	-220.0	-20.6	-227.0	-34.4	-282.0
Run 4	-110.0	-316.0	-27.5	-289.0	-20.6	-371.0	-103.0	-378.0
Run 5	-186.0	-419.0	-82.4	-378.0	-27.5	-385.0	-240.0	-522.0
Run 6	-199.0	-543.0	-61.8	-275.0	-68.7	-399.0	-330.0	-591.0
Run 7	-227.0	-653.0	-34.4	-412.0	-75.6	-378.0	-371.0	-625.0
Run 8	-240.0	-715.0	41.2	-660.0	-41.2	-330.0	-350.0	-660.0
Run 9	-254.0	-811.0	34.4	-660.0	-34.4	-337.0	-330.0	-838.0
Run 10	-247.0	-845.0	192.0	-460.0	-82.5	-419.0	-350.0	-1040.0
Run 11	-289.0	-955.0	-	-	-117.0	-522.0	-405.0	-1360.0
Run 12	-309.0	-804.0	-	-	-206.0	-763.0	-508.0	-1520.0

Table 3.13 Column transverse reinforcement strain data at 12 in above cap beam (values reported in microstrains)

Location	Column, 12" (305 mm) Above Cap Beam							
Gauge No.	SG 47		SG 48		SG 49		SG 50	
Bar Type	Transverse		Transverse		Transverse		Transverse	
Run No.	Max	Min	Max	Min	Max	Min	Max	Min
Run 1	13.7	-27.5	20.6	-34.3	54.9	6.9	27.5	-27.5
Run 2	13.7	-61.8	20.6	-68.7	61.8	-48.0	27.5	-48.1
Run 3	-13.7	-103.0	13.7	-440.0	34.3	-233.0	55.0	-151.0
Run 4	-41.2	-179.0	-137.0	-577.0	-82.4	-494.0	131.0	-172.0
Run 5	-82.4	-165.0	-137.0	-543.0	-227.0	-542.0	117.0	-165.0
Run 6	-82.4	-199.0	-137.0	-556.0	-288.0	-618.0	75.6	-172.0
Run 7	-75.6	-227.0	-131.0	-570.0	-329.0	-748.0	96.2	-165.0
Run 8	-61.8	-234.0	-110.0	-570.0	-329.0	-783.0	137.0	-131.0
Run 9	-68.7	-275.0	-89.3	-453.0	-309.0	-810.0	165.0	-137.0
Run 10	-68.7	-302.0	34.3	-343.0	-329.0	-803.0	137.0	-165.0
Run 11	-34.3	-289.0	20.6	-412.0	-	-	82.5	-206.0
Run 12	-48.1	-309.0	-61.8	-488.0	-	-	-20.6	-261.0

Table 3.14 Cap beam transverse reinforcement strain data set #1 (values reported in microstrains)

Location	Cap Beam															
Gauge No.	SG 61		SG 62		SG 63		SG 64		SG 65		SG 66		SG 67		SG 68	
Bar Type	Transverse		Transverse		Transverse		Transverse		Transverse		Transverse		Transverse		Transverse	
Run No.	Max	Min	Max	Min	Max	Min	Max	Min	Max	Min	Max	Min	Max	Min	Max	Min
Run 1	61.8	-13.7	27.5	-20.6	41.1	-6.8	6.9	-41.2	55.0	-6.9	-6.9	-55.0	20.6	-27.5	-	-
Run 2	117.0	-27.5	41.2	-27.5	54.7	-13.7	20.6	-41.2	61.8	-6.9	13.7	-61.8	34.4	-27.5	-	-
Run 3	206.0	-75.6	61.9	-41.2	287.0	-13.7	48.1	-61.8	289.0	-6.9	55.0	-68.7	144.0	-27.5	-	-
Run 4	247.0	-96.2	55.0	-48.1	335.0	0.0	55.0	-82.5	343.0	0.0	68.7	-75.6	151.0	-34.4	-	-
Run 5	254.0	-96.2	48.1	-61.9	328.0	0.0	48.1	-89.3	323.0	0.0	55.0	-82.5	131.0	-27.5	-	-
Run 6	254.0	-103.0	41.2	-68.7	335.0	-6.8	20.6	-103.0	316.0	13.7	27.5	-89.3	103.0	-34.4	-	-
Run 7	247.0	-117.0	34.4	-82.5	322.0	-13.7	13.7	-117.0	309.0	6.9	27.5	-96.2	82.4	-41.2	-	-
Run 8	323.0	-48.1	48.1	-68.7	301.0	-34.2	27.5	-117.0	282.0	6.9	13.7	-117.0	89.3	-34.4	-	-
Run 9	350.0	-68.7	34.4	-75.6	287.0	-20.5	41.2	-117.0	275.0	6.9	34.4	-124.0	96.2	-41.2	-	-
Run 10	343.0	-124.0	27.5	-75.6	246.0	0.0	61.8	-124.0	206.0	-6.9	55.0	-124.0	96.2	-68.7	-	-
Run 11	357.0	-165.0	27.5	-82.5	171.0	6.8	96.2	-117.0	165.0	-34.3	103.0	-117.0	82.4	-117.0	-	-
Run 12	357.0	-192.0	34.4	-82.5	226.0	-13.7	96.2	-89.3	192.0	-68.7	137.0	-96.2	96.2	-158.0	-	-

Location	Cap Beam															
Gauge No.	SG 69		SG 70		SG 71		SG 72		SG 73		SG 74		SG 75		SG 76	
Bar Type	Transverse		Transverse		Transverse		Transverse		Transverse		Transverse		Transverse		Transverse	
Run No.	Max	Min	Max	Min	Max	Min	Max	Min	Max	Min	Max	Min	Max	Min	Max	Min
Run 1	27.5	-27.5	27.5	-13.7	41.1	-13.7	27.5	-20.6	27.5	-20.6	54.9	-6.9	-	-	61.9	-27.5
Run 2	41.2	-27.5	34.3	-13.7	61.6	-13.7	41.2	-27.5	27.5	-27.5	54.9	-41.2	-	-	103.0	-68.7
Run 3	96.2	-55.0	48.1	-27.5	68.4	-20.5	61.9	-41.2	82.4	-110.0	41.2	-611.0	-	-	234.0	-220.0
Run 4	110.0	-110.0	41.2	-34.3	68.4	-27.4	68.7	-55.0	124.0	-117.0	41.2	-852.0	-	-	247.0	-385.0
Run 5	110.0	-165.0	34.3	-48.1	68.4	-27.4	68.7	-55.0	89.3	-110.0	41.2	-955.0	-	-	247.0	-412.0
Run 6	110.0	-206.0	27.5	-34.3	68.4	-20.5	61.9	-48.1	6.9	-172.0	34.3	-1010.0	-	-	247.0	-392.0
Run 7	110.0	-234.0	20.6	-41.2	68.4	-27.4	68.7	-48.1	-48.1	-220.0	34.3	-1060.0	-	-	247.0	-399.0
Run 8	110.0	-261.0	20.6	-41.2	68.4	-20.5	82.5	-48.1	-117.0	-282.0	6.9	-1080.0	-	-	241.0	-419.0
Run 9	117.0	-275.0	27.5	-41.2	68.4	-27.4	75.6	-55.0	-165.0	-344.0	27.5	-1060.0	-	-	241.0	-474.0
Run 10	124.0	-268.0	13.7	-61.8	68.4	-6.8	75.6	-55.0	-199.0	-385.0	34.3	-962.0	-	-	227.0	-529.0
Run 11	124.0	-261.0	20.6	-75.6	75.3	6.8	75.6	-68.7	-227.0	-405.0	27.5	-989.0	-	-	206.0	-646.0
Run 12	131.0	-234.0	13.7	-110.0	75.3	0.0	75.6	-117.0	-254.0	-426.0	34.3	-1090.0	-	-	192.0	-694.0

Table 3.15 Cap beam transverse reinforcement strain data set #2 (values reported in microstrains)

Location	Cap Beam															
Gauge No.	SG 77		SG 78		SG 79		SG 80		SG 81		SG 82		SG 83		SG 84	
Bar Type	Transverse		Transverse		Transverse		Transverse		Transverse		Transverse		Transverse		Transverse	
Run No.	Max	Min	Max	Min	Max	Min	Max	Min	Max	Min	Max	Min	Max	Min	Max	Min
Run 1	27.5	-20.6	34.4	-20.6	-	-	-	-	41.2	-27.5	20.6	-27.5	34.4	-27.5	41.2	-20.6
Run 2	55.0	-13.7	55.0	-27.5	-	-	-	-	68.7	-27.5	27.5	-34.3	41.2	-20.6	55.0	-20.6
Run 3	144.0	-48.1	213.0	-61.8	-	-	-	-	172.0	-54.9	117.0	-48.1	55.0	-27.5	110.0	-41.2
Run 4	179.0	-82.5	316.0	-61.8	-	-	-	-	206.0	-110.0	137.0	-54.9	55.0	-27.5	117.0	-82.5
Run 5	192.0	-82.5	234.0	-82.4	-	-	-	-	206.0	-144.0	137.0	-68.7	48.1	-34.4	103.0	-89.3
Run 6	192.0	-75.6	247.0	-96.2	-	-	-	-	199.0	-185.0	137.0	-75.5	55.0	-34.4	103.0	-82.5
Run 7	199.0	-55.0	261.0	-82.4	-	-	-	-	192.0	-220.0	130.0	-82.4	55.0	-34.4	96.2	-82.5
Run 8	186.0	-96.2	295.0	-68.7	-	-	-	-	192.0	-254.0	130.0	-89.3	68.7	-34.4	103.0	-75.6
Run 9	192.0	-96.2	316.0	-68.7	-	-	-	-	199.0	-282.0	137.0	-103.0	68.7	-34.4	96.2	-96.2
Run 10	186.0	-137.0	323.0	-41.2	-	-	-	-	206.0	-302.0	124.0	-117.0	68.7	-34.4	89.3	-103.0
Run 11	179.0	-	350.0	-55.0	-	-	-	-	199.0	-343.0	117.0	-117.0	75.6	-41.2	82.5	-151.0
Run 12	275.0	-	460.0	0.0	-	-	-	-	179.0	-343.0	96.1	-158.0	61.9	-48.1	96.2	-199.0

Location	Cap Beam															
Gauge No.	SG 85		SG 86		SG 87		SG 88		SG 89		SG 90		SG 91		SG 92	
Bar Type	Transverse		Transverse		Transverse		Transverse		Transverse		Transverse		Transverse		Transverse	
Run No.	Max	Min	Max	Min	Max	Min	Max	Min	Max	Min	Max	Min	Max	Min	Max	Min
Run 1	41.2	-13.7	20.6	-34.3	27.5	-13.8	27.5	-34.3	20.6	-27.5	-	-	27.5	-27.5	41.2	0.0
Run 2	34.4	-20.6	20.6	-89.3	34.4	-20.6	41.2	-55.0	34.4	-34.4	-	-	27.5	-68.7	48.1	-41.2
Run 3	34.4	-186.0	6.9	-440.0	89.4	-55.0	137.0	-185.0	61.9	-75.6	-	-	20.6	-447.0	261.0	-982.0
Run 4	13.7	-289.0	6.9	-680.0	124.0	-117.0	165.0	-275.0	75.6	-96.2	-	-	27.5	-694.0	350.0	-1290.0
Run 5	6.9	-309.0	-13.7	-735.0	117.0	-138.0	158.0	-289.0	75.6	-103.0	-	-	27.5	-749.0	289.0	-1450.0
Run 6	13.7	-309.0	-20.6	-735.0	110.0	-172.0	165.0	-275.0	75.6	-110.0	-	-	13.7	-749.0	234.0	-1570.0
Run 7	13.7	-309.0	-27.5	-749.0	110.0	-199.0	179.0	-268.0	75.6	-117.0	-	-	20.6	-735.0	240.0	-1640.0
Run 8	20.6	-302.0	-27.5	-756.0	110.0	-213.0	199.0	-261.0	82.5	-110.0	-	-	27.5	-770.0	220.0	-1760.0
Run 9	20.6	-337.0	-41.2	-817.0	110.0	-227.0	227.0	-254.0	89.4	-110.0	-	-	27.5	-804.0	110.0	-1930.0
Run 10	20.6	-371.0	-68.7	-893.0	124.0	-227.0	199.0	-316.0	82.5	-89.4	-	-	34.4	-838.0	6.9	-2010.0
Run 11	-6.9	-715.0	-110.0	-996.0	117.0	-234.0	165.0	-392.0	89.4	-68.7	-	-	13.7	-928.0	206.0	-1980.0
Run 12	-75.6	-701.0	-165.0	-1060.0	117.0	-220.0	124.0	-426.0	96.2	-55.0	-	-	-13.7	-1020.0	199.0	-1550.0

Table 3.16 Cap beam transverse reinforcement strain data set #3 (values reported in microstrains)

Location	Cap Beam															
Gauge No.	SG 93		SG 94		SG 95		SG 96		SG 97		SG 98		SG 99		SG 100	
Bar Type	Transverse		Transverse		Transverse		Transverse		Transverse		Transverse		Transverse		Transverse	
Run No.	Max	Min	Max	Min	Max	Min	Max	Min	Max	Min	Max	Min	Max	Min	Max	Min
Run 1	55.0	-6.9	20.6	-41.2	-6.9	-61.8	27.5	-27.5	-	-	41.3	-48.1	27.5	-20.6	41.2	-13.7
Run 2	82.5	-27.5	34.4	-48.1	-6.9	-61.8	34.4	-27.5	-	-	68.8	-124.0	27.5	-20.6	54.9	-20.6
Run 3	186.0	-151.0	117.0	-96.2	13.7	-61.8	61.8	-103.0	-	-	151.0	-619.0	55.0	-20.6	96.1	-96.1
Run 4	247.0	-199.0	137.0	-117.0	20.6	-61.8	61.8	-158.0	-	-	144.0	-990.0	55.0	-27.5	110.0	-124.0
Run 5	254.0	-192.0	137.0	-117.0	20.6	-68.7	68.7	-172.0	-	-	131.0	-1040.0	41.2	-27.5	103.0	-130.0
Run 6	247.0	-199.0	144.0	-103.0	6.9	-68.7	96.2	-151.0	-	-	124.0	-1010.0	41.2	-34.4	110.0	-130.0
Run 7	247.0	-206.0	137.0	-110.0	0.0	-75.6	96.2	-151.0	-	-	131.0	-984.0	34.4	-34.4	103.0	-151.0
Run 8	254.0	-199.0	151.0	-103.0	41.2	-41.2	124.0	-172.0	-	-	117.0	-1000.0	41.2	-27.5	110.0	-137.0
Run 9	261.0	-206.0	151.0	-117.0	48.1	-41.2	55.0	-213.0	-	-	103.0	-1100.0	34.4	-27.5	117.0	-137.0
Run 10	268.0	-179.0	137.0	-117.0	34.3	-48.1	55.0	-240.0	-	-	110.0	-1200.0	27.5	-34.4	117.0	-124.0
Run 11	282.0	-144.0	124.0	-137.0	34.3	-48.1	68.7	-282.0			117.0	-1400.0	20.6	-34.4	117.0	-103.0
Run 12	275.0	-110.0	103.0	-137.0	20.6	-55.0	48.1	-405.0	-	-	34.4	-1560.0	13.7	-34.4	137.0	-96.2

Table 3.17 Cap beam longitudinal reinforcement strain data (values reported in microstrains)

Location	Cap Beam							
Gauge No.	SG 101		SG 102		SG 103		SG 104	
Bar Type	Longitudinal		Longitudinal		Longitudinal		Longitudinal	
Run No.	Max	Min	Max	Min	Max	Min	Max	Min
Run 1	27.5	-20.6	34.4	-20.6	-	-	20.6	-27.5
Run 2	27.5	-34.4	34.4	-27.5	-	-	13.7	-48.1
Run 3	34.4	-206.0	34.4	-110.0	-	-	13.7	-309.0
Run 4	13.7	-261.0	41.2	-158.0	-	-	-	-
Run 5	20.6	-261.0	41.2	-179.0	-	-	-	-
Run 6	13.7	-261.0	34.4	-172.0	-	-	-	-
Run 7	13.7	-275.0	41.2	-165.0	-	-	-	-
Run 8	41.2	-227.0	41.2	-172.0	-	-	-	-
Run 9	41.2	-213.0	34.4	-192.0	-	-	-	-
Run 10	41.2	-172.0	34.4	-206.0	-	-	-	-
Run 11	34.4	-137.0	27.5	-234.0	-	-	-	-
Run 12	41.2	-96.2	27.5	-234.0	-	-	-	-

CHAPTER 2 FIGURES

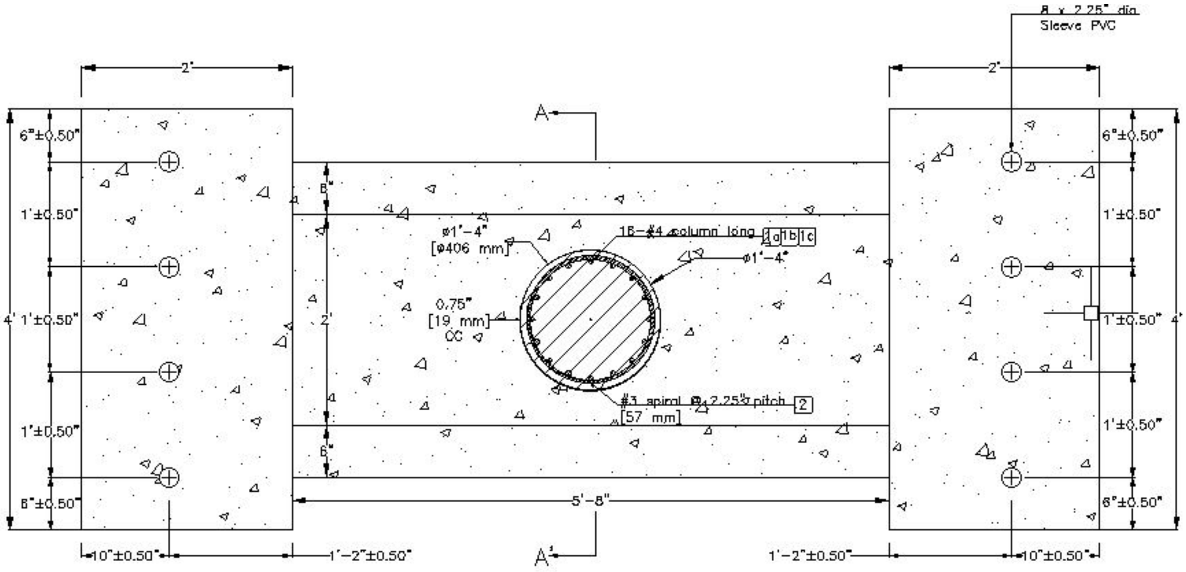

Figure 2.1 Plan view of the horizontal cut section

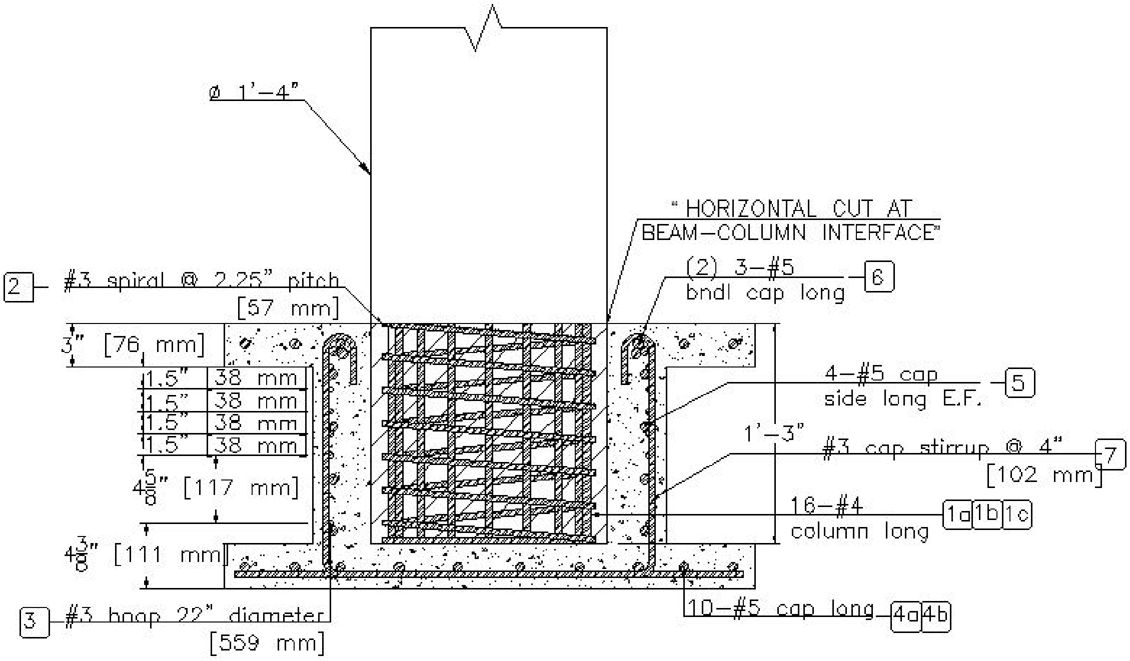

Figure 2.2 Horizontal cut at the beam-column interface

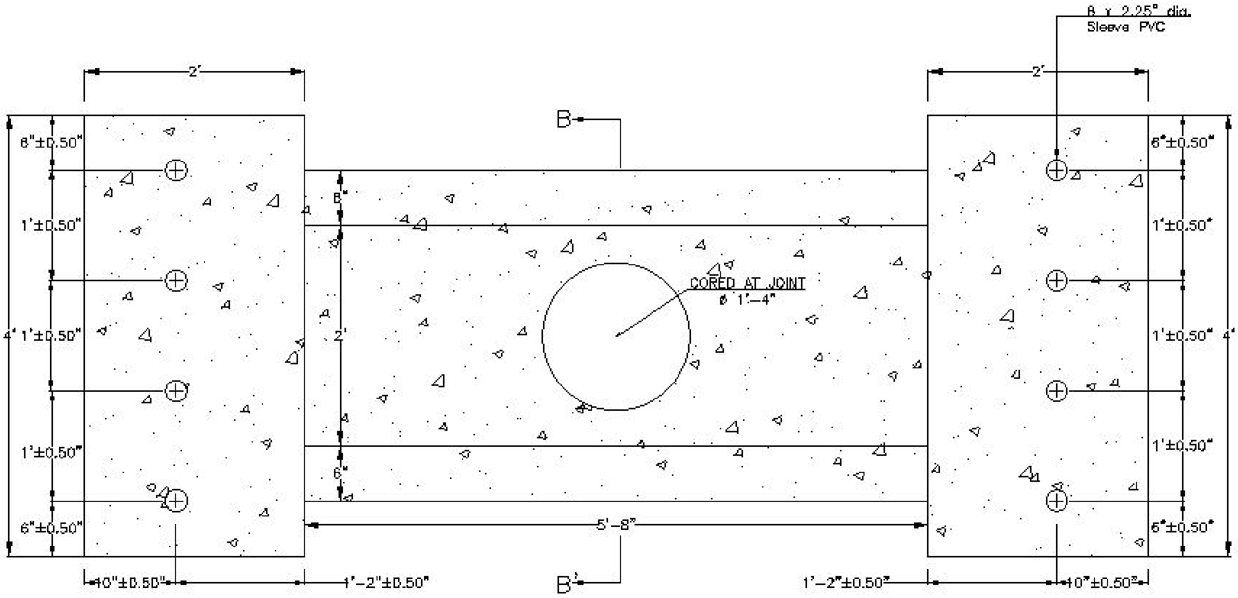

Figure 2.3 Plan view of the cored joint specimen

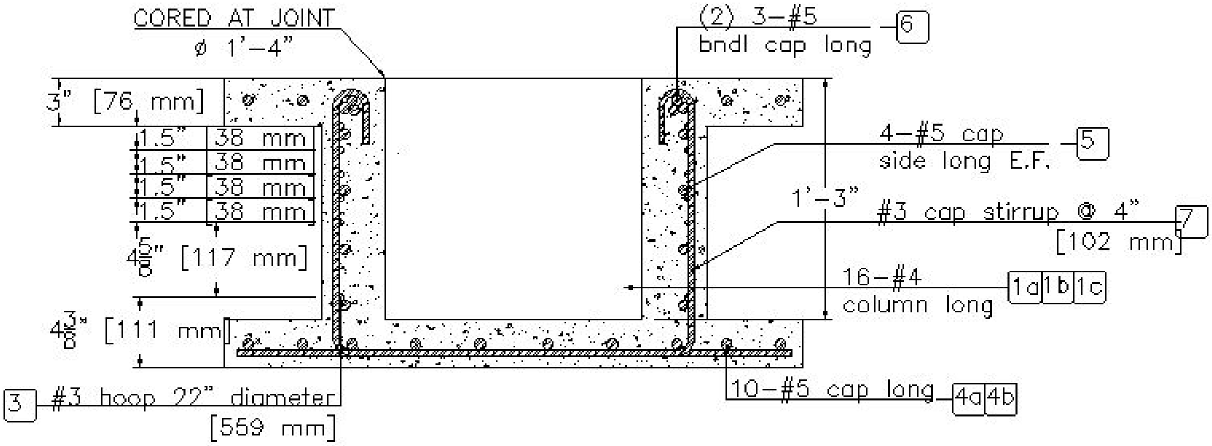

Figure 2.4 Coring of embedded column specimen

Figure 2.5 Cap beam specimen after cutting

Figure 2.6 Coring process and extraction of older joint

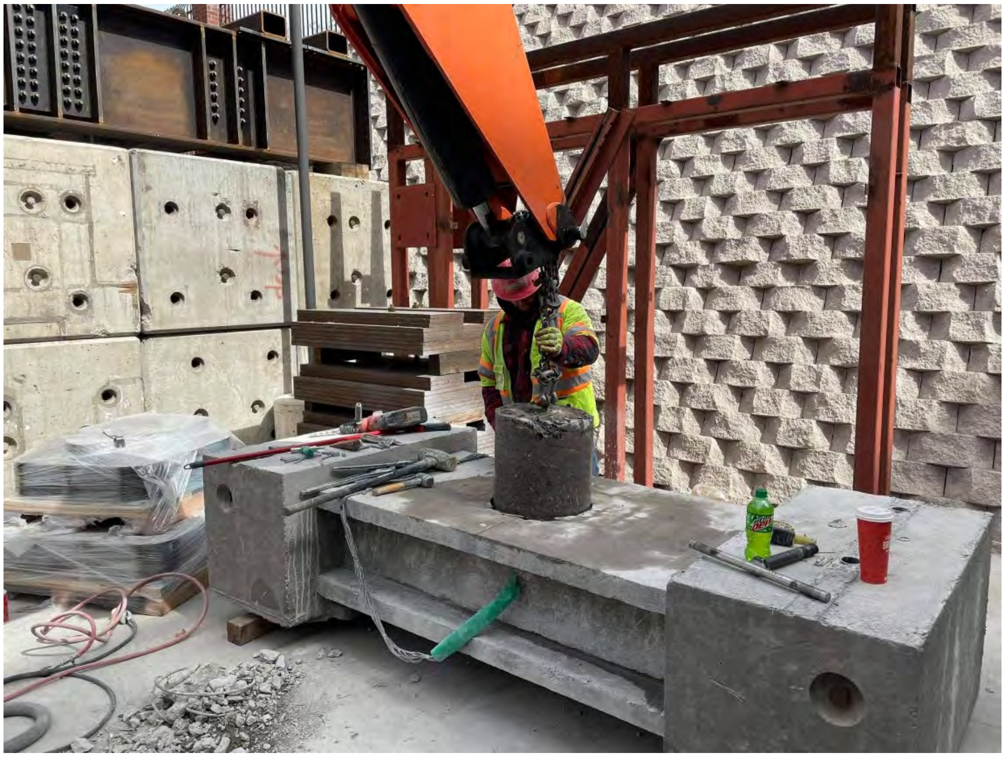

Figure 2.7 Another view of the coring process

Figure 2.8 Close-up view of the extracted portion of the column (embedded in joint)

Figure 2.9 Joint pocket after coring

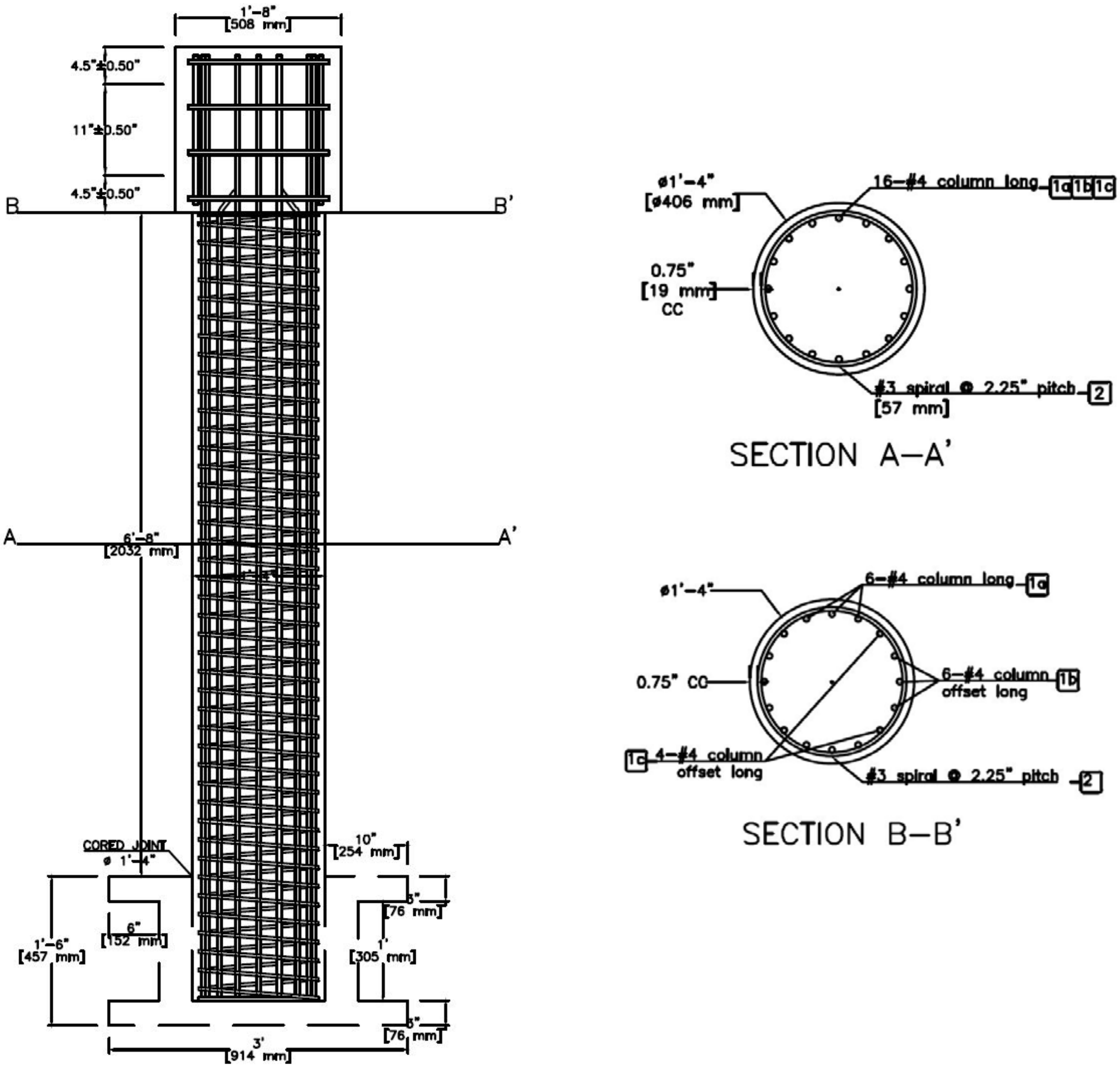

Figure 2.10 Column reinforcement details

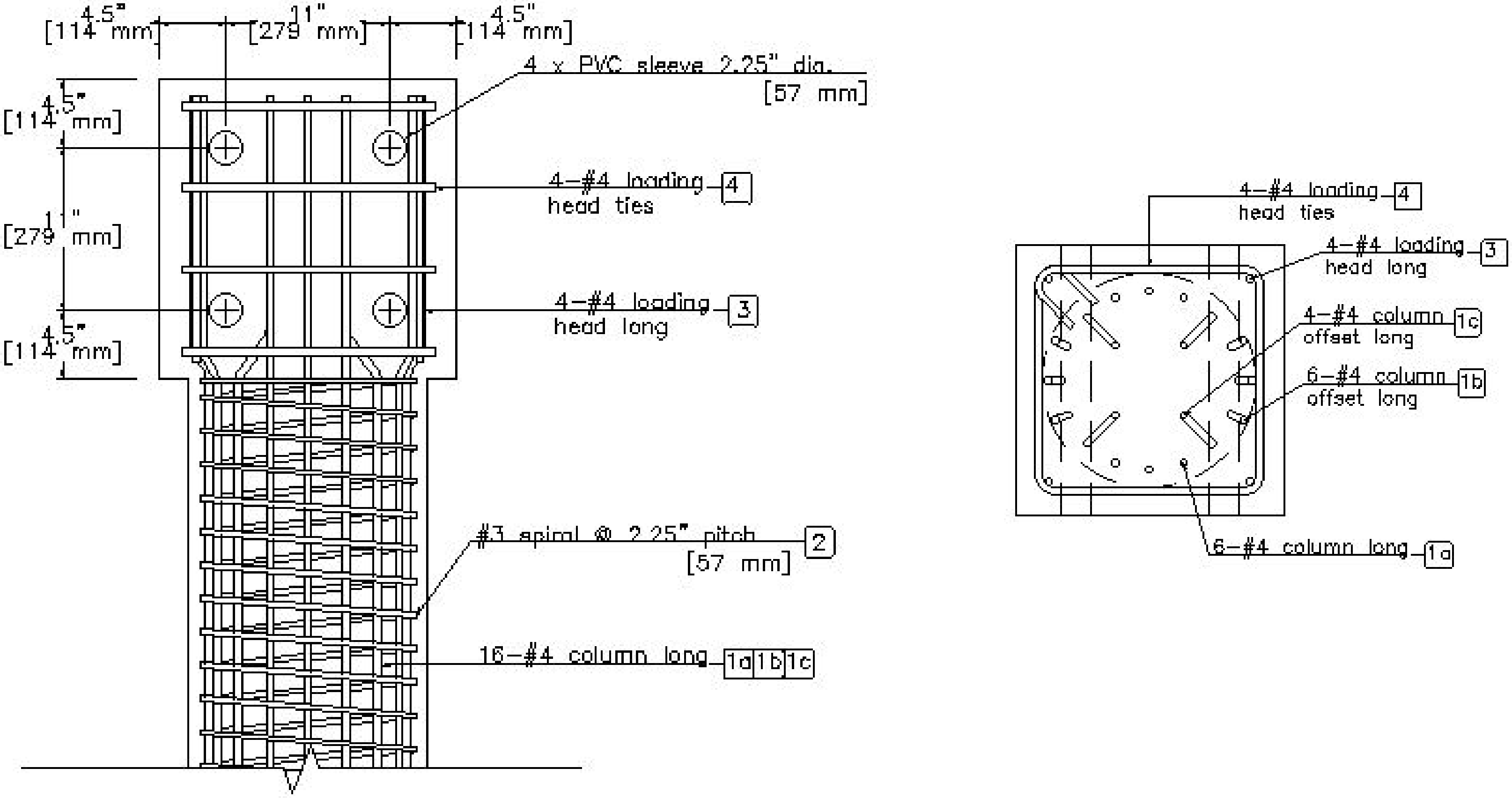

Figure 2.11 Loading head reinforcement details

Figure 2.12 Assembled column reinforcement cage and loading head reinforcement

Figure 2.13 Lifting of column reinforcement cage to be placed inside formwork

Figure 2.14 Casting of concrete from the top of the column

Figure 2.15 Vibrating of fresh cast concrete

Figure 2.16 Overall specimen after stripping of new column formwork

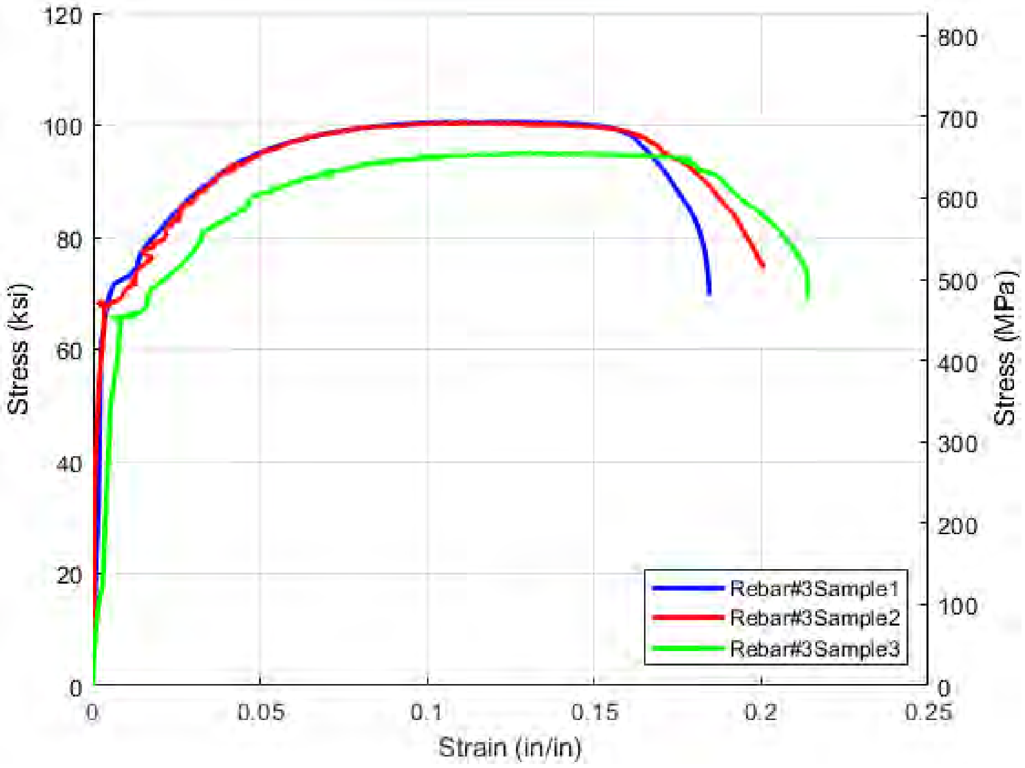

Figure 2.17 Measured stress-strain relationships for #3 bars

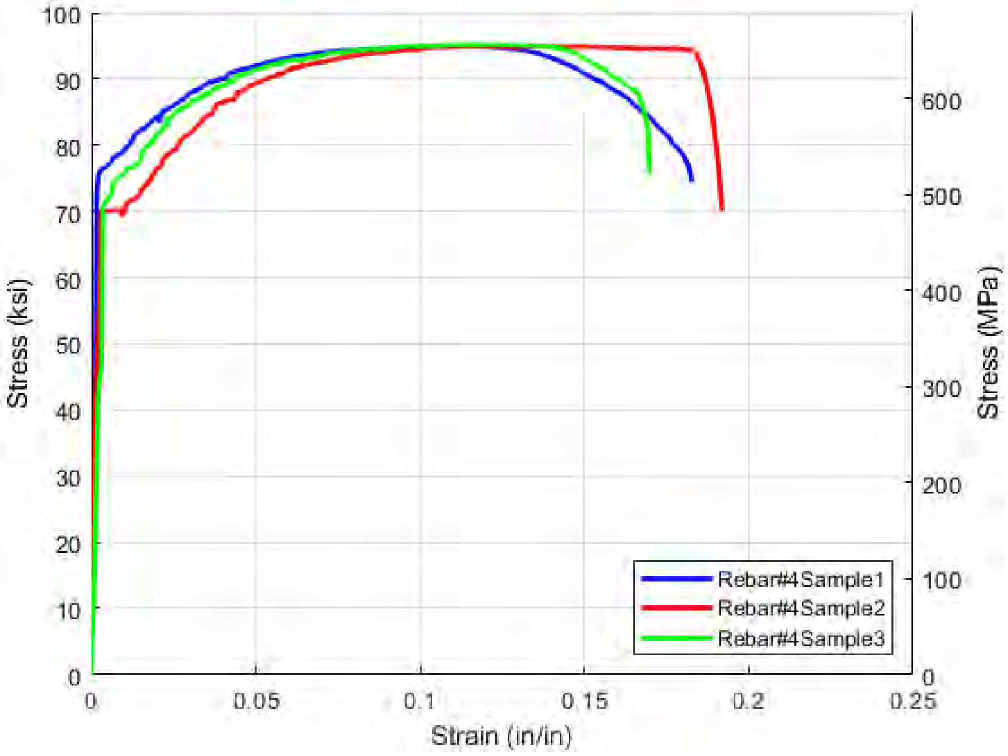

Figure 2.18 Measured stress-strain relationships for #4 bars

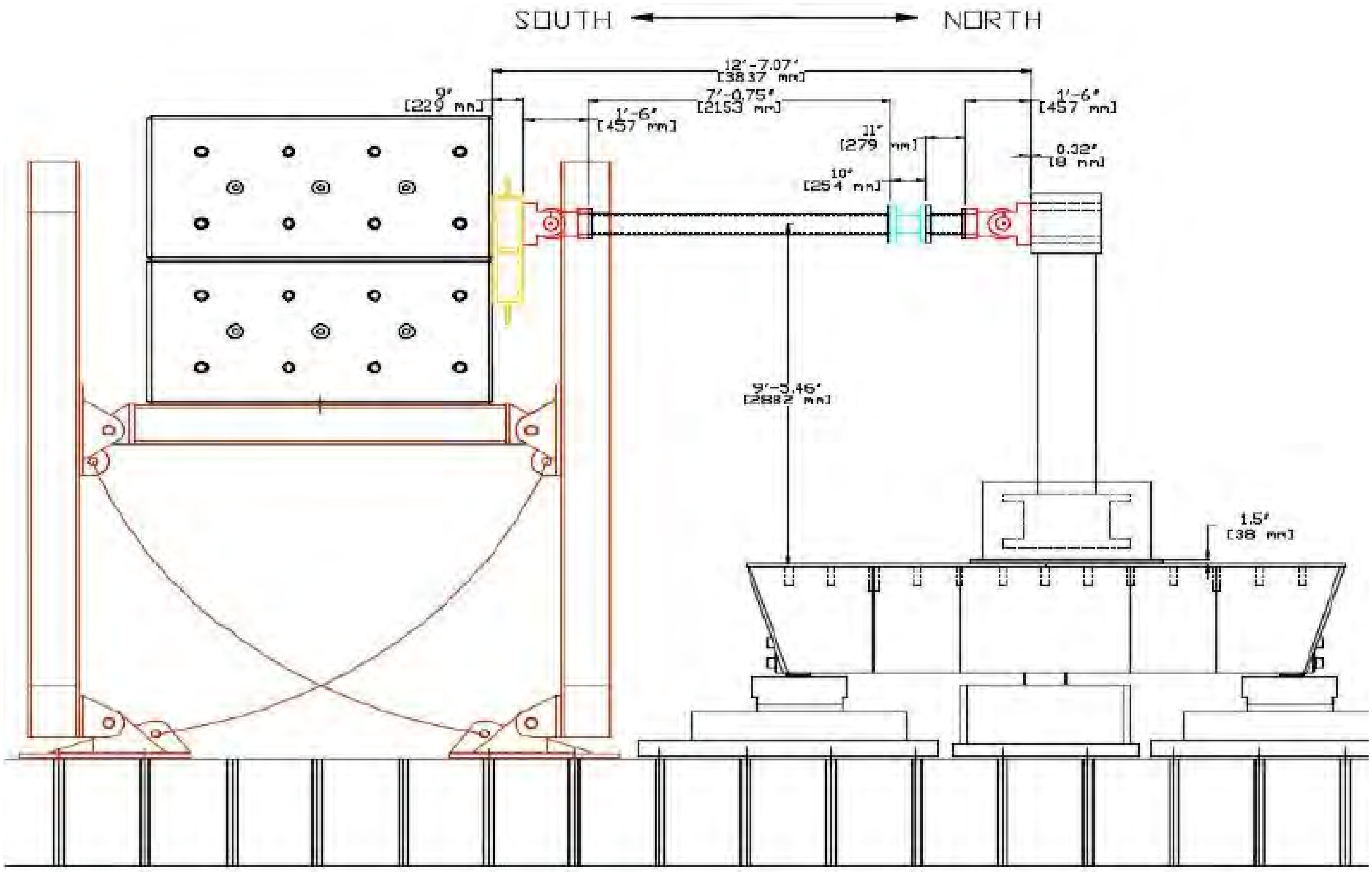

Figure 2.19 Elevation view of the specimen on the shake table

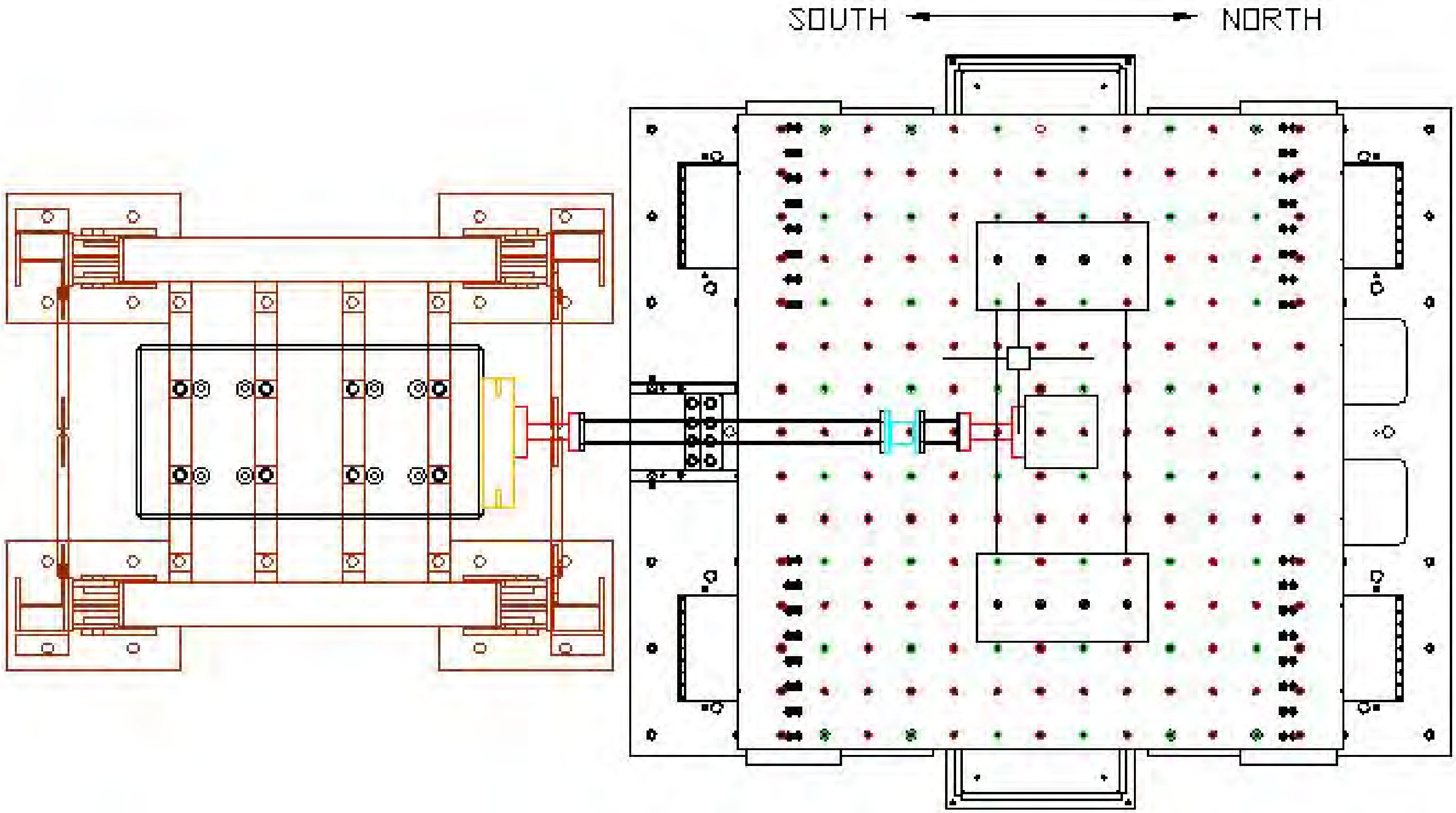

Figure 2.20 Plan view of the specimen on the shake table

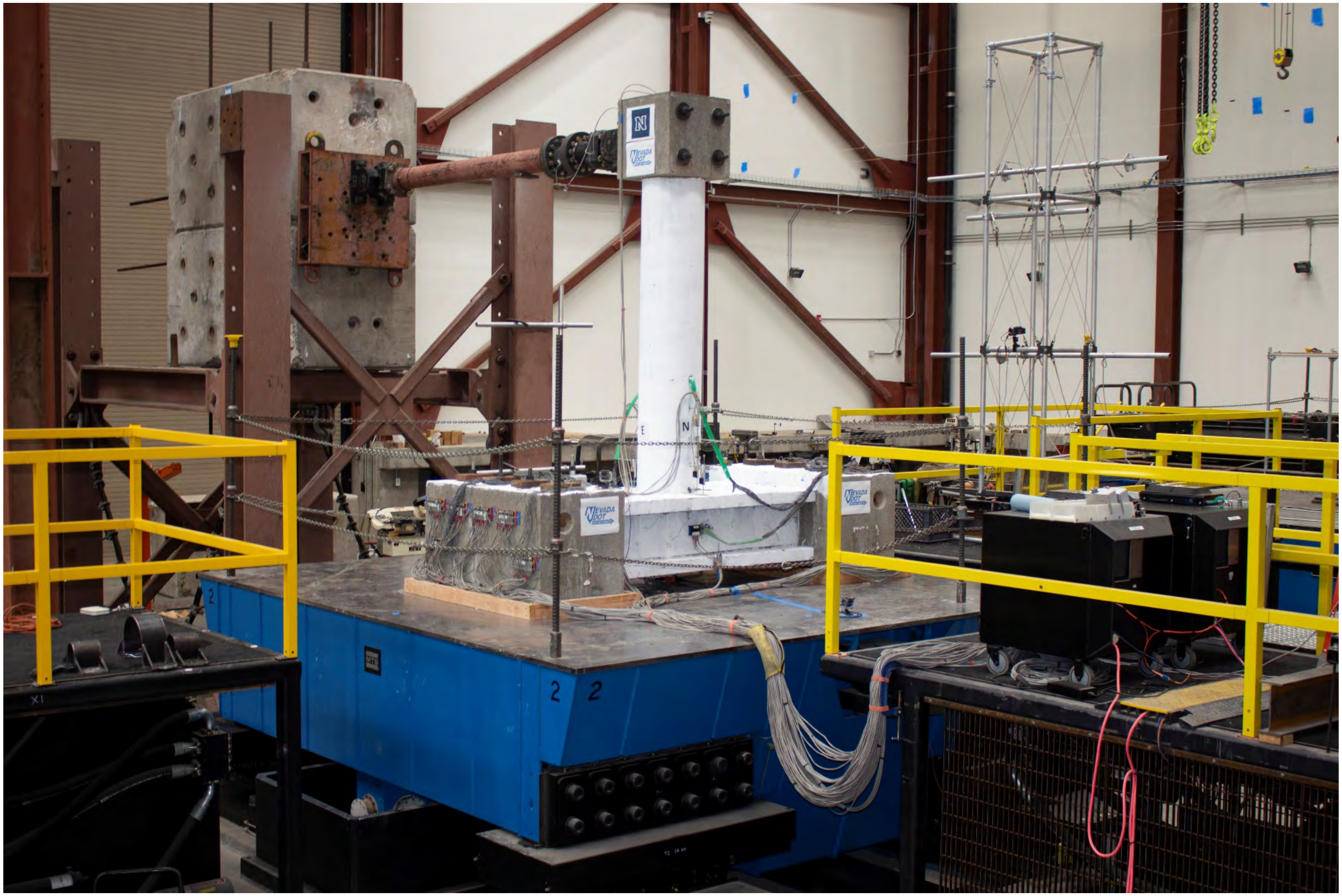

Figure 2.21 Overall view of shake table test setup of the repaired specimen

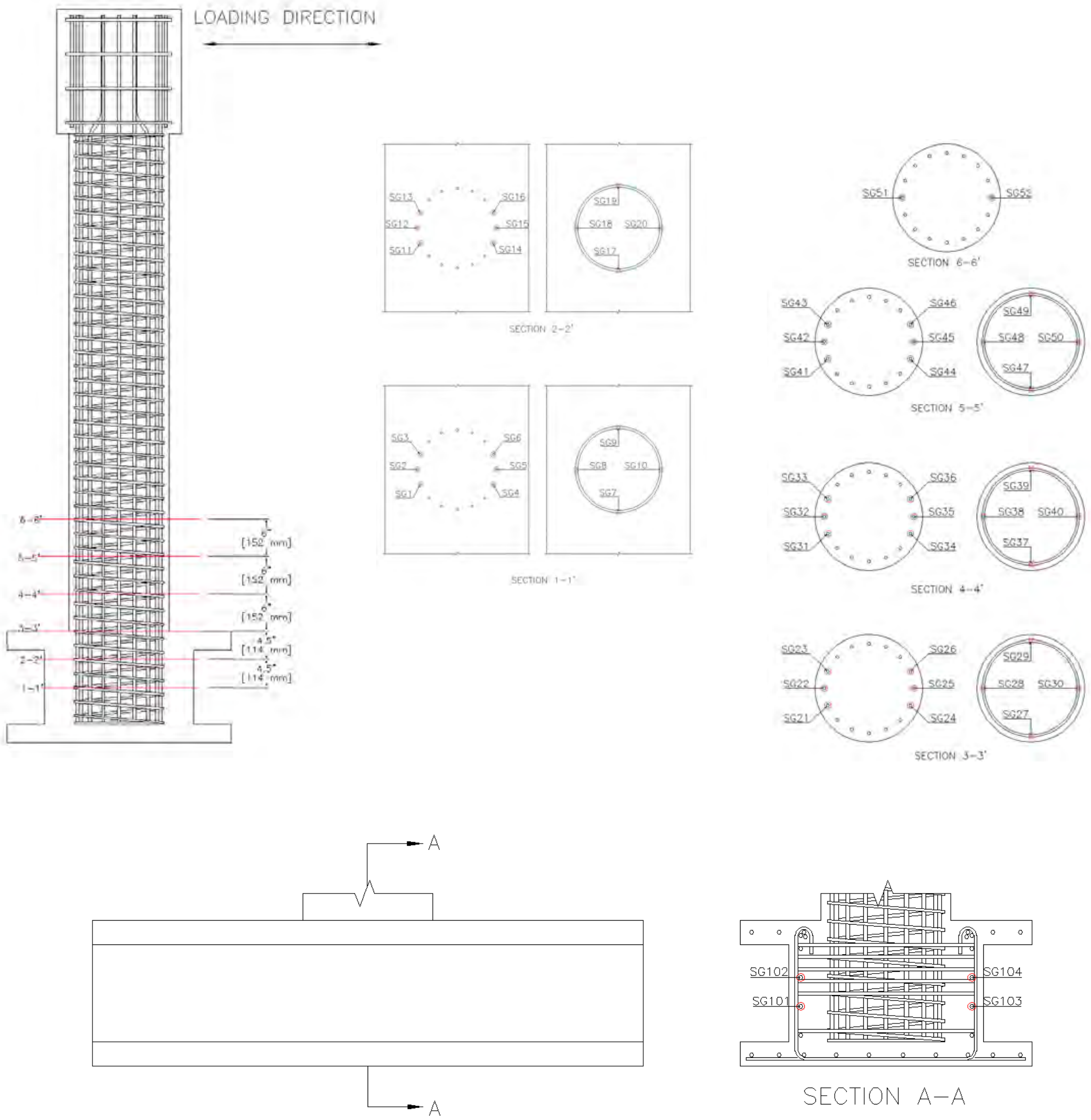

Figure 2.22 Strain gauges on longitudinal bars, spirals, and longitudinal cap beam

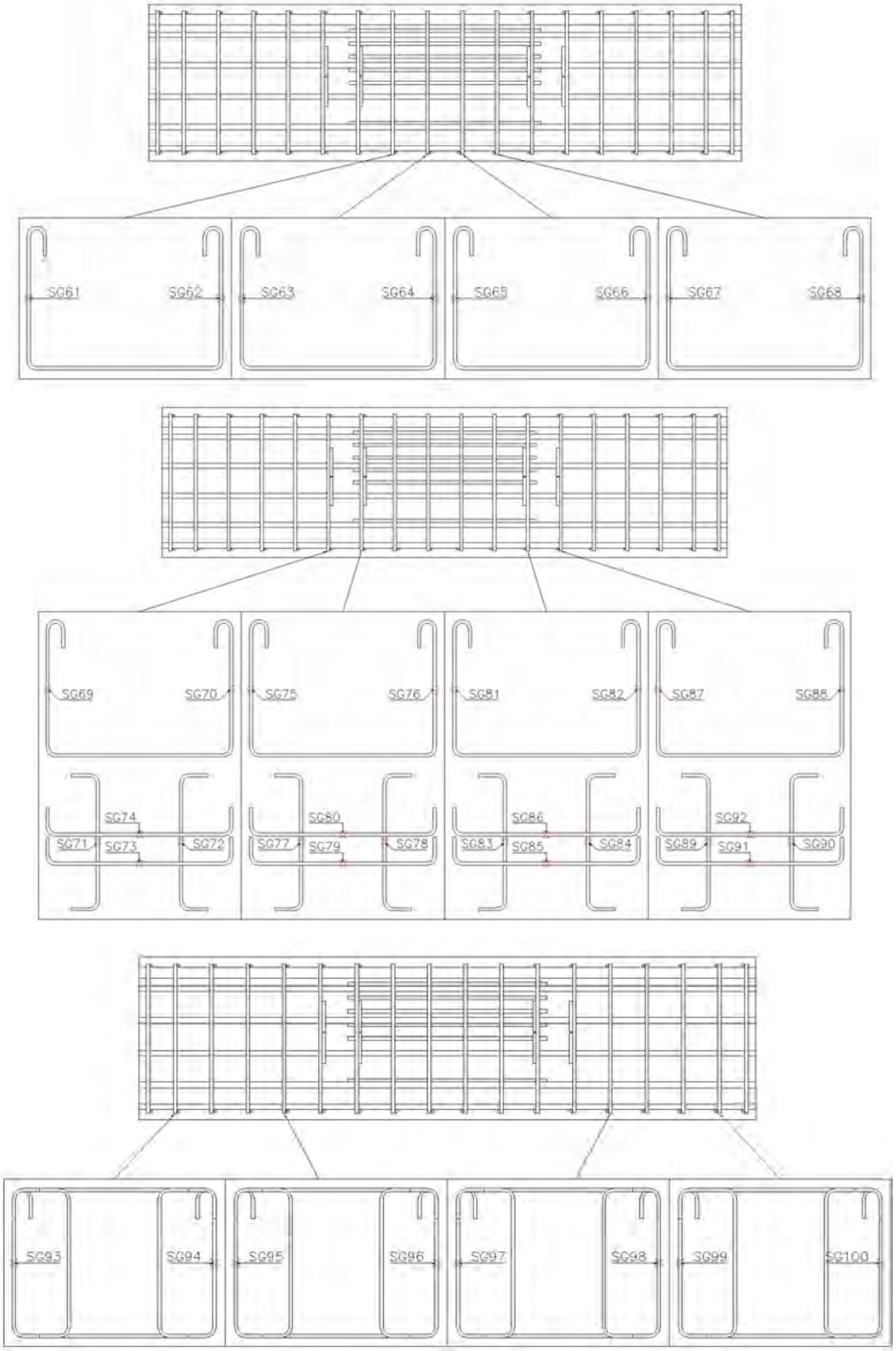

Figure 2.23 Strain gauges on stirrups and ties in the cap beam

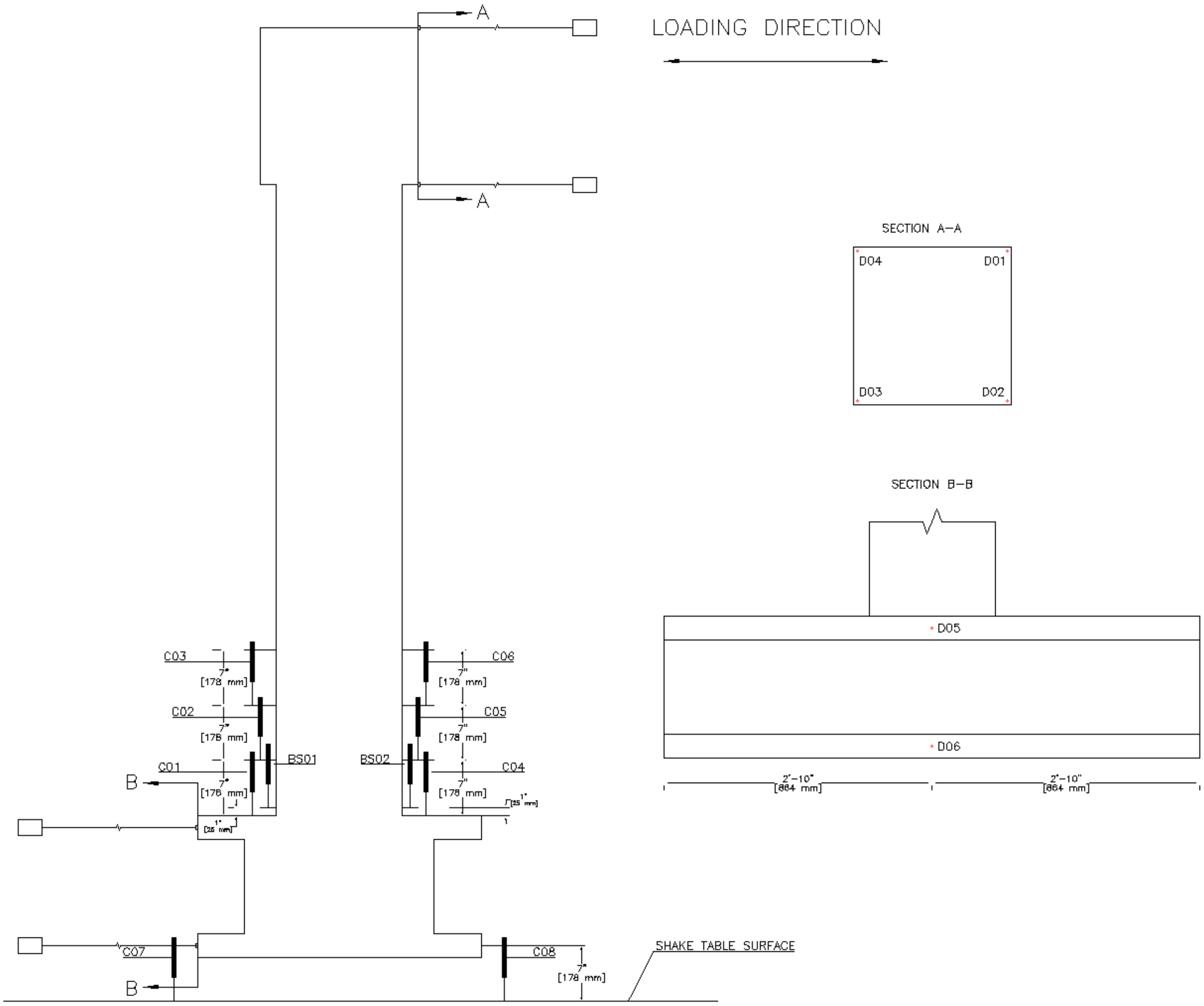

Figure 2.24 Wire potentiometers and displacement transducers for curvature estimation

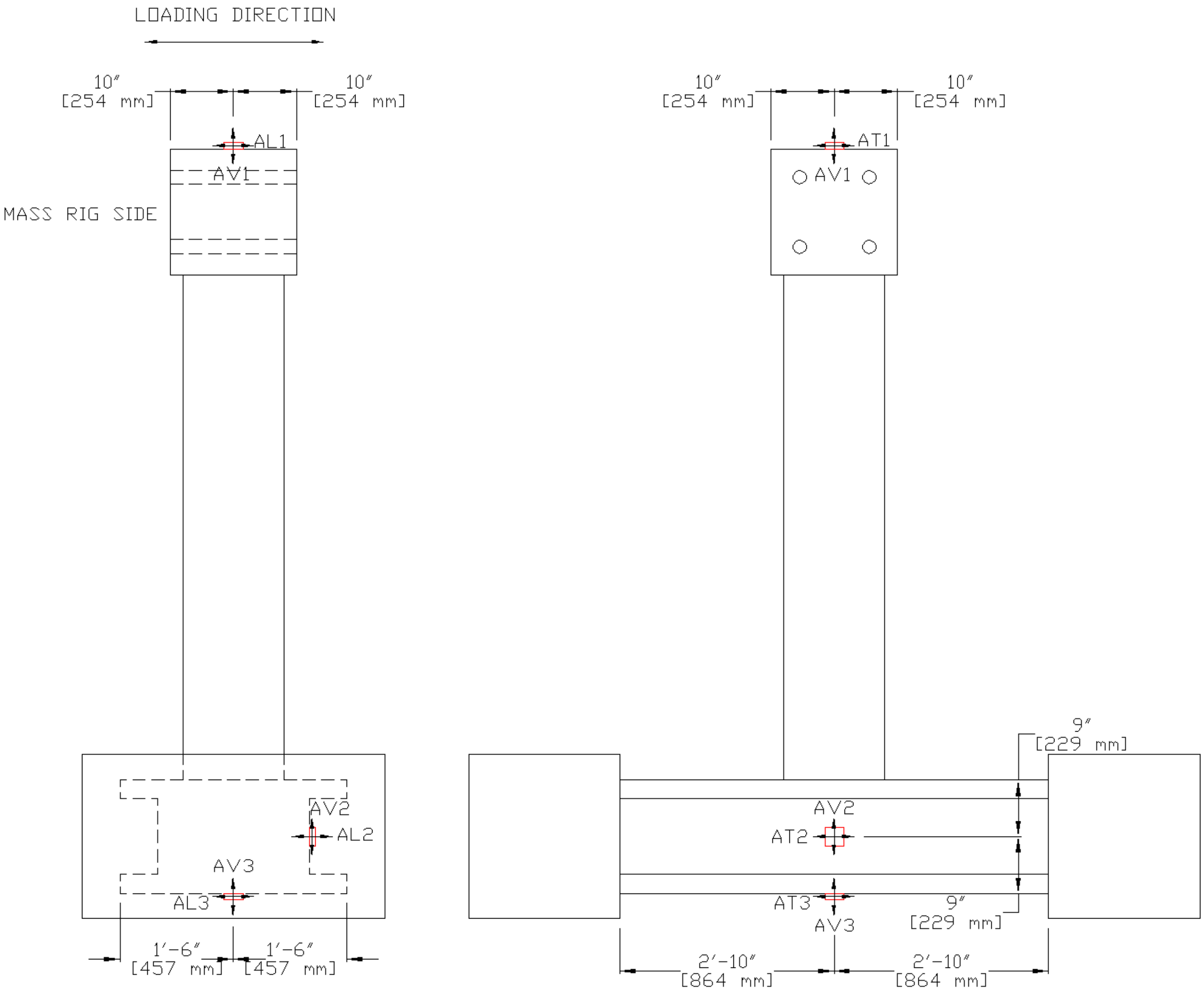

Figure 2.25 Location of accelerometers on the test specimen

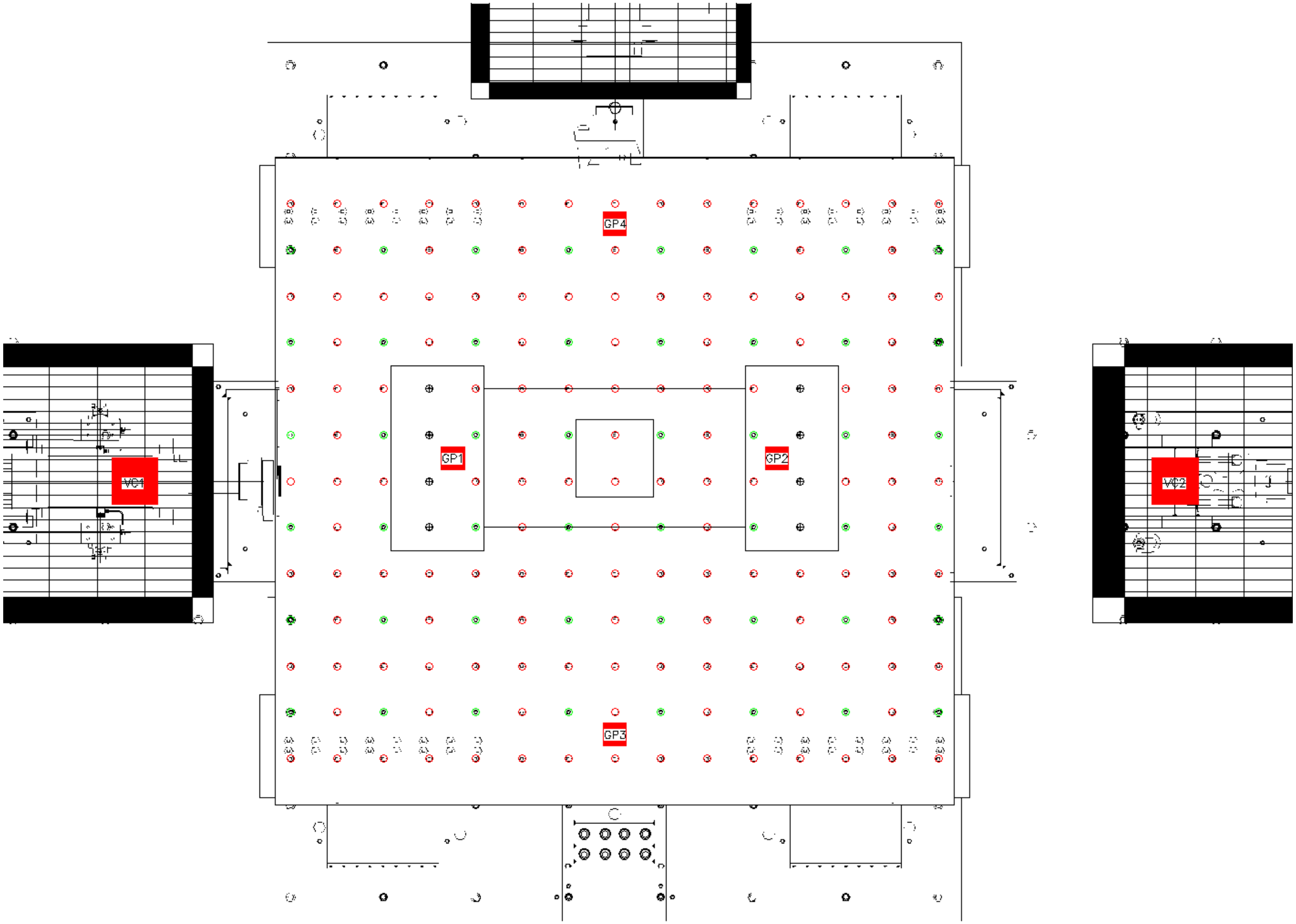

Figure 2.26 Location of cameras on specimen

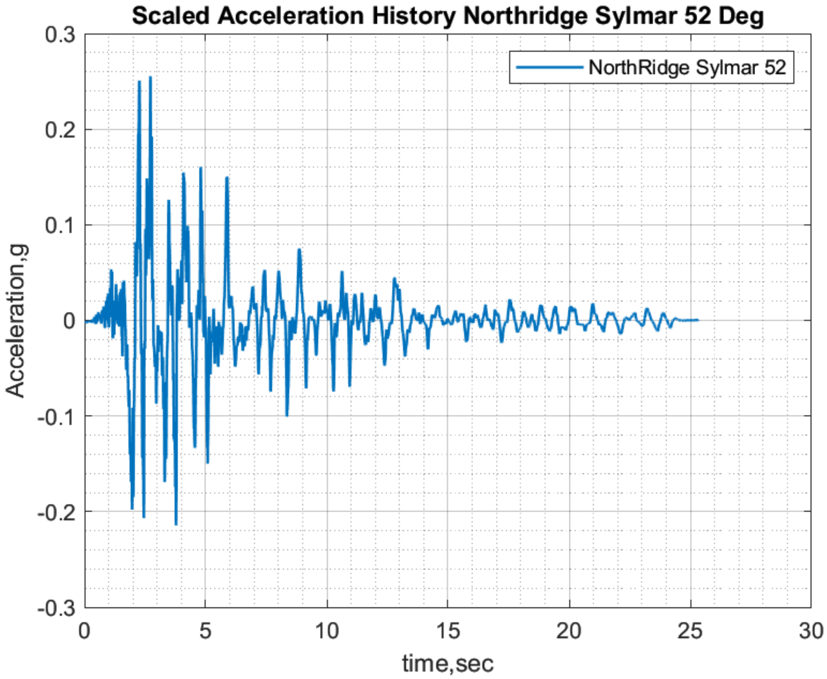

Figure 2.27 Scaled acceleration history for Northridge earthquake Sylmar record

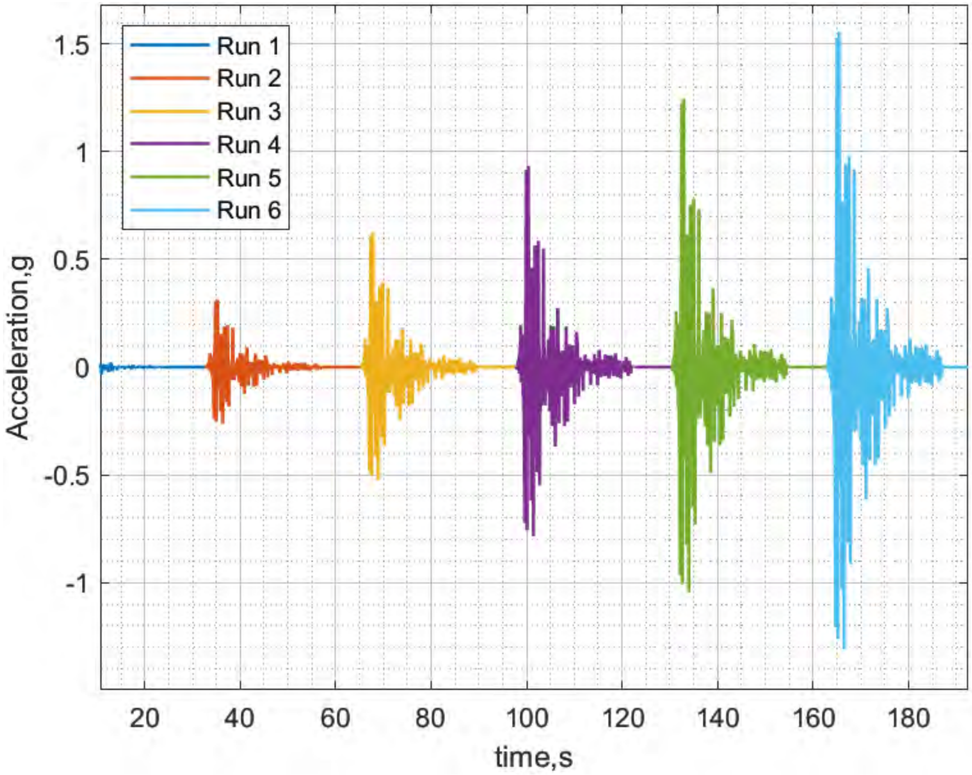

Figure 2.28 Acceleration history for runs 1-6

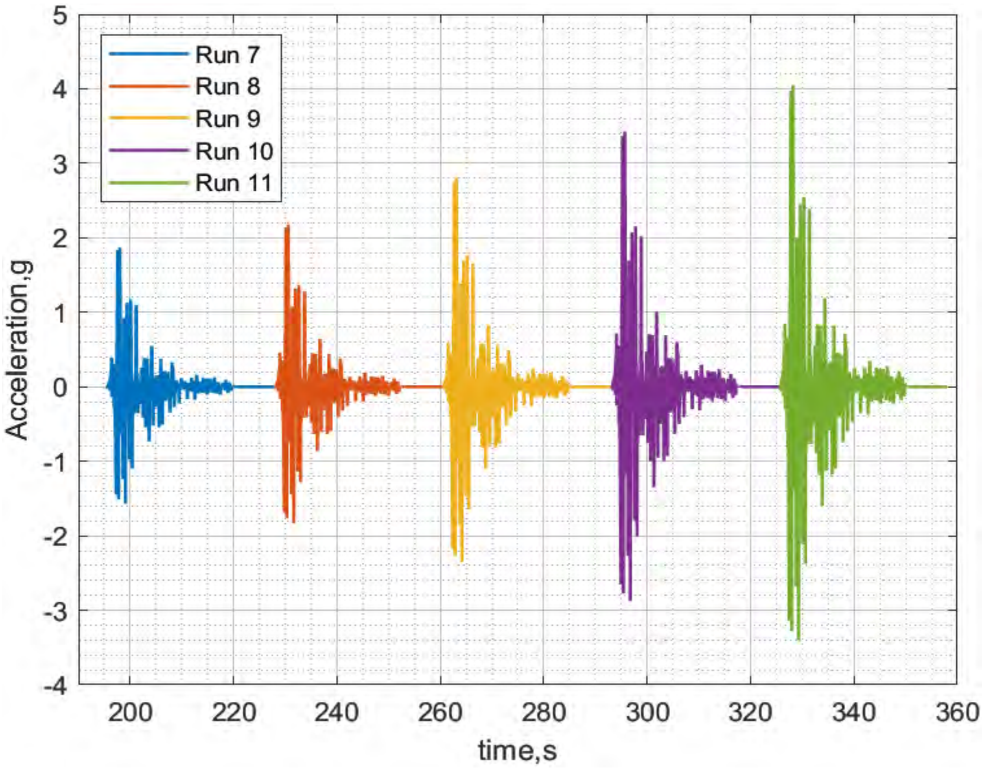

Figure 2.29 Acceleration history for runs 7-11

CHAPTER 3 FIGURES

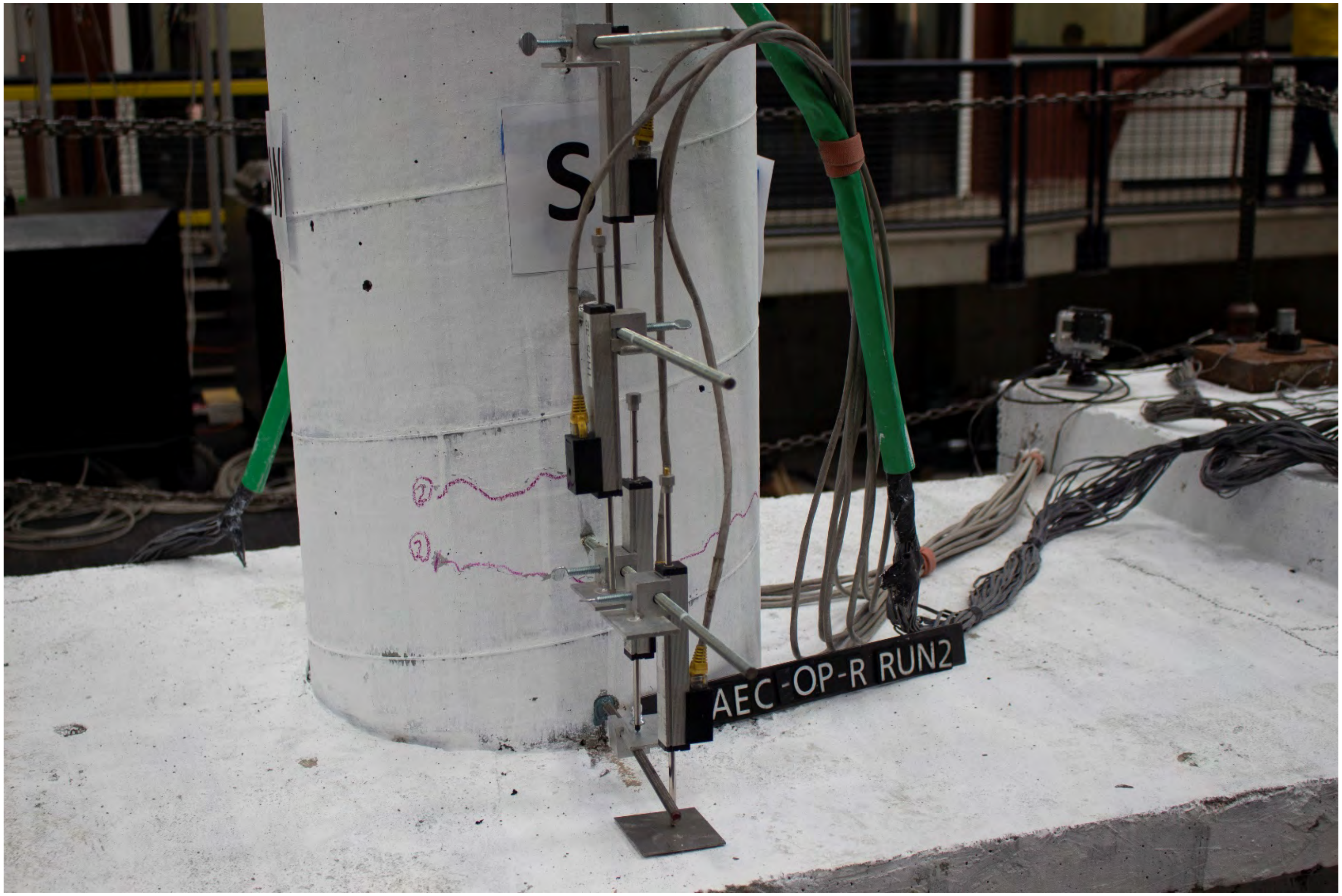

Figure 3.1 Flexural cracks (run #2)

Figure 3.2 Additional flexural cracks (run #3)

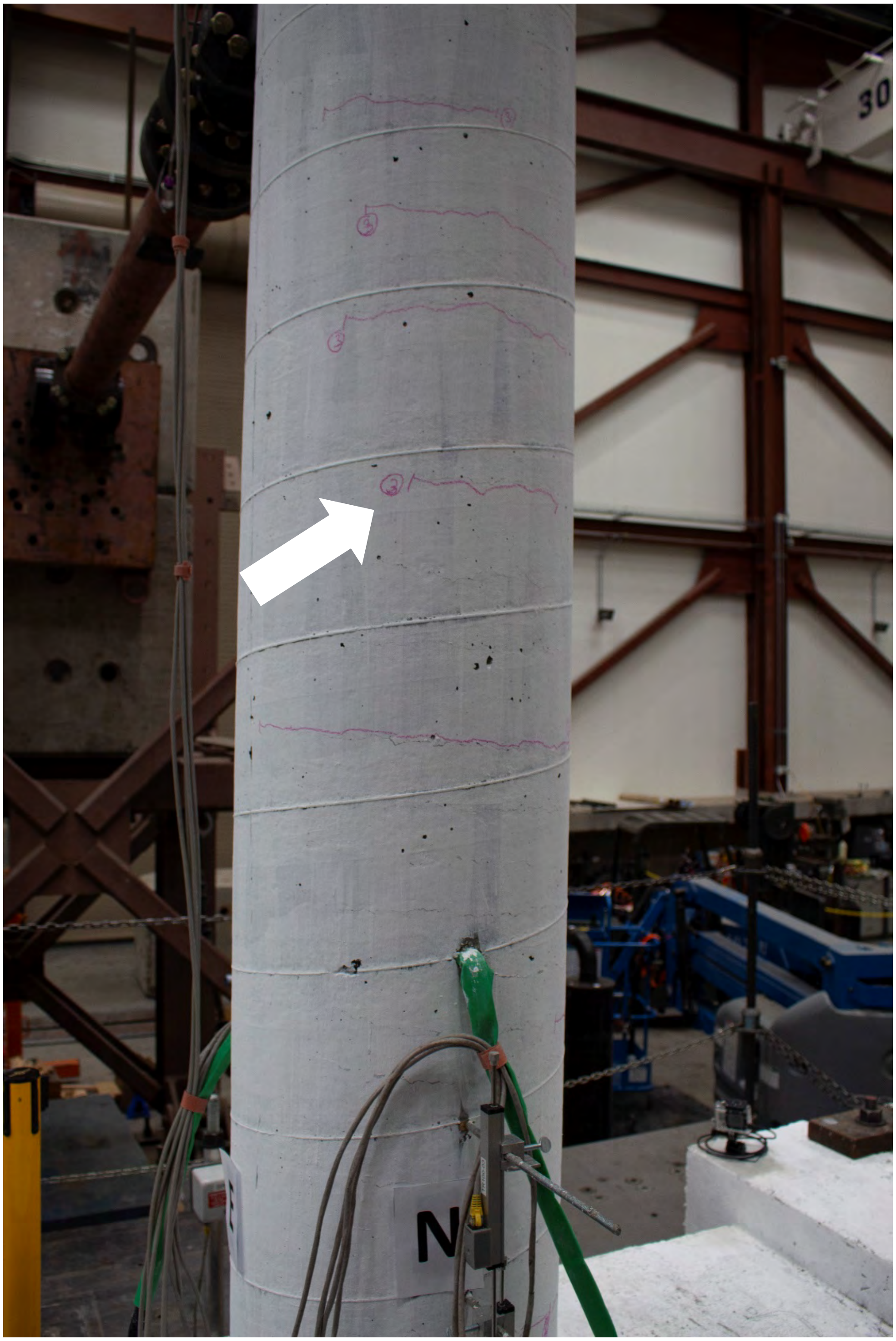

Figure 3.3 Flexural cracks on the upper part of the column (run #3)

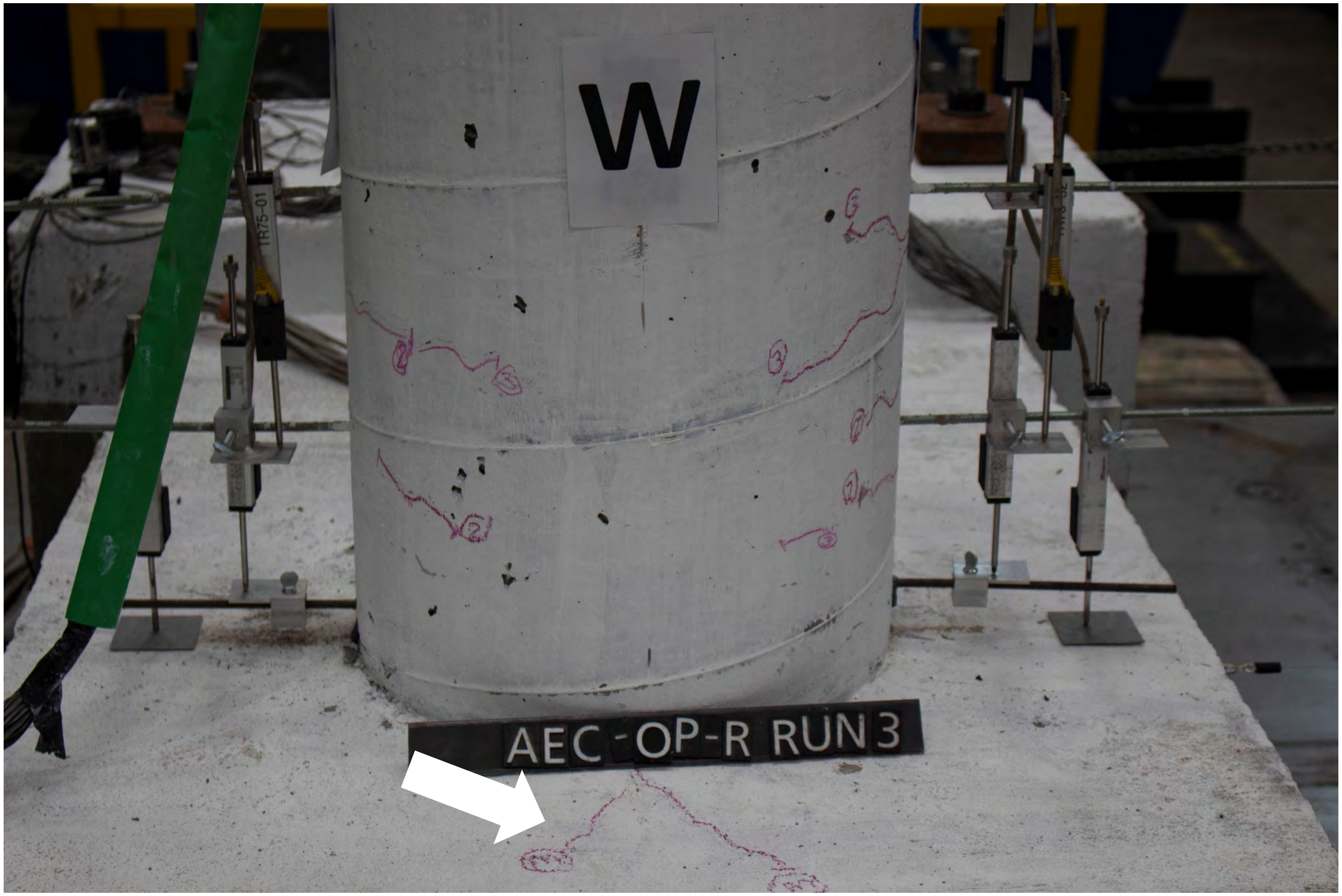

Figure 3.4 Shear cracks on the cap beam (run #3)

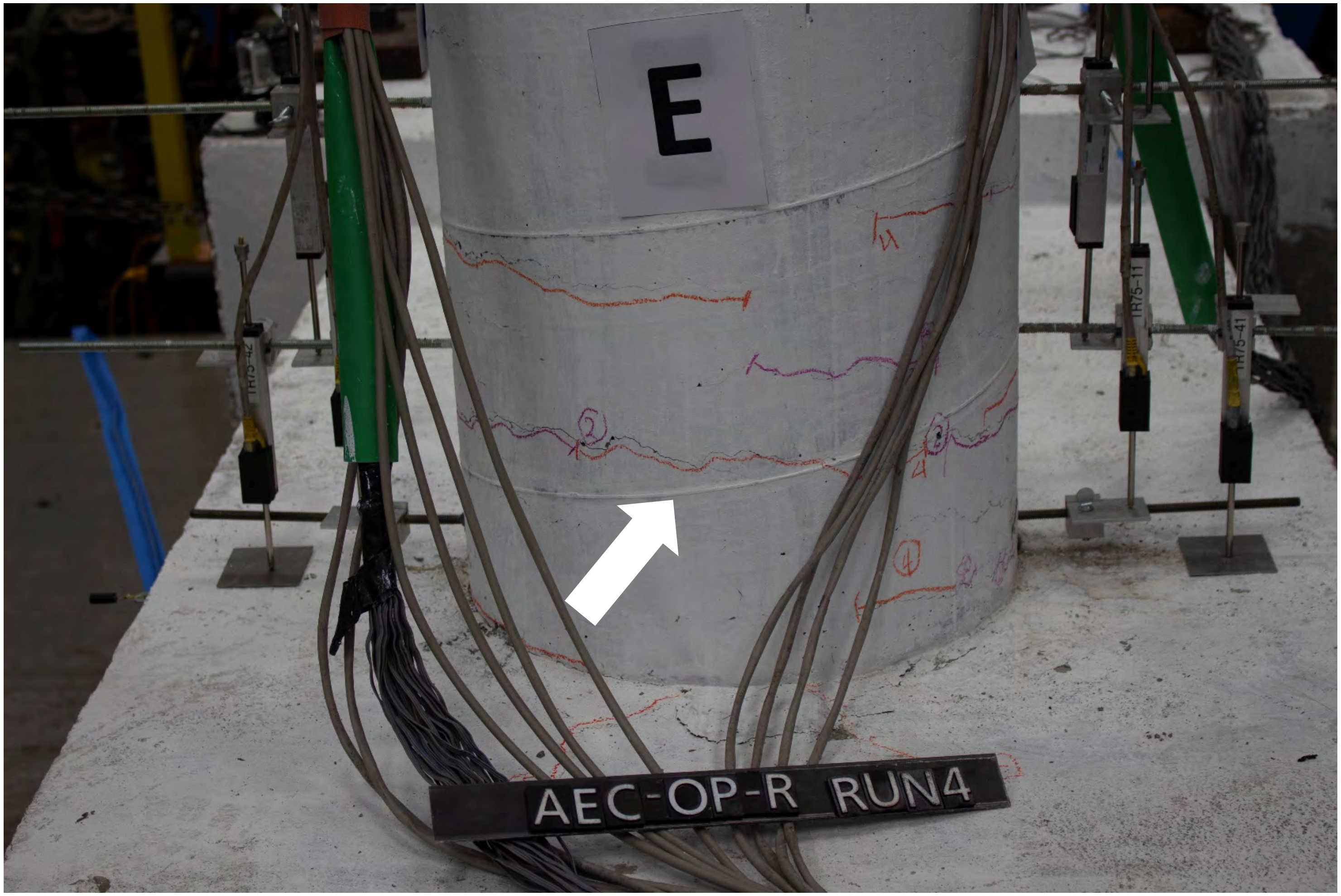

Figure 3.5 Flexural cracks extending on the east side (run #4)

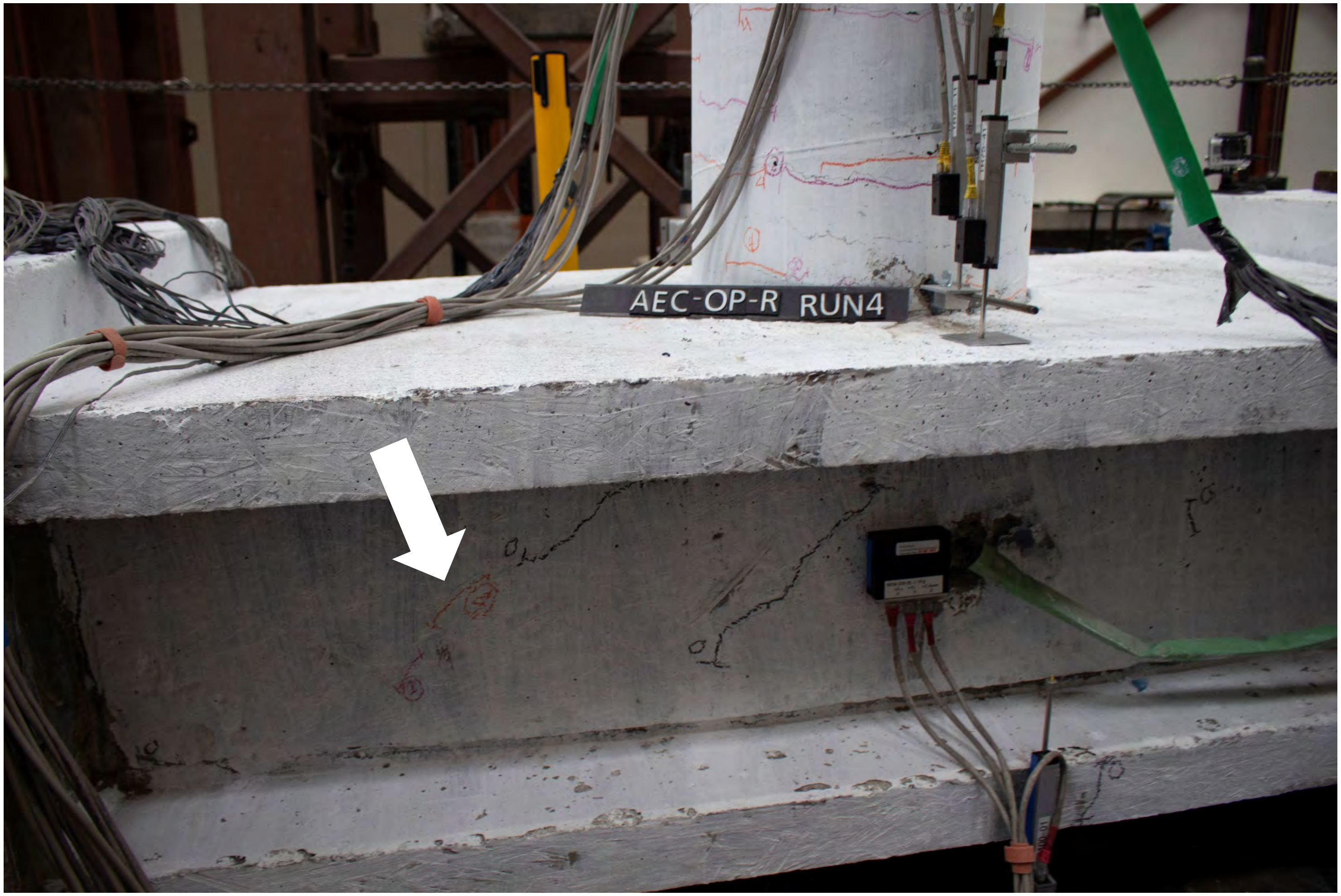

Figure 3.6 Shear crack occurring on the north side cap beam (run #4)

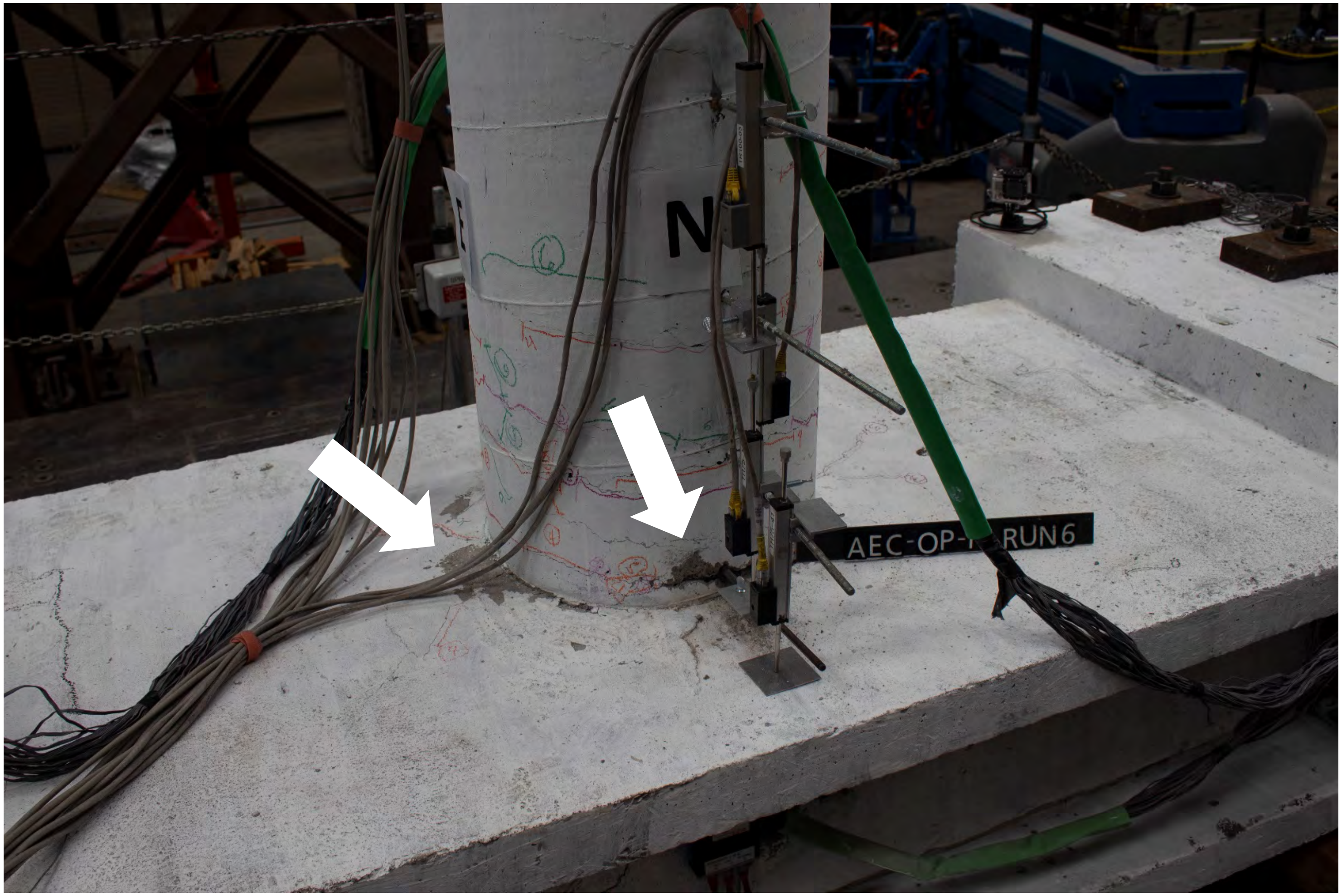

Figure 3.7 Spalling on the north side and cap beam (run #6)

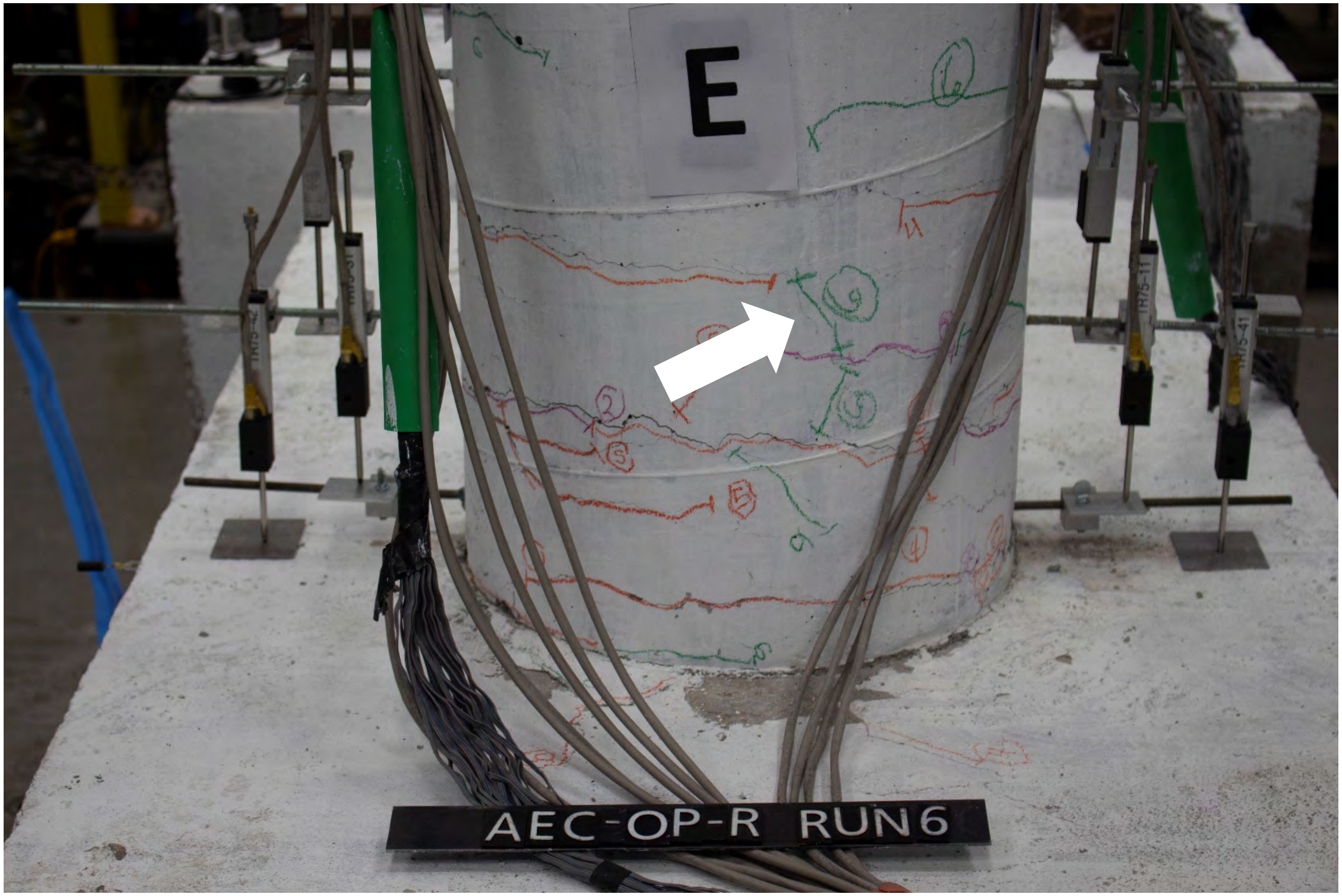

Figure 3.8 Shear cracks forming in the east side plastic hinge zone (run #6)

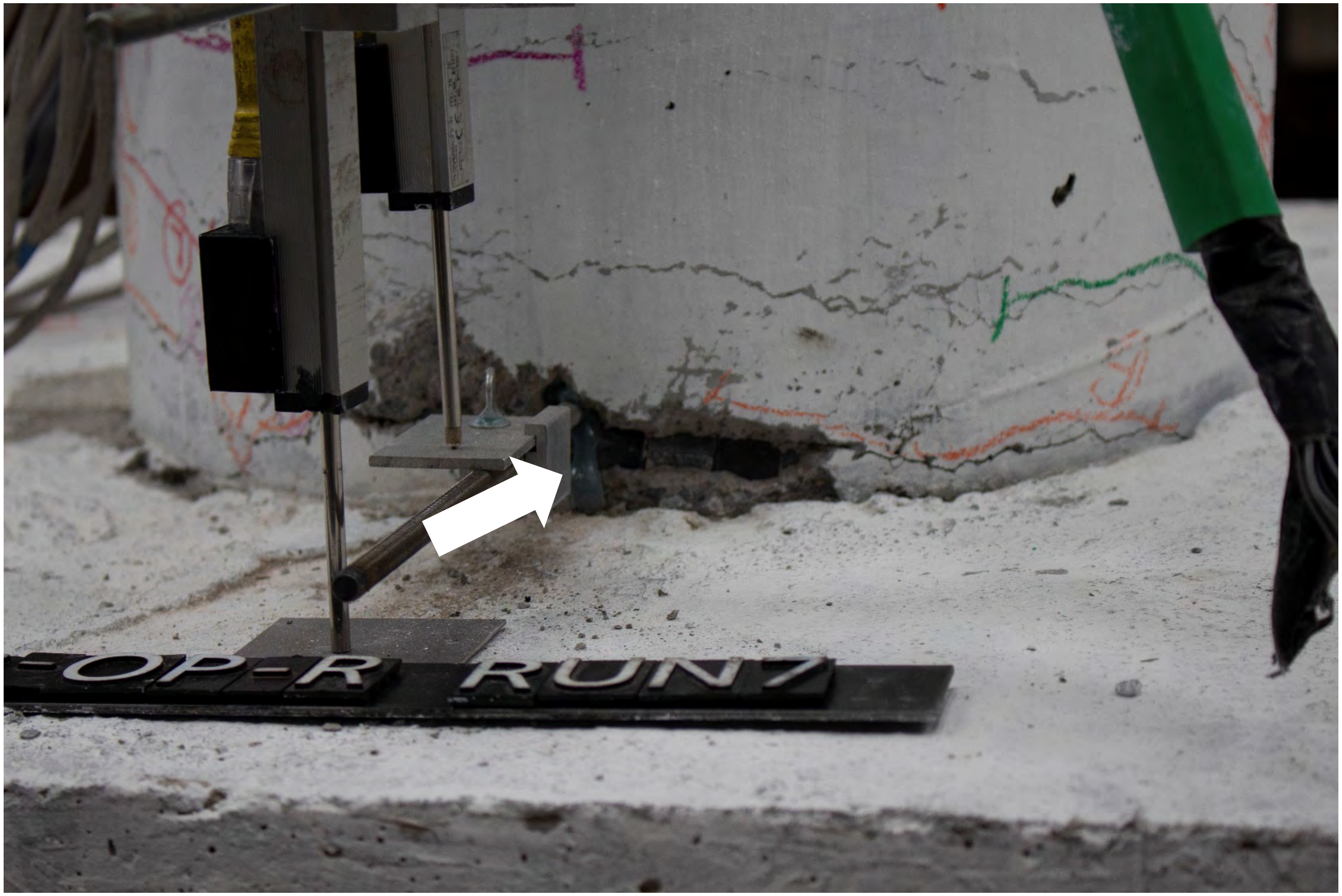

Figure 3.9 Exposed spiral reinforcement in the north side (run #7)

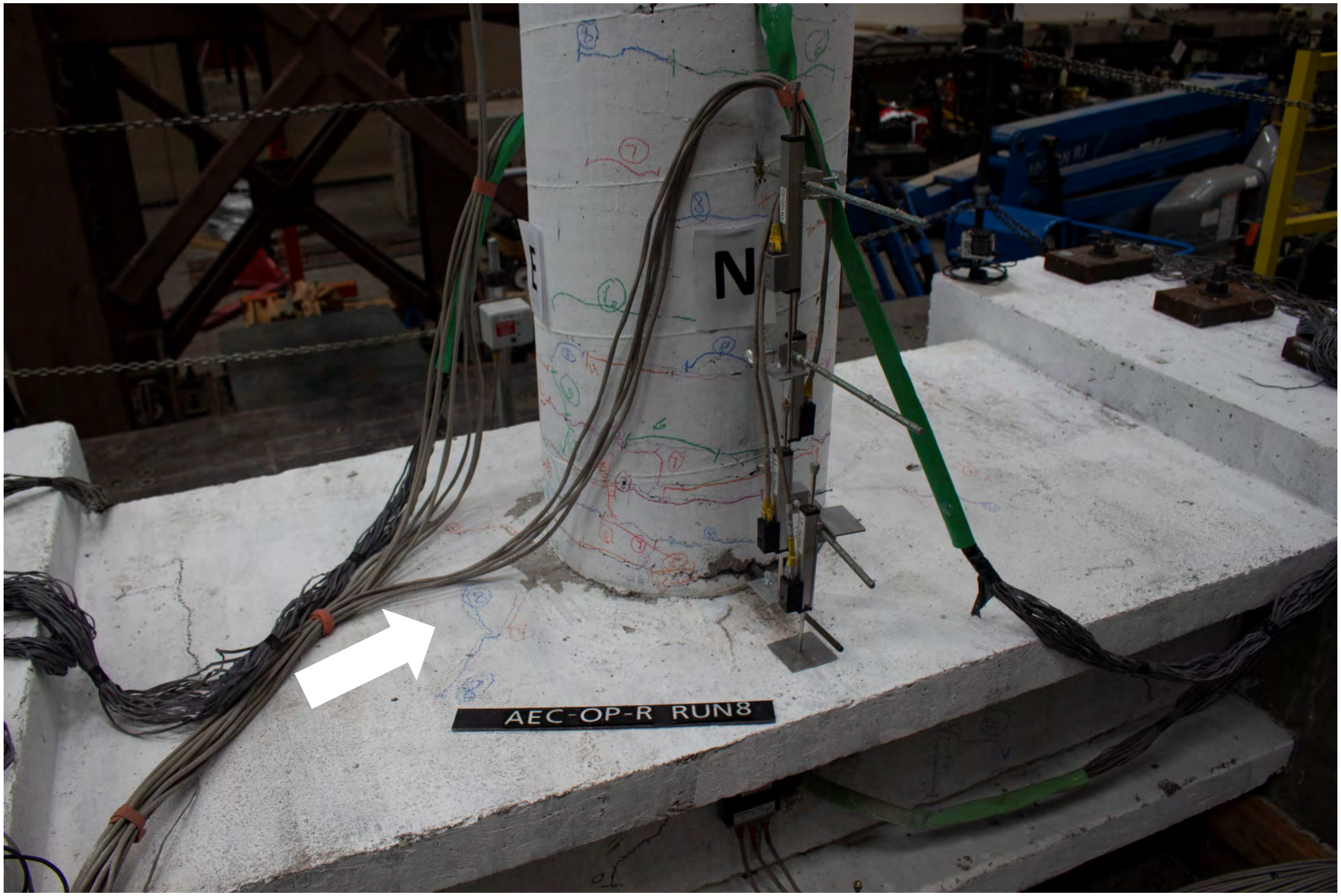

Figure 3.10 Shear crack in the cap beam interface (run #8)

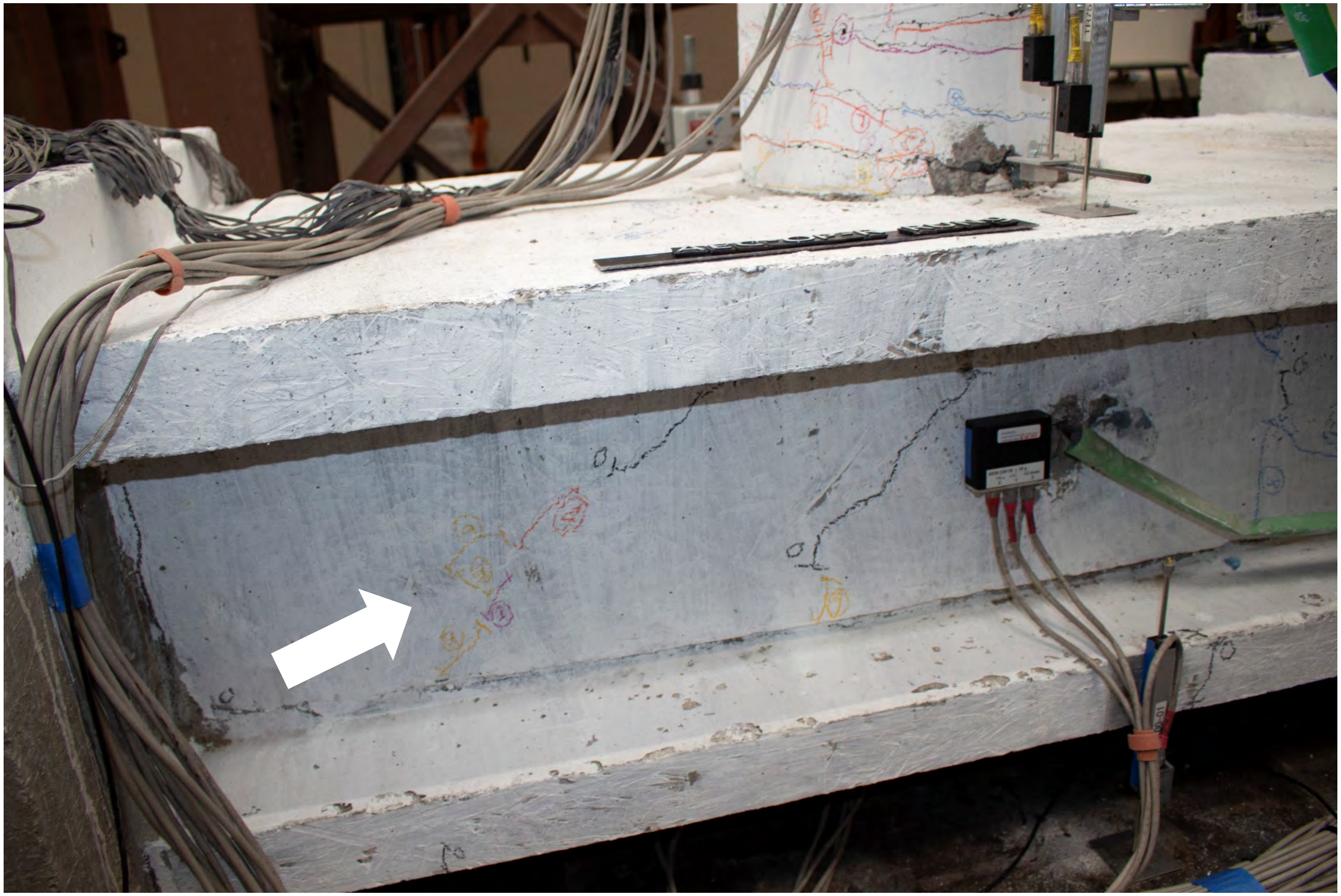

Figure 3.11 Shear crack in the cap beam web (run #9)

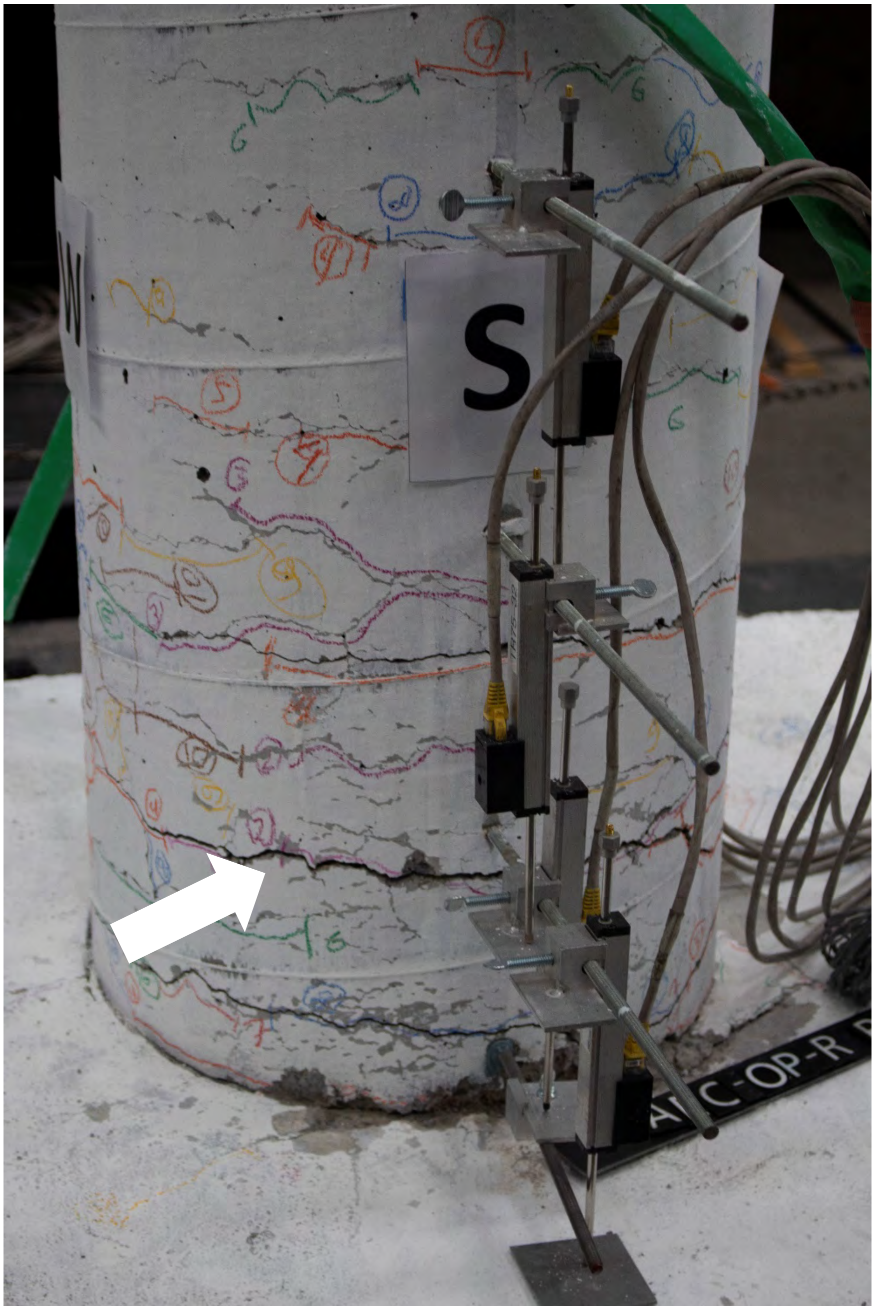

Figure 3.12 Flexure cracks widening in the south side (run #10)

Figure 3.13 Concrete spalling in the north direction (run #10)

Figure 3.14 Concrete spalling in the north direction (run #11)

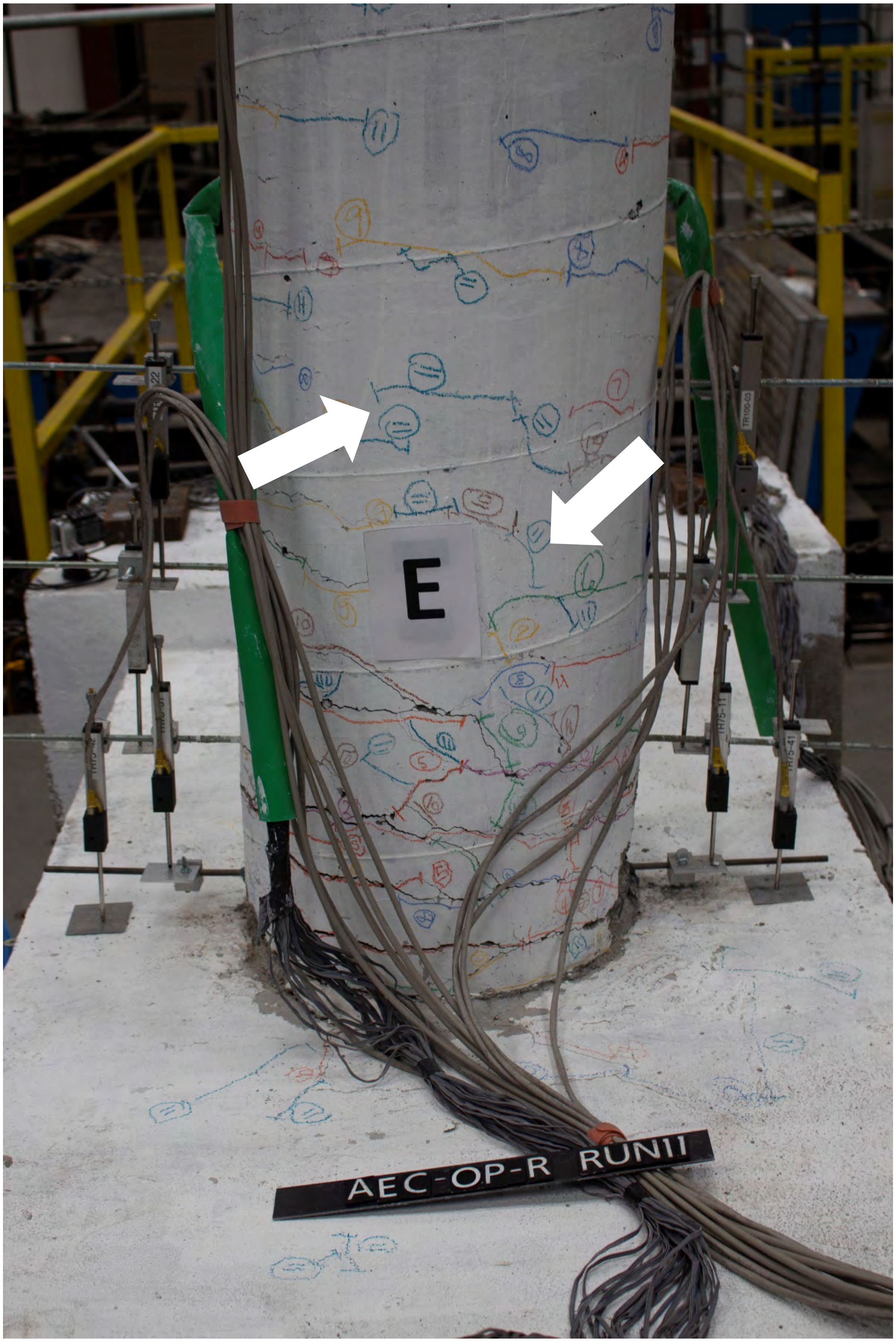

Figure 3.15 Additional flexural and shear cracks (run #11)

Figure 3.16 Spalling on the north side (run #12)

Figure 3.17 Spalling and widening of flexural cracks on the south side (run #12)

Figure 3.18 Column position after run #12

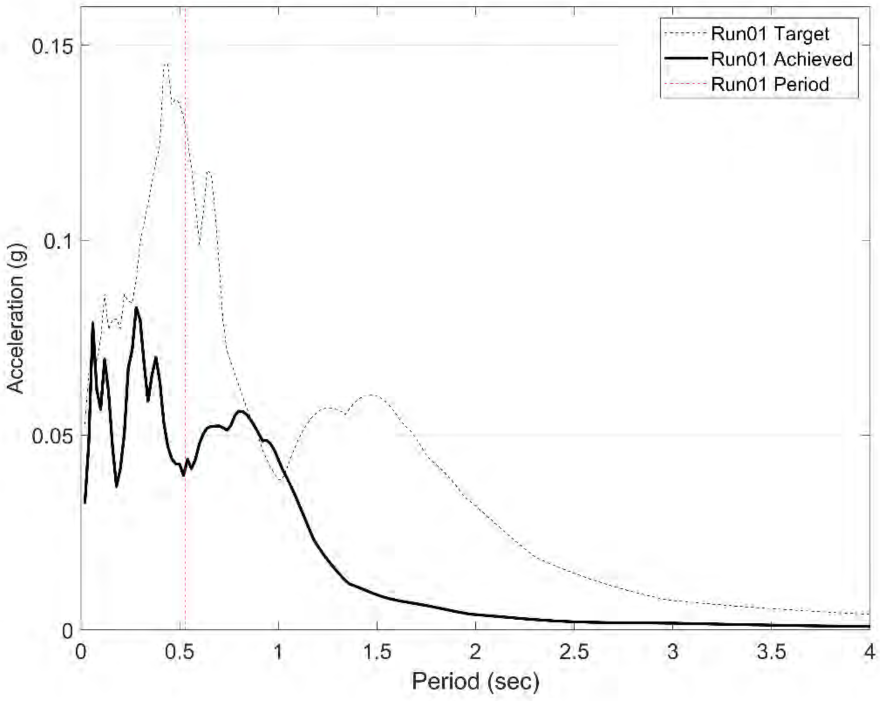

Figure 3.19 Target and achieved response spectra for run #1

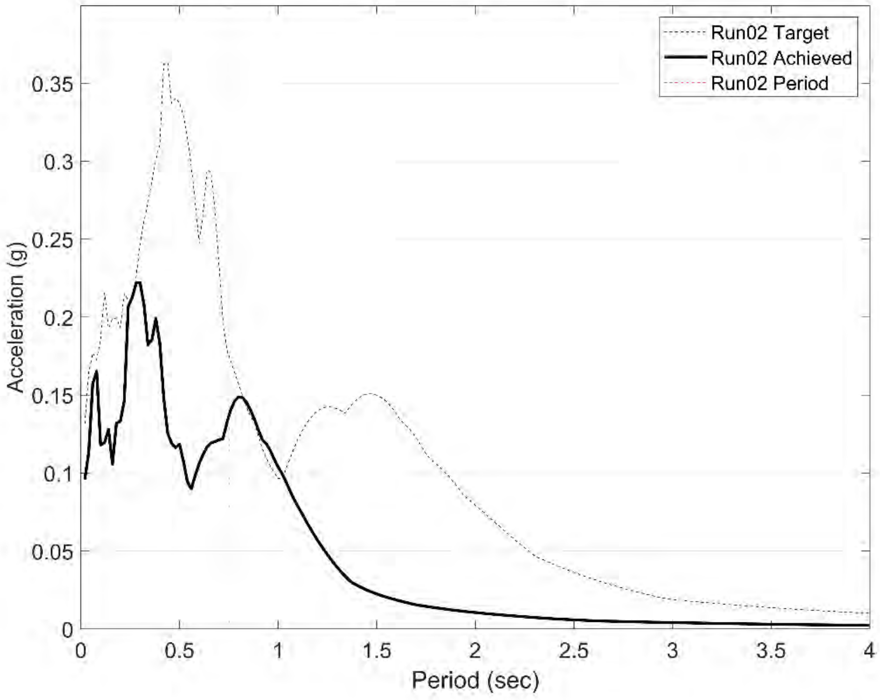

Figure 3.20 Target and achieved response spectra for run #2

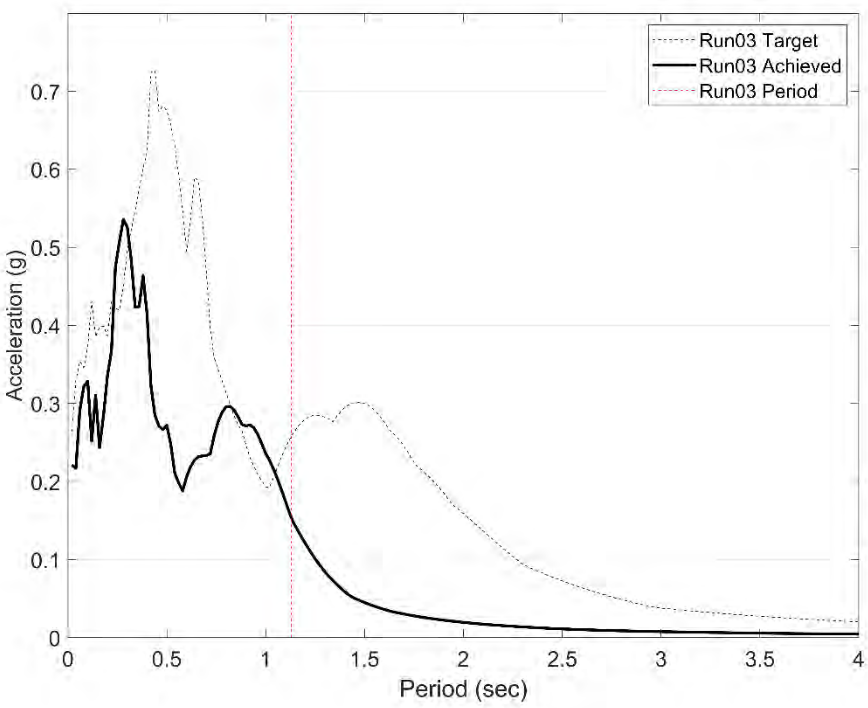

Figure 3.21 Target and achieved response spectra for run #3

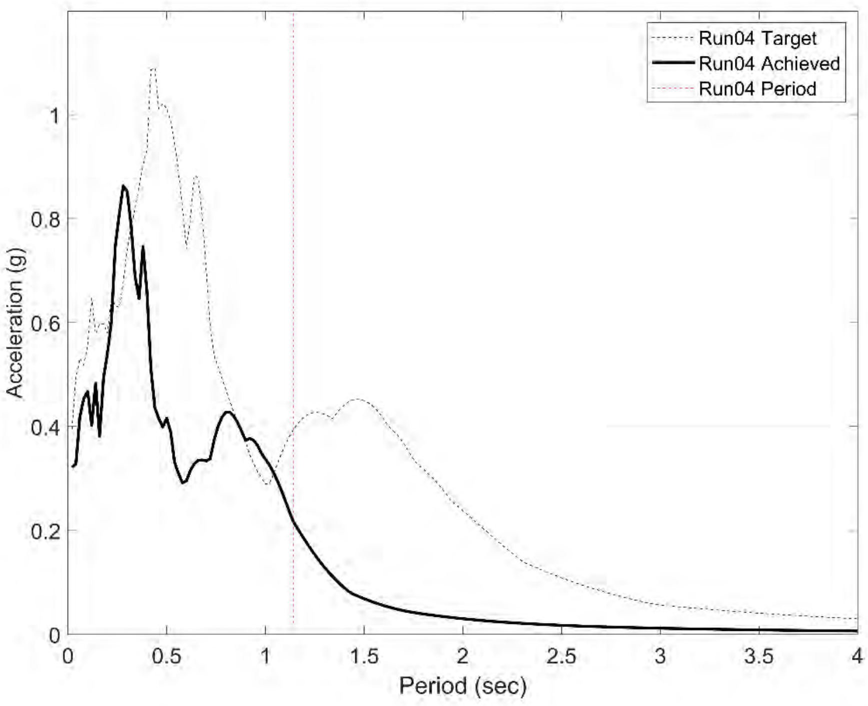

Figure 3.22 Target and achieved response spectra for run #4

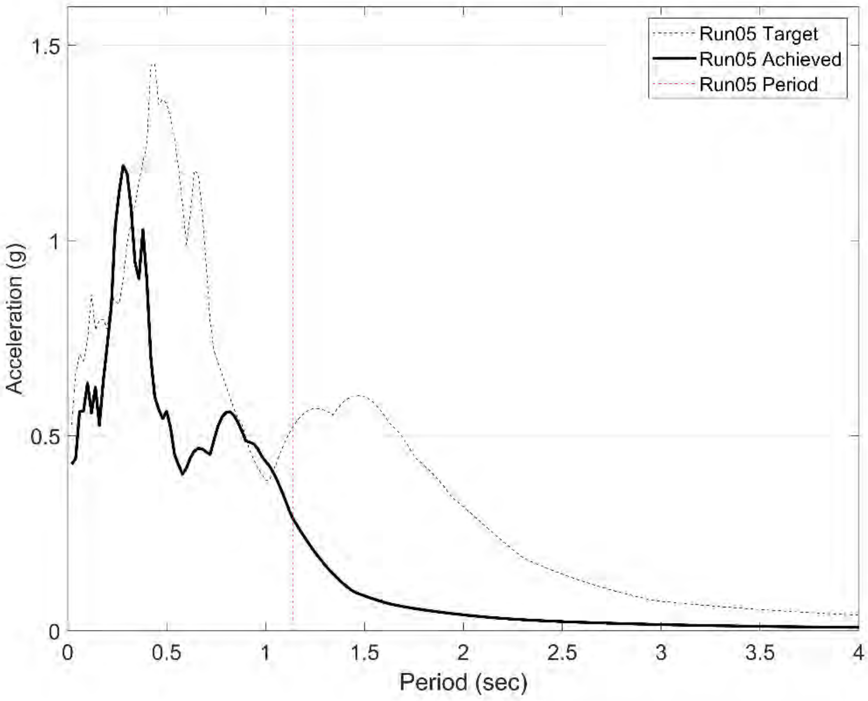

Figure 3.23 Target and achieved response spectra for run #5

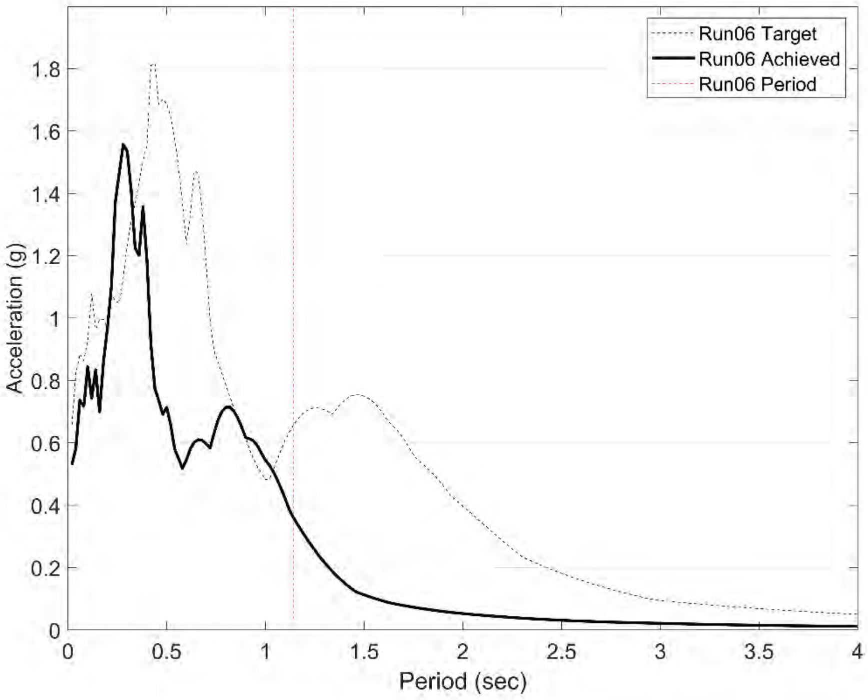

Figure 3.24 Target and achieved response spectra for run #6

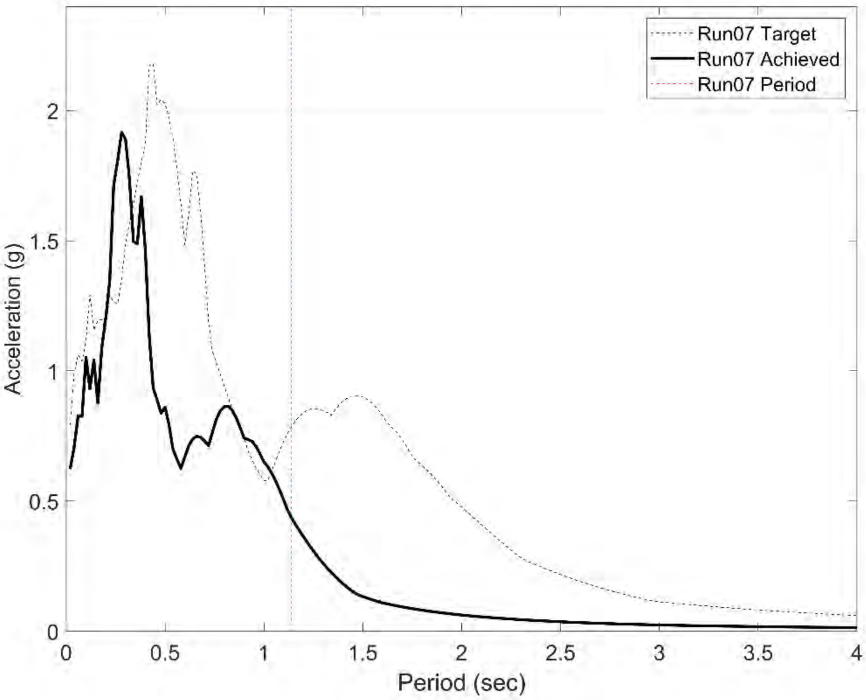

Figure 3.25 Target and achieved response spectra for run #7

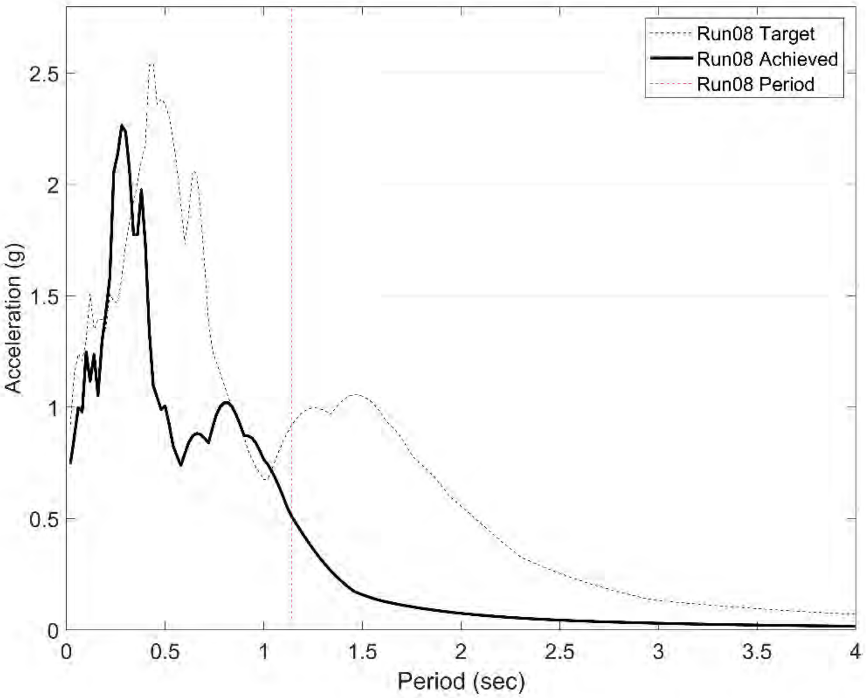

Figure 3.26 Target and achieved response spectra for run #8

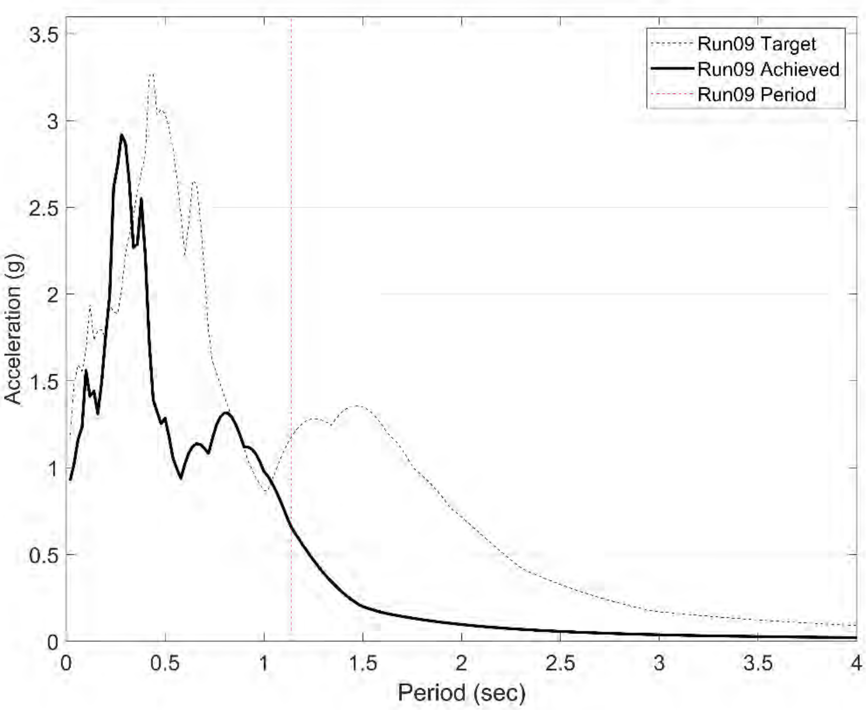

Figure 3.27 Target and achieved response spectra for run #9

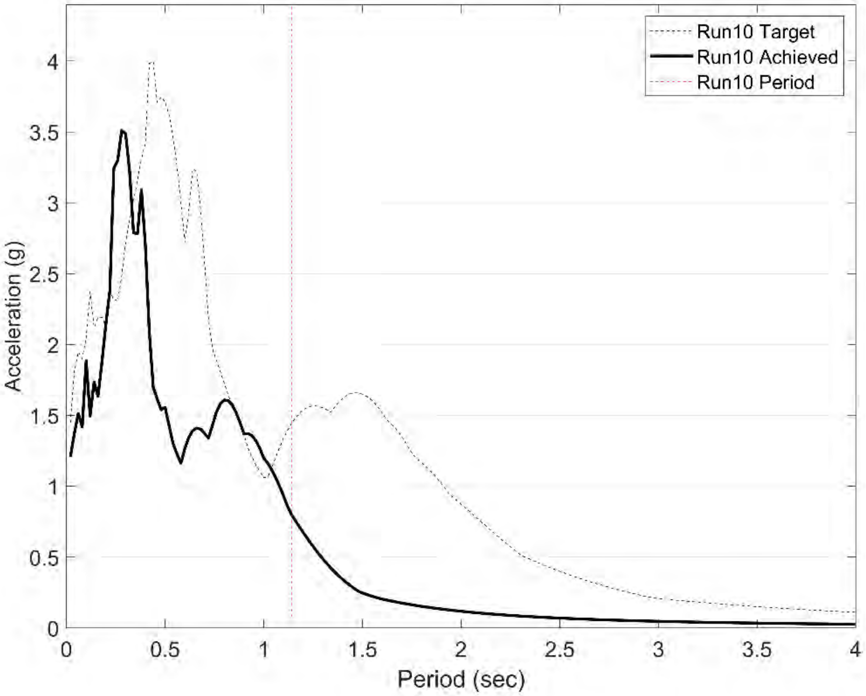

Figure 3.28 Target and achieved response spectra for run #10

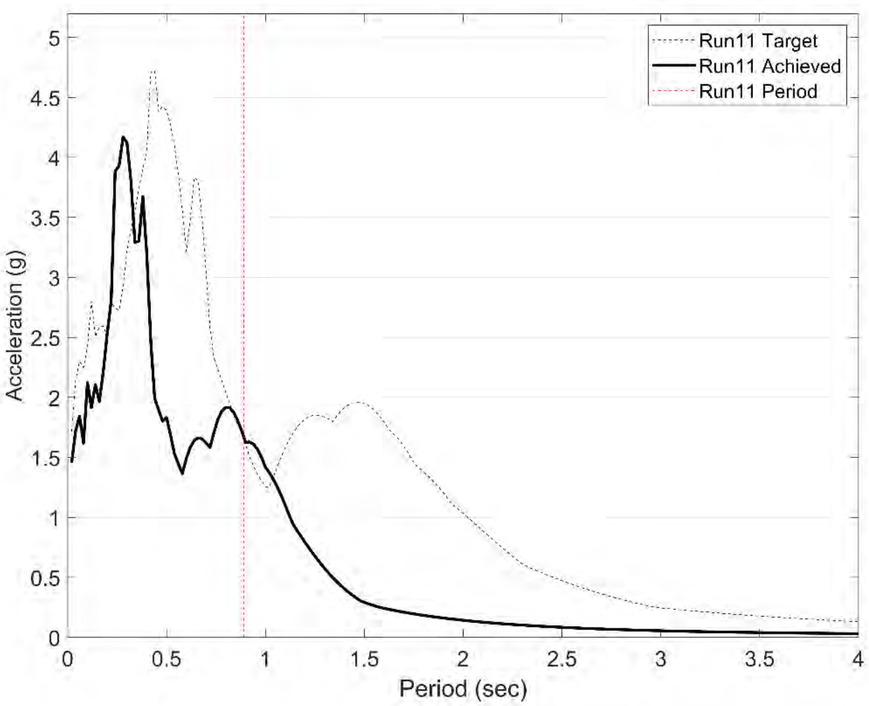

Figure 3.29 Target and achieved response spectra for run #11

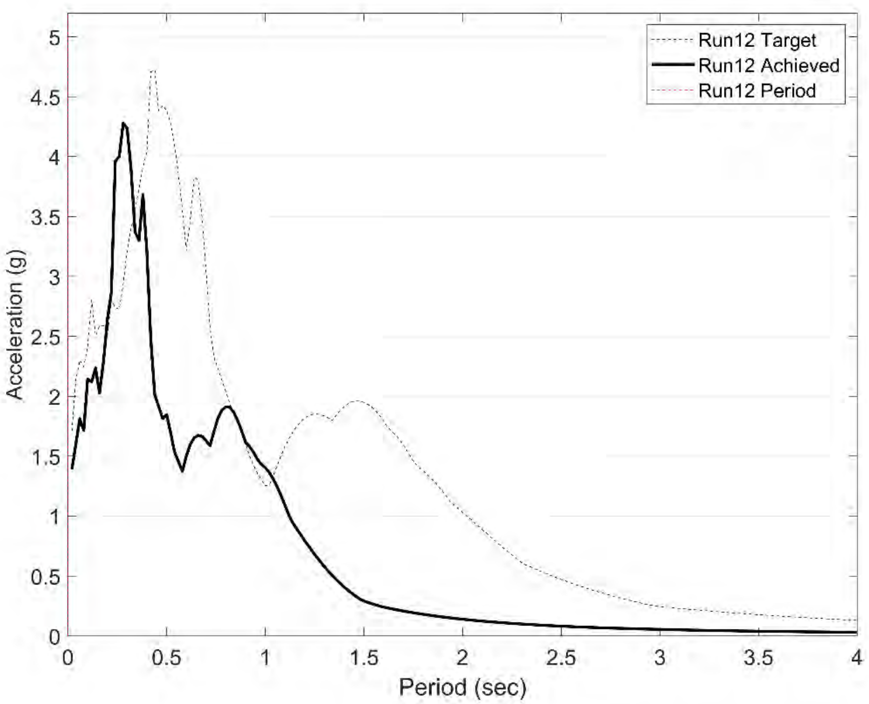

Figure 3.30 Target and achieved response spectra for run #12

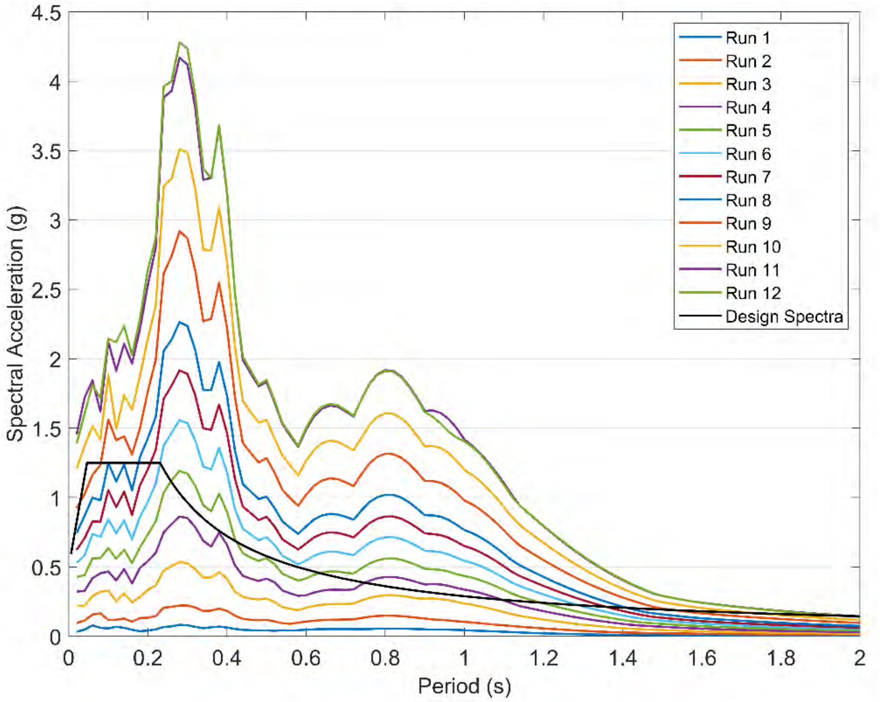

Figure 3.31 Achieved response spectra compared to seismic design response spectrum

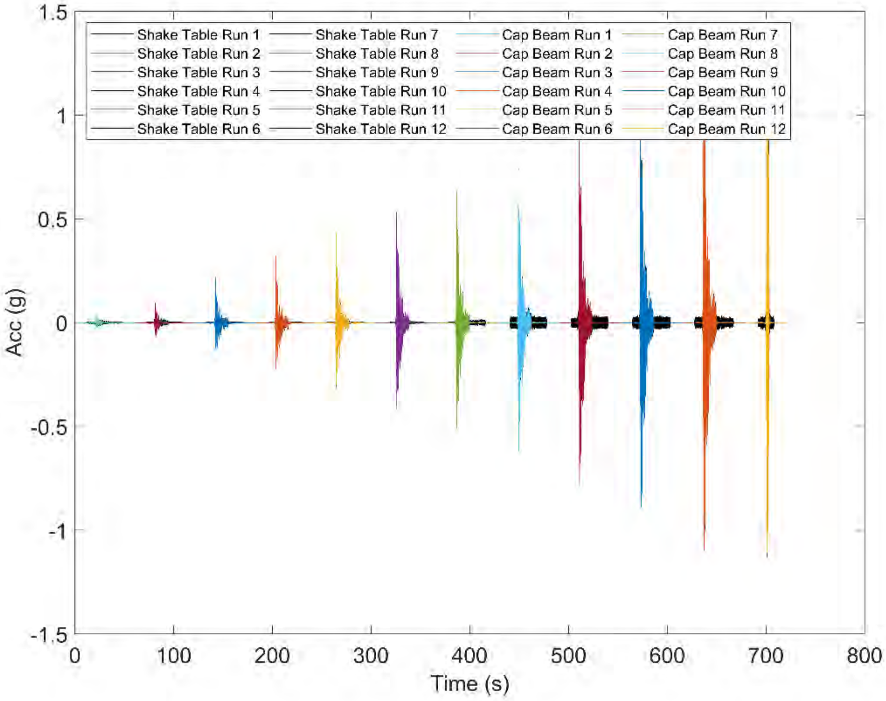

Figure 3.32 Comparison of cap beam and shake table accelerations for runs 1 through 12

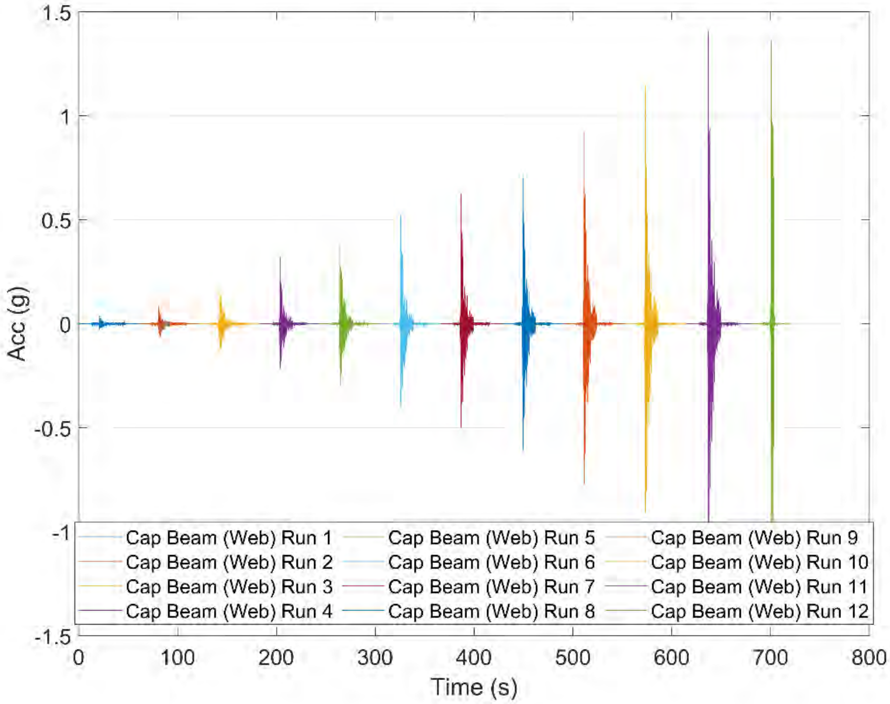

Figure 3.33 Accelerations on cap beam web for runs 1 through 12

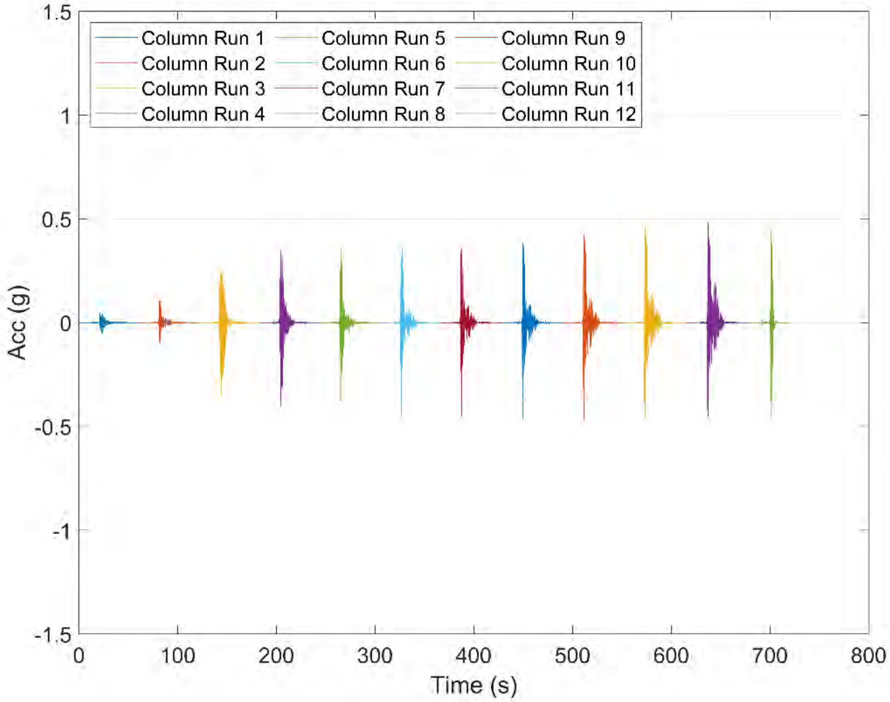

Figure 3.34 Accelerations at the top of the column for runs 1 through 12

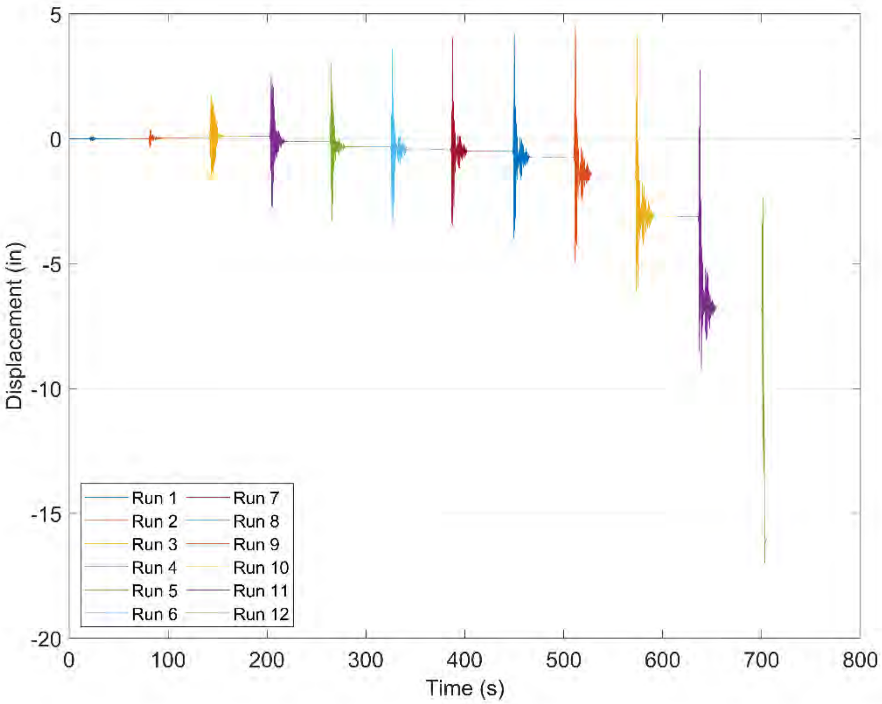

Figure 3.35 Measured relative column displacement history for runs 1 through 12

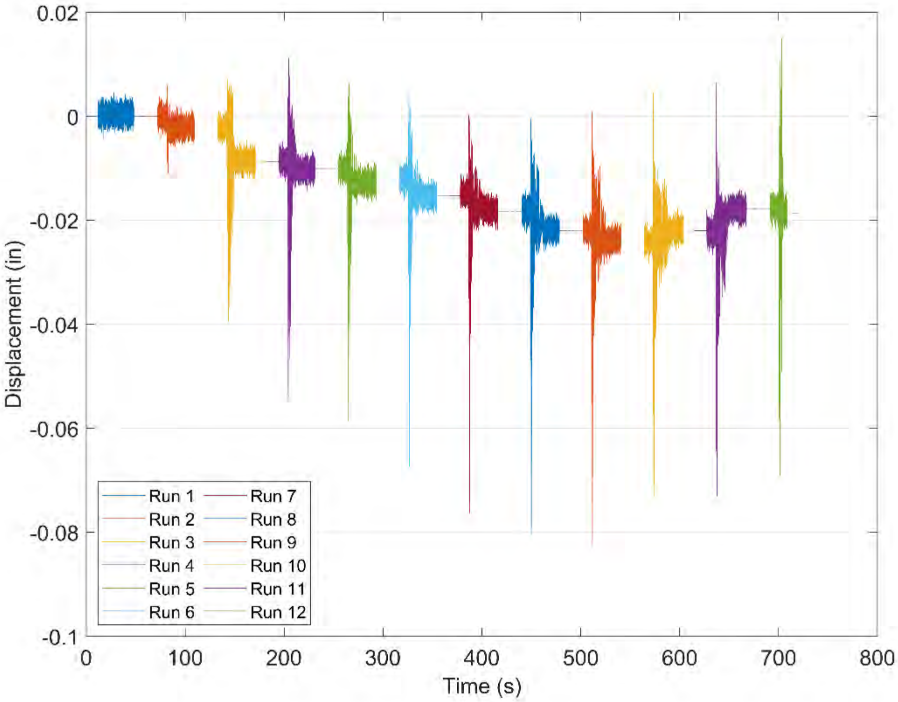

Figure 3.36 Measured cap beam displacement history for runs 1 through 12

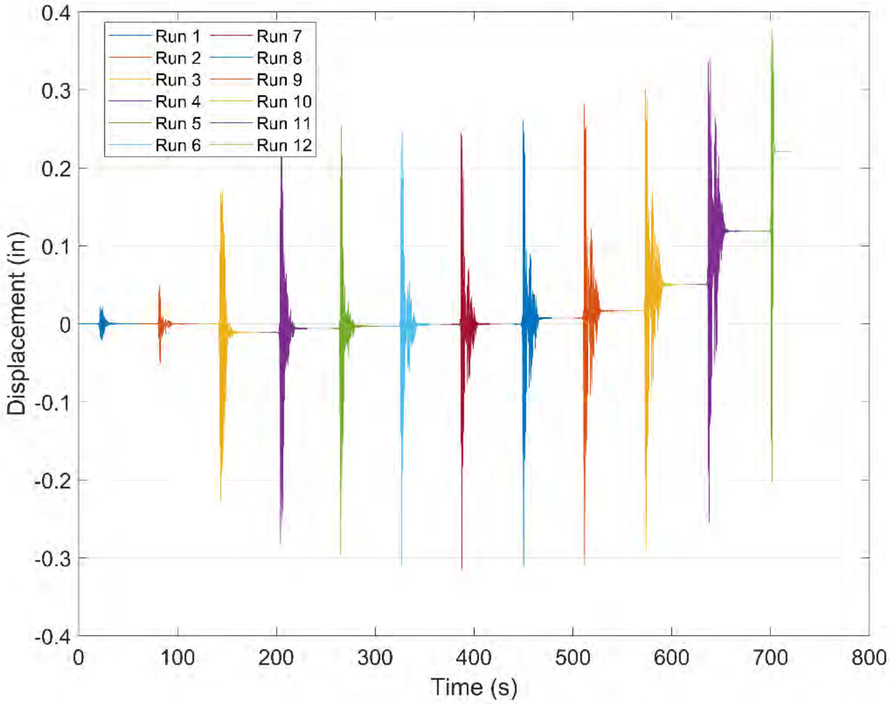

Figure 3.37 Measured displacement history at the top of the column due to cap beam twist for runs 1 through 12

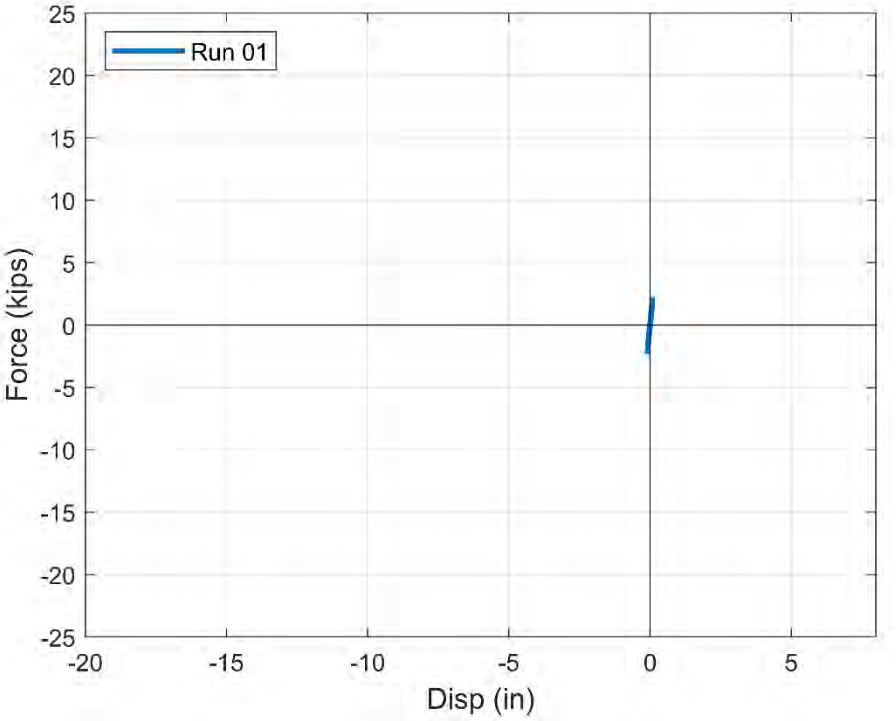

Figure 3.38 Force-displacement relationship for run #1

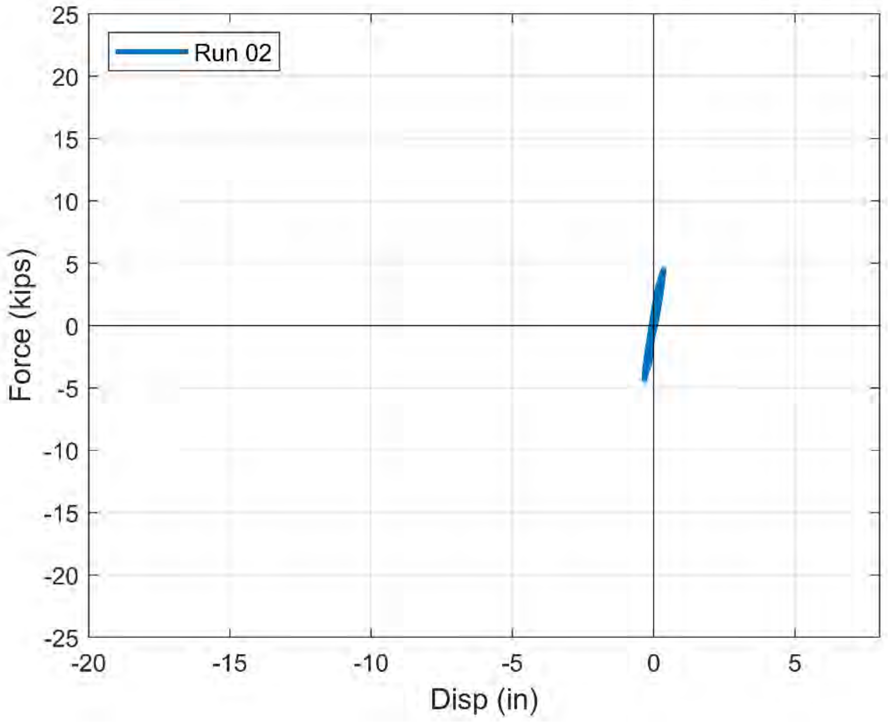

Figure 3.39 Force-displacement relationship for run #2

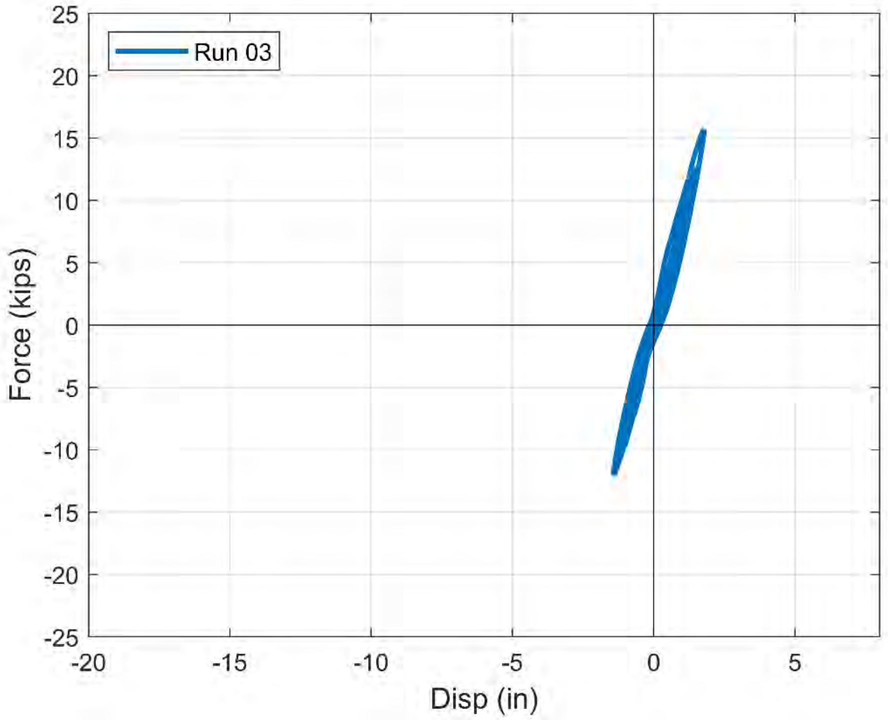

Figure 3.40 Force-displacement relationship for run #3

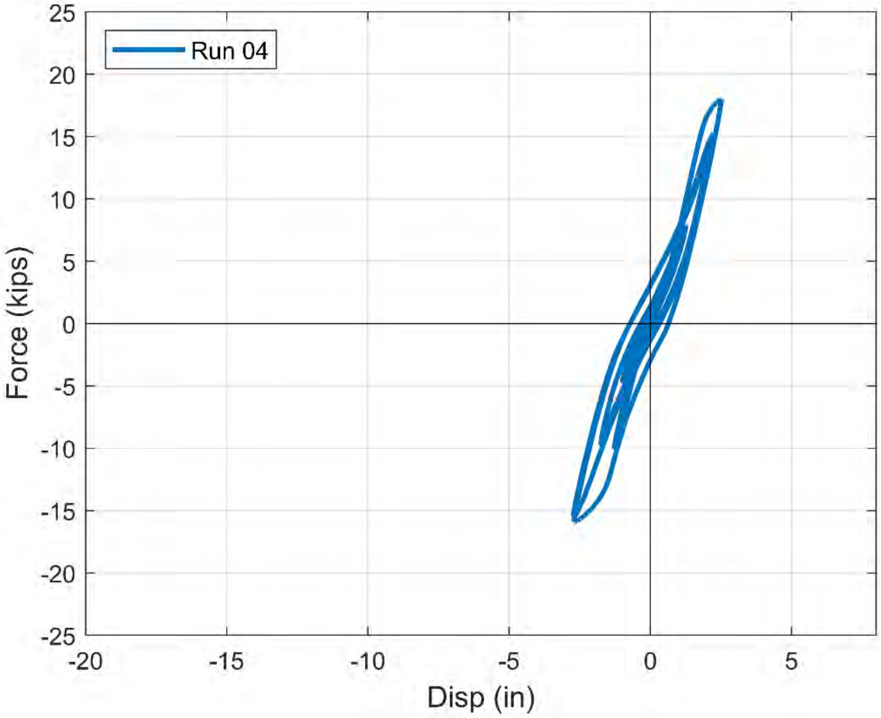

Figure 3.41 Force-displacement relationship for run #4

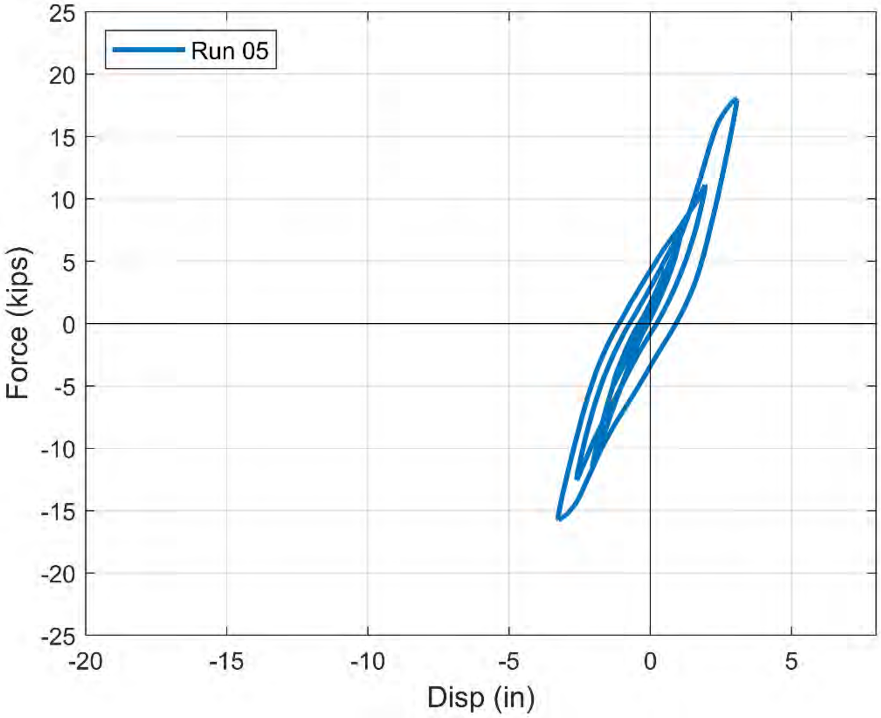

Figure 3.42 Force-displacement relationship for run #5

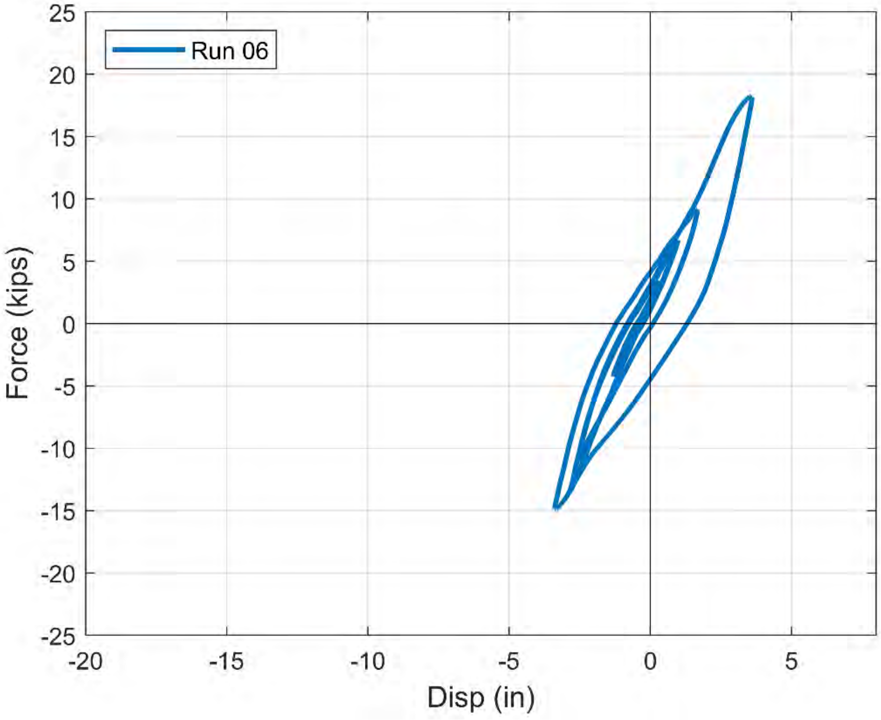

Figure 3.43 Force-displacement relationship for run #6

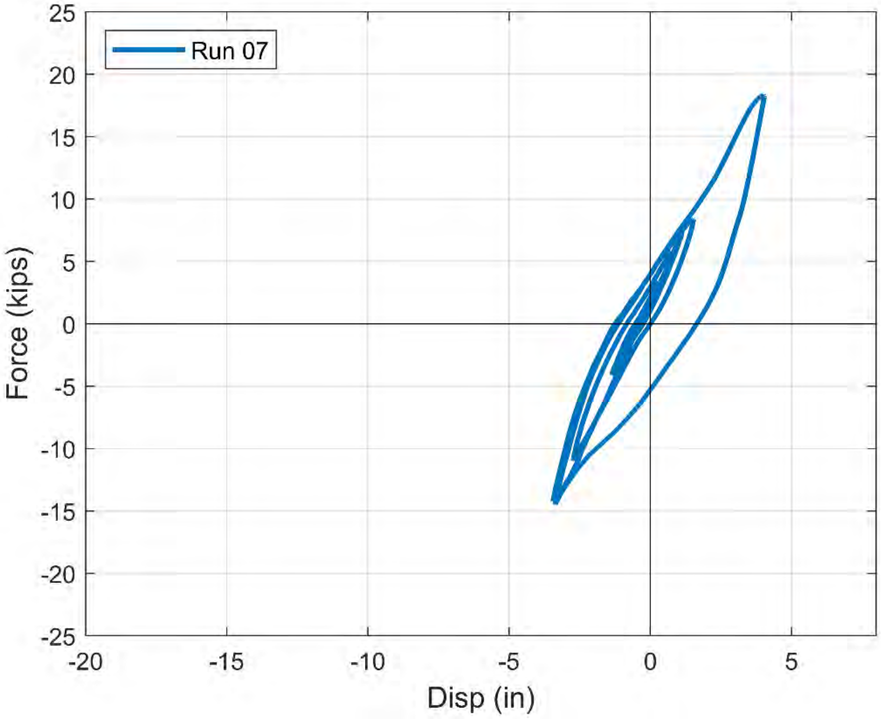

Figure 3.44 Force-displacement relationship for run #7

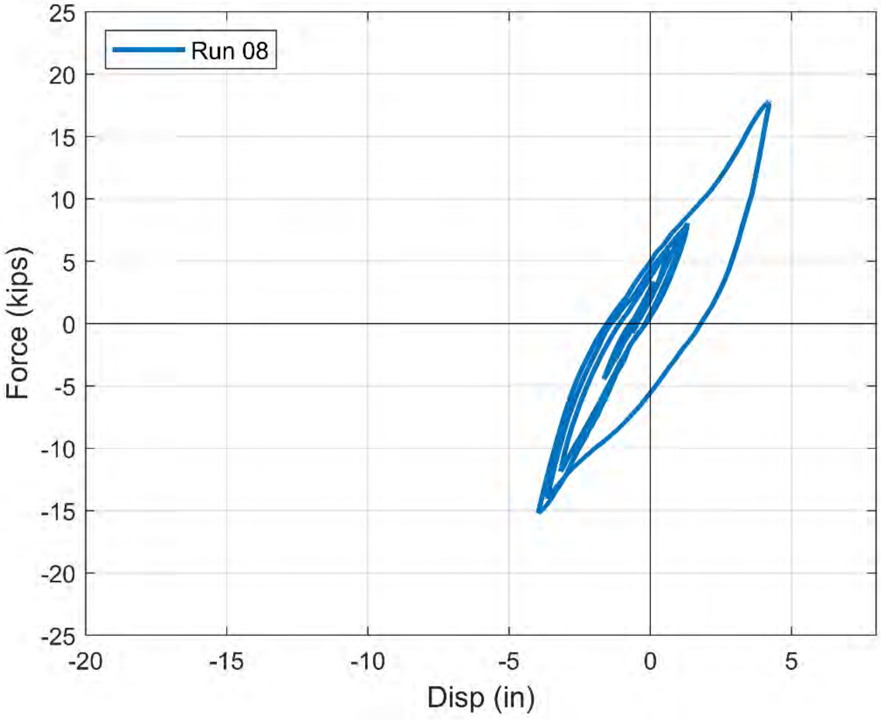

Figure 3.45 Force-displacement relationship for run #8

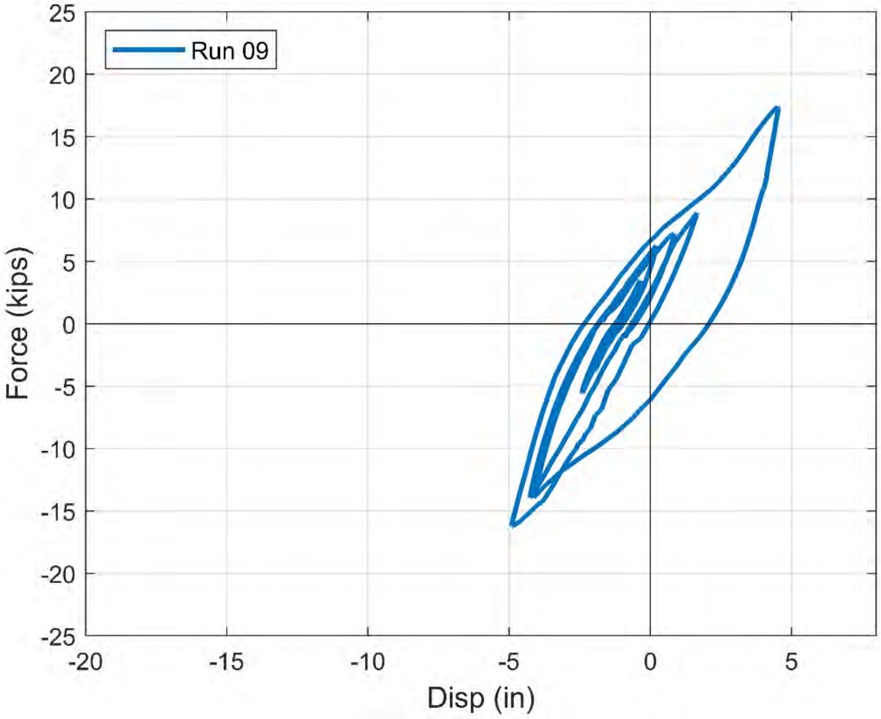

Figure 3.46 Force-displacement relationship for run #9

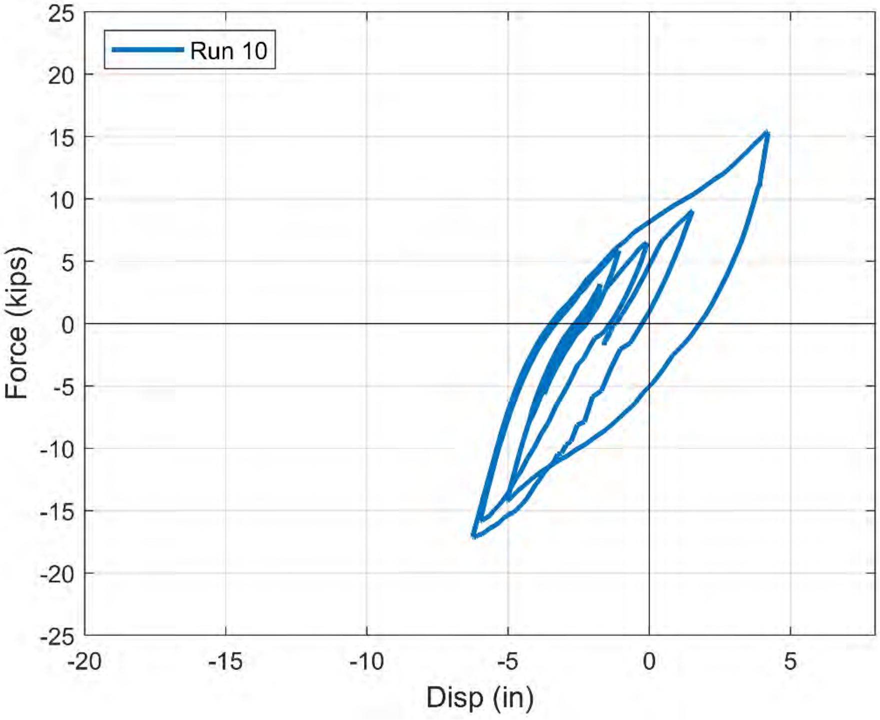

Figure 3.47 Force-displacement relationship for run #10

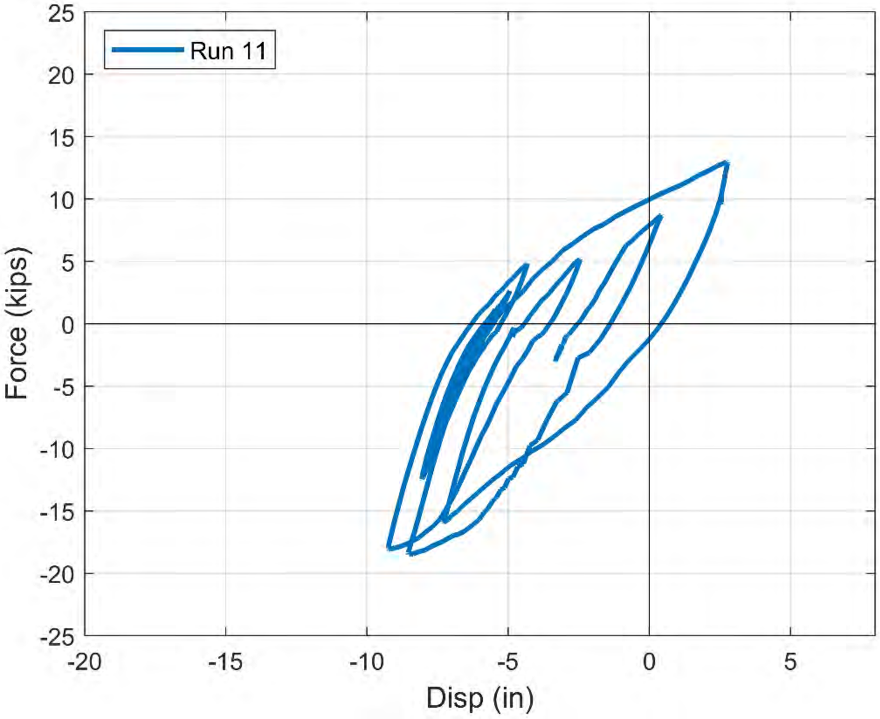

Figure 3.48 Force-displacement relationship for run #11

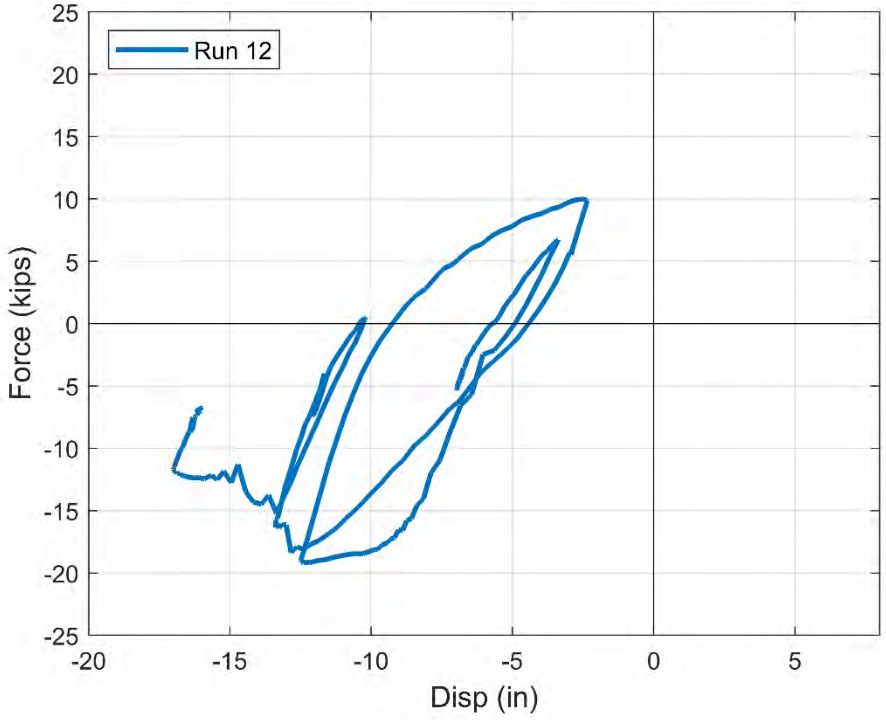

Figure 3.49 Force-displacement relationship for run #12

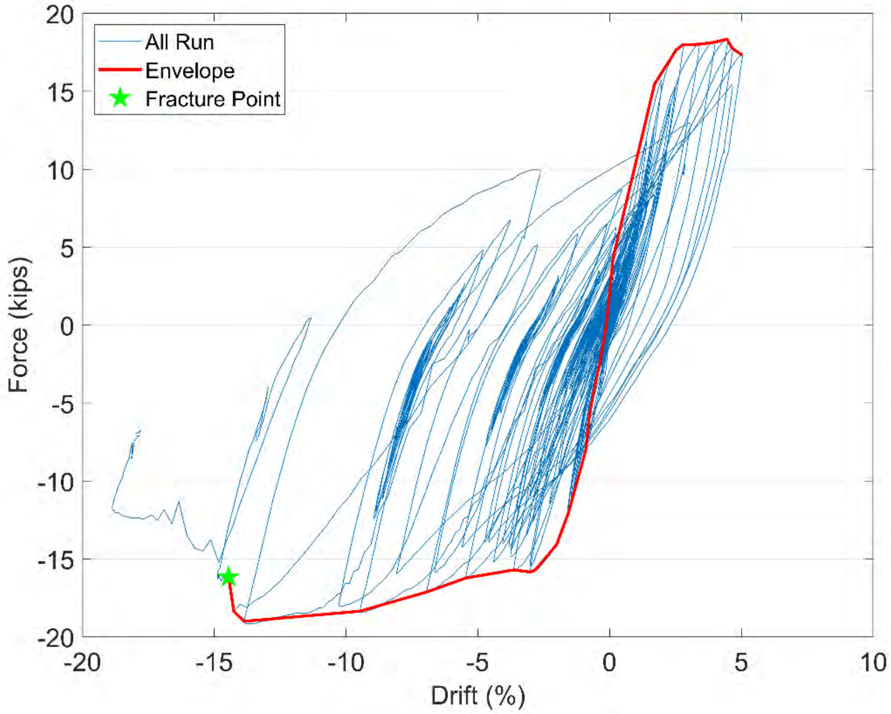

Figure 3.50 Hysteresis envelope for positive and negative sides

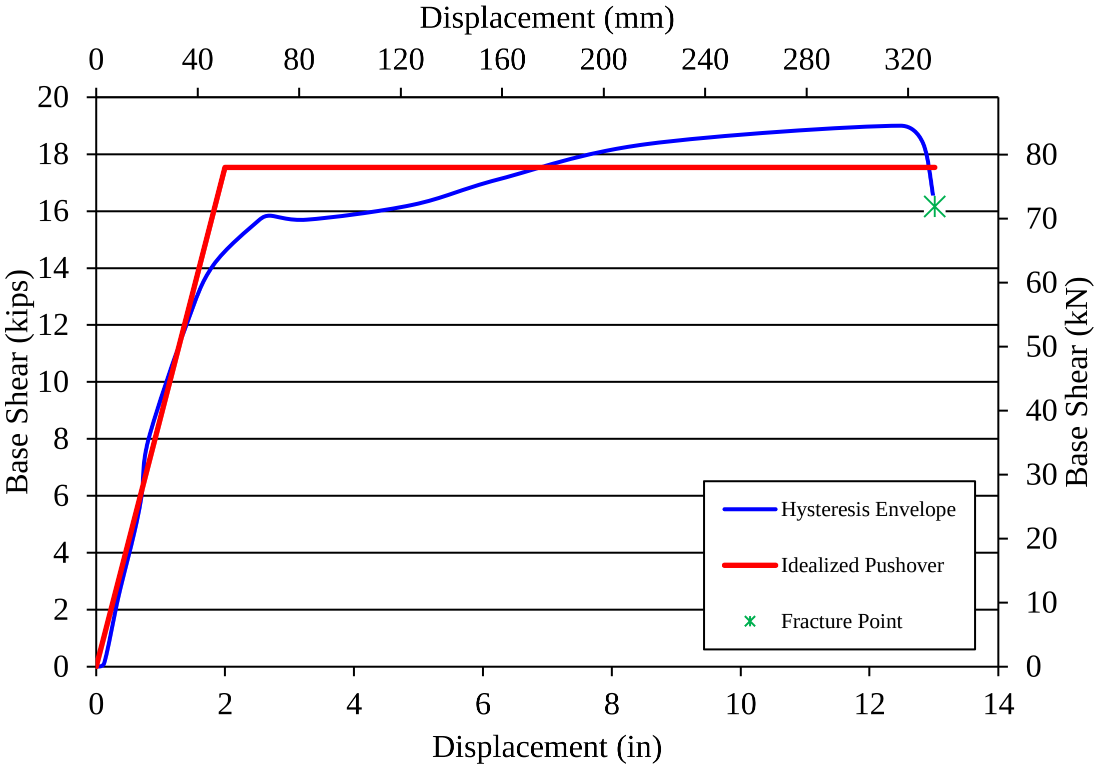

Figure 3.51 Experimental pushover curves based on actual hysteretic behavior and idealization

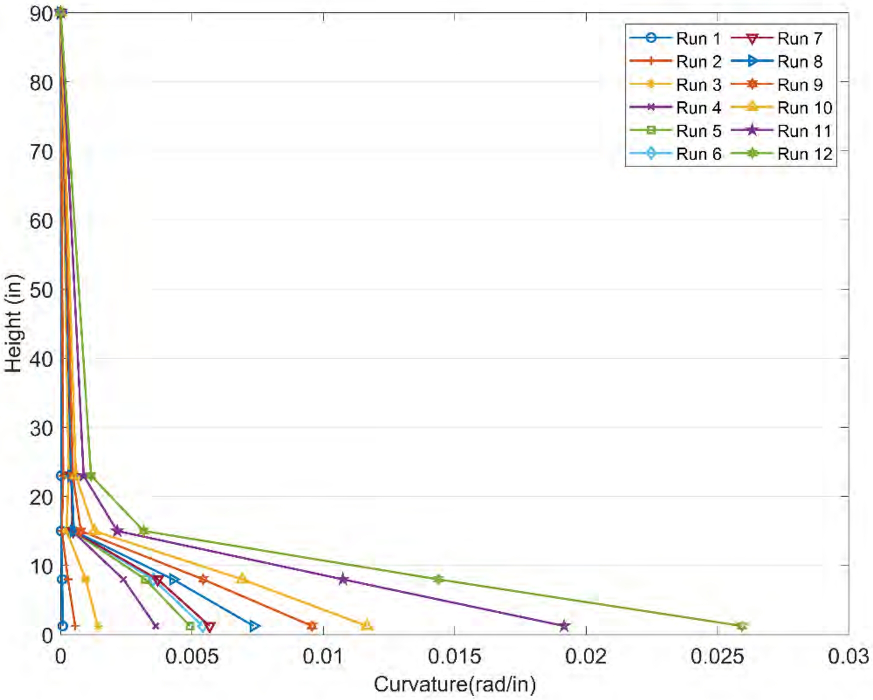

Figure 3.52 Estimated curvature profile for runs 1 through 12

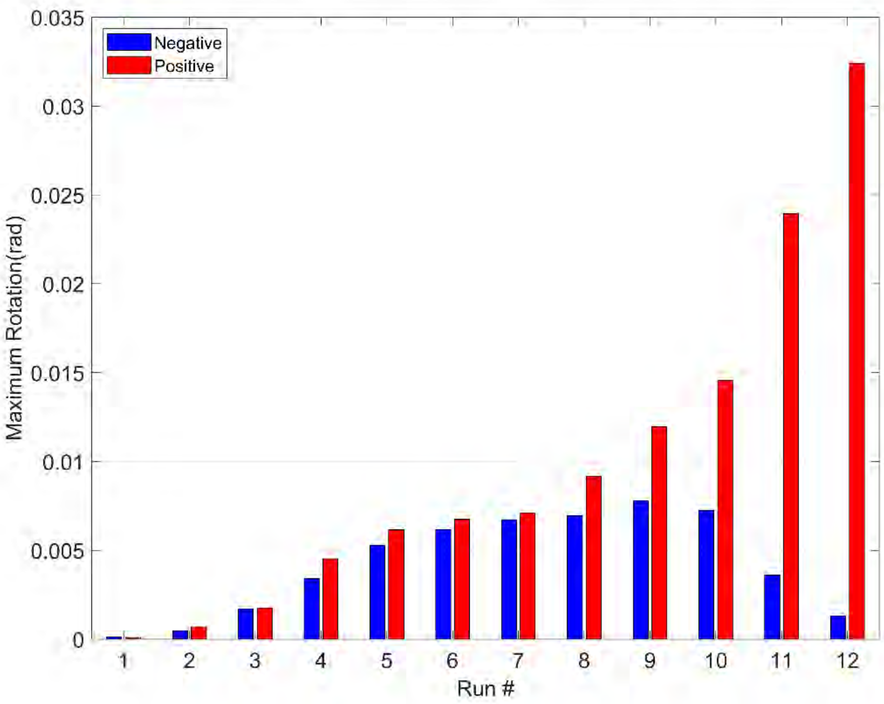

Figure 3.53 Measured maximum and minimum rotations for each run

CHAPTER 4 FIGURES

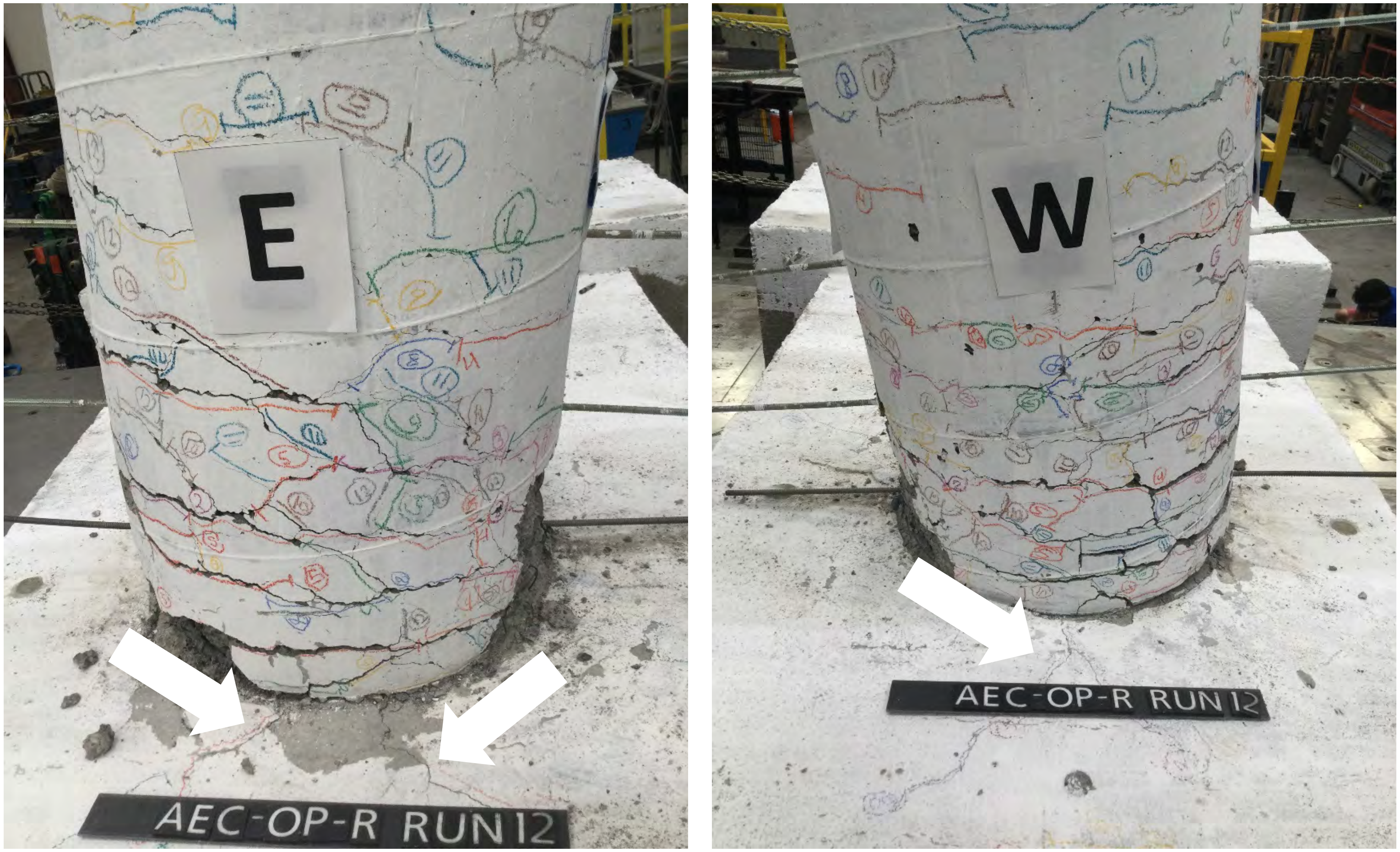

Figure 4.1 Shear cracks around the column-cap beam interface

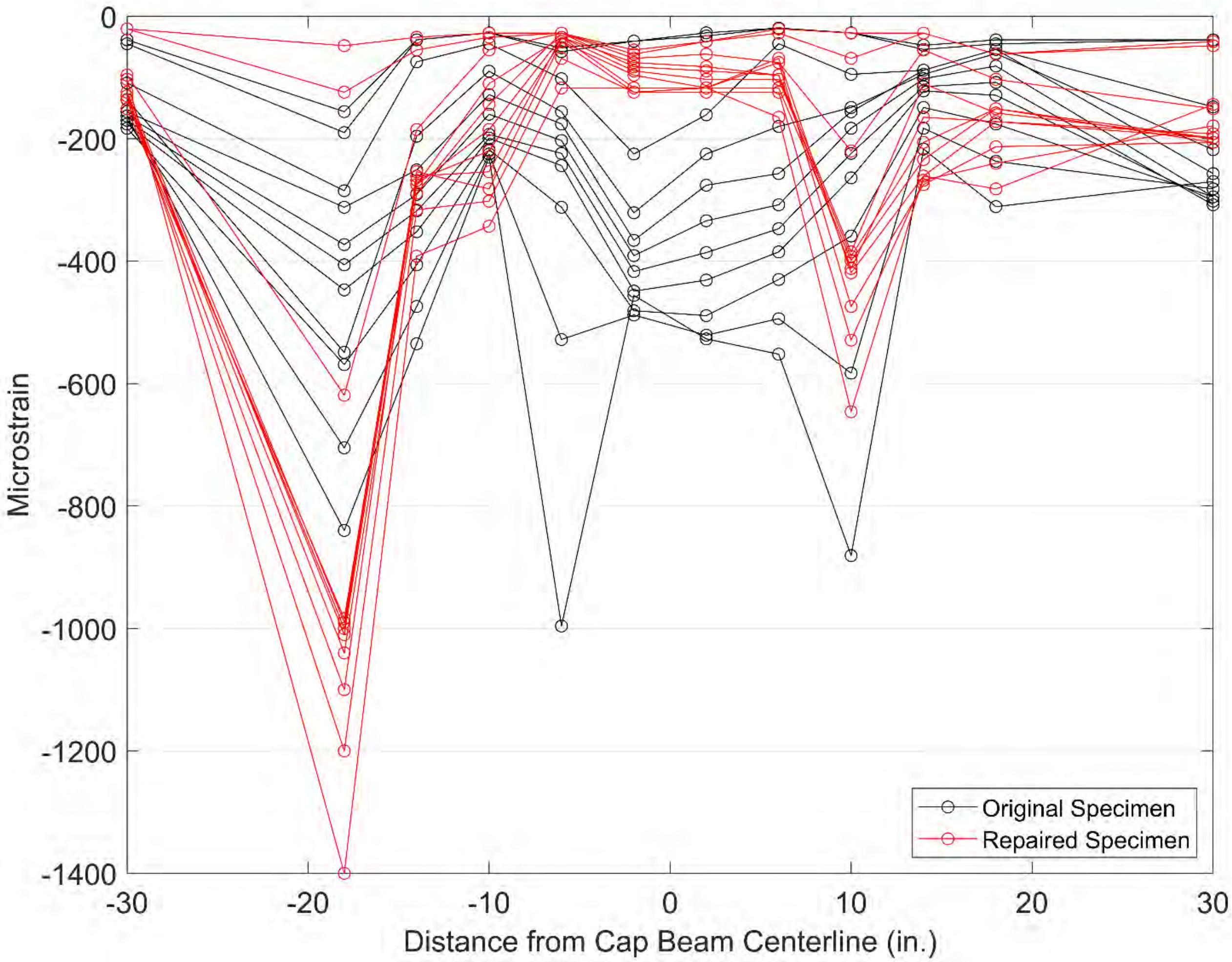

Figure 4.2 Strains in the cap beam stirrups along the cap beam length

Figure 4.3 Comparison of concrete spalling as observed from the specimens tests located at: (a) north section of the original specimen, (b) north section of the repaired specimen, (c) south section of the original specimen, and (d) south section of the repaired specimen

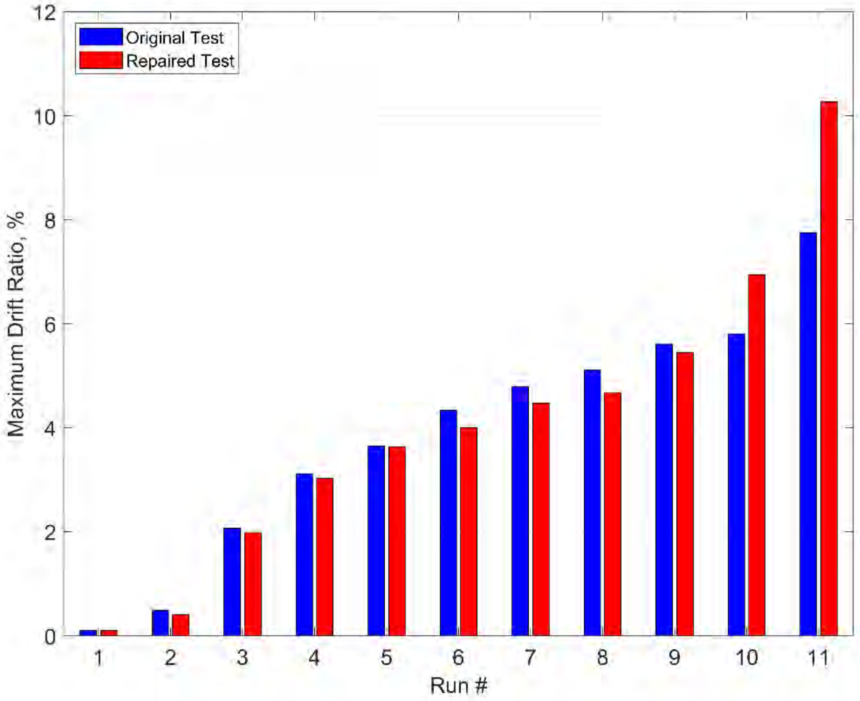

Figure 4.4 Maximum drift ratio observed from both specimens tests

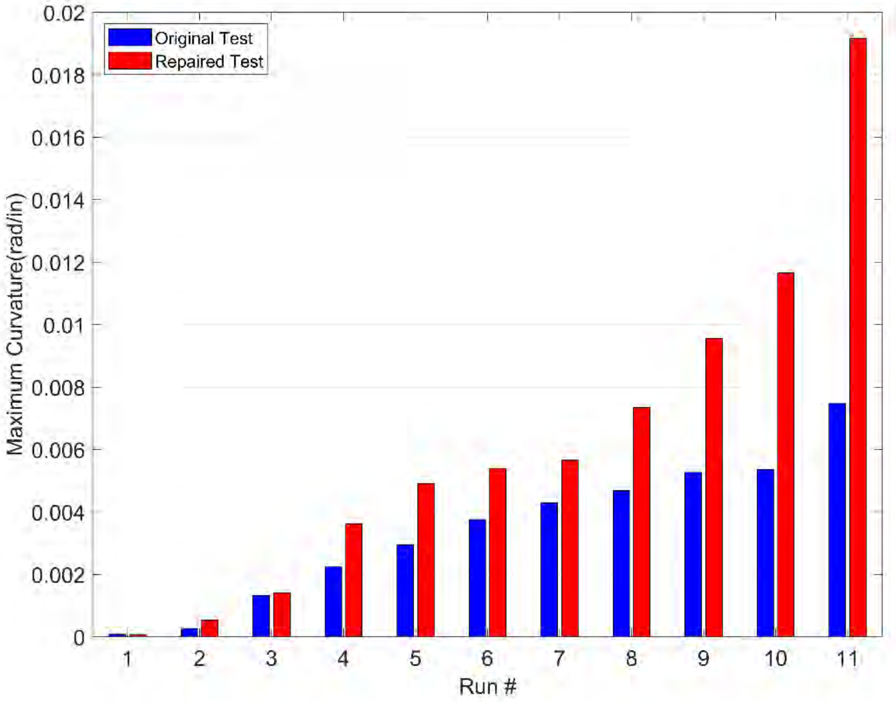

Figure 4.5 Maximum curvature estimated in the column from both specimens tests

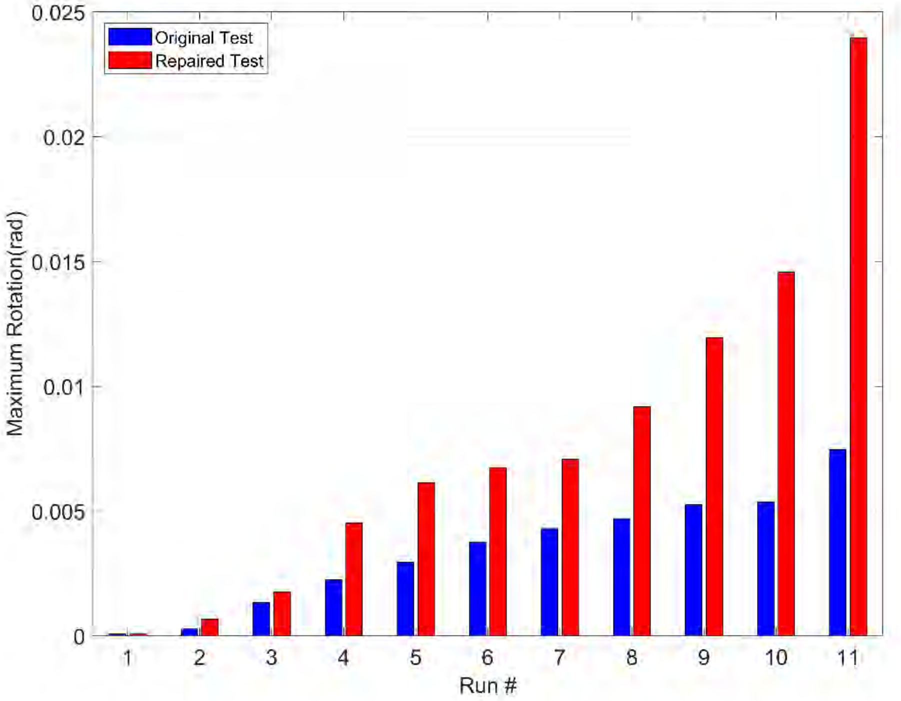

Figure 4.6 Comparison of maximum rotations for both the original and repaired specimens

Nevada Department of Transportation
Kristina L. Swallow, P.E. Director
Ken Chambers, Research Division Chief
(775) 888-7220
kchambers@dot.nv.gov
1263 South Stewart Street
Carson City, Nevada 89712